ONLINE CORRECTION OF SCANNING PROBE MICROSCOPES WITH PIXEL ACCURACY

Kai Dirscherl

LYNGBY 2000
Ph.D. Thesis
IMM-PHD-2000-76

ISSN 0909-3192

Copyright © 2000 Kai Dirscherl
Printed by DTU-Tryk, DTU
Bookbinder Hans Meyer

Preface

This thesis has been prepared at the Department of Mathematical Modeling (IMM), Technical University of Denmark, and the Danish Institute for Fundamental Metrology (DFM), Lyngby, Denmark.

The work has been financed by the European Commission under the project no. ERB4001GT965760 and carried out in accordance to contract no. ERBSMT4CT979015. It has been performed under the supervision of:

Mads Peter Sørensen

Department of Mathematical Modeling (IMM), Technical University of Denmark

Jørgen Garnæs

Danish Institute of Fundamental Metrology (DFM)

The work started August 1997 and has been carried out mainly at Danish Institute for Fundamental Metrology, Lyngby, Denmark. During April 1998, three weeks were spent at the Department for Mechanic Mathematics of the Moscow State University, Moscow, Russia. September and October 1999 were spent at the Institute of Microelectronics and Submicrontechnology of the Technical University Delft, The Netherlands.

Lyngby, August 2000

Kai Dirscherl

Acknowledgments

First of all I would like to thank the European Commission for allowing me to elaborate this thesis.

I am grateful for the inspiring discussions with my supervisors Jørgen Garnæs, Mads Peter Sørensen and Lars Nielsen. A special thanks to Lars and Jørgen who always ask the right questions. I also want to thank Jørgen for helping me with the translation of the abstract to the Danish resumé.

Furthermore I want to thank my colleagues Jan Friis Jørgensen, Anders Kühle and Niels Kofod for the talks and discussions that contributed to this work. Jan included a special routine for image analysis in his now commercial image processing program SPIP which was helpful at the start of my work.

A big hug goes to the Danish Institute of Fundamental Metrology DFM for their hospitality during the past three years.

I am also thankful to Reinder Banning and Odet Lemmens from the Technical University of Delft, Holland, for giving me the opportunity to program their state-of-the-art feedback controlled stage and letting me push it to the limit and, for the case of one experiment, "slightly" beyond. (Re-booting the system helped.)

Thank you very much, Maria and Yuri Ponomareva from Moscow, for the scientific support and huge friendship you offered during my stay at the Moscow State University, Russia.

Without the generosity of Curt Sander and Jens Hovgaard from Danish Micro Engineering A/S, a crucial part of this thesis would not have been tested experimentally. They provided me with their commercial SPM DualScope and the permission to change the source code of the control program to suit my purposes.

Ruth Rasmussen and Villy Damstrup have offered distraction with their fantastic works of art and provided a haven to rest and relax with their beautifully arranged garden - thank you.

I also want to express my gratitude to my former German math-teacher Winfried Fandel for still staying in touch with me and for continuously encouraging my research. Without his initiative and support more than 15 years ago, this thesis might not have been written.

Last but farthest from least I am deeply thankful to my fiancée Mette and my daughter Josephine who brighten up my daily life with their smiles.

Abstract

In this project "Online Control of Scanning Probe Microscopes with Pixel Accuracy", the development of an algorithm is described that enhances the measurement uncertainty of software controlled SPM by one order of magnitude from 2% to 0.2%. The SPM is globally used as a metrological instrument for dimensional and length measurements. The sample surfaces are scanned 3-dimensionally, typically within the ranges up to 150 μm x 150 μm x 6 μm. This is done by moving a sharp tip systematically across the sample while simultaneously recording the height of the tip. Typically, the tip has a radius of curvature of 10 nm and an opening angle of 30.0°. Even atomic resolution can be achieved. The scan movement of the tip is not linear however. This is caused by the propelling device of the SPM for the scan motion - a piezoelectric ceramic. The two major non-linear responses of the piezo to the applied control voltage are rate-independent hysteresis between the scanner's position and the voltage and time-dependent creep of the ceramic. Hysteresis leads to a non-linear mapping of distances while creep changes the actual sensitivity of the ceramic. The non-linearity of a hysteresis loop is in the order of 2-20% depending on the piezo material used and the scan range. The change in sensitivity is up to 20% as well, depending on the scan frequency. Current software controlled SPM are equipped with an algorithm that changes the shape of the control voltage online in a way to produce a linear piezo movement. The algorithm typically contains 5 - 7 parameters which have to be calibrated manually. Still, non-linear errors remain in the order of 1-2%. One pixel in a 512x512 image corresponds to 0.2% per direction. This goal of measurement accuracy is reached with the algorithm developed in this thesis.

Three different SPM are analyzed for their non-linearity. Two commercial tube scanners are applied with a maximum scan range in x and y of 40.0 μm and 160.0 μm as well as one specially designed stack scanner with a maximum range of 5.0 μm. For the tube scanners, a 1-dimensional line pattern with a reference period of 3.0 μm and a 2-dimensional grating with a reference pitch distance of 200.0 nm are applied as length standards. The non-linearity of the scanner is then traceable to the distances on the samples. The stack scanner is equipped with capacitive sensors that measure the position of the scanner during the scan process. The signal of the sensors can be used as closed loop feedback signal.

At first a model is set up to describe the measured hysteresis. An ordinary

linear differential equation proves to yield the desired accuracy of 0.2% when simulating the measured hysteresis. This is done with 5 model parameters and verified for 99% of the scan range of the SPM. In addition to this, the model is not restricted to a periodic scan movement in the lateral plane as most online models are. It is flexible enough to even describe the random rate-independent movement in the z-direction. After simulating the hysteresis, the model is enhanced in order to describe time-dependent creep during the scan motion. The new model contains 7 parameters and yields the desired accuracy of 0.2% for a large choice of scan ranges and scan frequencies. The parameters are determined in a numerically optimum way by using a least-squares-fitting technique.

After having successfully simulated the measured non-linearities, the model is inverted in order to form an algorithm for online correction during the scan process. Also the online algorithm is tested on two different scanners. The residual non-linearity of online corrected images is in the order of 0.2 % for both scanners: The error in length changes between ±1% from experiment to experiment. Within one experiment however, the variation of the errors is 0.3%. Therefore it is concluded that the online algorithm is stable within the set goal of 0.2% measuring uncertainty, but the piezo changes arbitrarily in the its sensitivity.

Further results of this thesis include the simulation of transient hysteresis as occurs at a change of scan conditions. This is also applied to the z-direction. Here an overshoot at a large step is qualitatively simulated and explained by hysteretic behaviour.

Resumé (in Danish)

I dette projekt "Online kontrol af skanderende probe mikroskoper (engelsk: scanning probe microscopes (SPM)" beskrives udviklingen af en algoritme som forbedrer måleussikerheden af software kontrollerede SPM med en størrelsesorden fra 2% til 0,2 %. SPMer bruges globalt som et metrologisk instrument til dimension og længde målinger. Prøvens overflade skannes 3-dimensionelt , typisk indenfor et område på 150 μm x 150 μm x 6 μm. Dette gøres ved at bevæge en skarp spids systematisk over prøven samtidig med at højde af spidsen optages. Typisk har spidsen en krumningsradius på 10 nm og en åbningsvinkel på 30°. Selv atomar opløsning kan opnås. Dog er den skanderende bevægelse af spidsen ikke lineær. Dette forårsages af den drivende anordning for SPMer til skannebevægelsen - en piezoelektrisk keramik. De to største ikke lineære responser af piezoen til den påtrykte spænding er tidsuafhængig hysterese og kryb af keramikken. Hysterese fører til en ikke lineær afbildning af afstande medens kryb ændre den aktuelle følsomhed af keramikken. Ulineariteten af en hysterese loop er i størrelsesordenen 2-20 % afhængig af piezomaterialet der er brugt og skanneområdet. Ligeledes er ændringen i følsomhed op til 20%, afhængig af skannefrekvensen. I øjeblikket er software kontrollerede SPMer udstyret med en algoritme som styrer formen af kontrolspændingen på en måde således at en lineær piezobevægelse produceres. Algoritmen indeholder typisk 5-7 parametre som skal kalibreres manuelt. På trods af dette forbliver ulineariteten af størrelsesordenen 1-2%. En pixel i et 512 x 512 billede svarer til 0,2% per retning. Dette mål for målenøjagtigheden opnås ved algoritmen udviklet i denne afhandling.

Tre forskellige SPMer er analyseret for deres ulinearitet. To kommercielle rør skannere er anvendt med et maksimalt skanneområde i x og y på 40,0 μm og 160,0 μm såvel som et specielt designet stak skanner med et maksimalt skanneområde på 5,0 μm. For rørskannerne anvendes som længdenormaler et 1-dimensionalt liniemønster med en referencelængde på 3,0 μm og et 2-dimensionelt gitter med en referencelængde på 200 nm. Ulineariteten af skanneren er således sporbar til afstandene på prøven. Stakskanneren er udstyret med kapacitive sensorer som udmåler positionen af skanneren under skanningen. Signalet fra sensorerne kan bruges som signaler til et lukket tilbagekoblingskredsløb. Først sættes en model op til at beskrive den målte hysterese. En ordinær lineær differentialligning viser sig at give den ønskede nøjagtighed på 0,2% når den målte hysterese simuleres. Dette gøres med

fem model parametre og er verificeret for 99% af skanneområdet for SP-Met. Oven i dette er modellen ikke begrænset til en periodisk skandende bevægelse i det laterale plan som de flest onlinemodeller er. Den er fleksibel nok til at beskrive tids uafhængigt den tilfældige bevægelse i z-retningen. Efter simuleringen af hysteresen, forbedres modellen for også at beskrive den tidsafhængige kryb under skannebevægelsen. Den nye model indeholder syv parametre og giver den ønskede usikkerhed på 0,2% for et stort udvalg af skanneområder og skannefrekvenser. Parametrene er bestemt på en numerisk optimal måde ved at bruge mindste kvadraters metode.

Efter succesfuldt at have simuleret den målte ulinearitet, inverteres modellen for at forme en algoritme til on-line korrektion under skanneprocessen. Også on-line algoritmen testes på to forskellige skannere. Den tilbageblevne ulinearitet af on-line korrigerede billeder er af størrelsesordenen 0,2% for begge skannere. Fejlen i længde variere indenfor ±1% fra eksperiment til eksperiment. Indenfor et eksperiment er variationen 0,3 %. Derfor konkluderes at on-line algoritmen er stabil indenfor det satte mål på 0,2% måleusikkerhed, men at piezoens følsomheden ændres tilfældigt.

Andre resultater i denne afhandling inkluderer simuleringen af transient hysterese som forekommer ved en ændring af skannebetingelser. Dette er også anvendt på z-retningen. Et overshoot ved store step kan kvalitativt simuleres og forklares ved hysteretisk opførelse.

?!? To Measure Is To Know ?!?

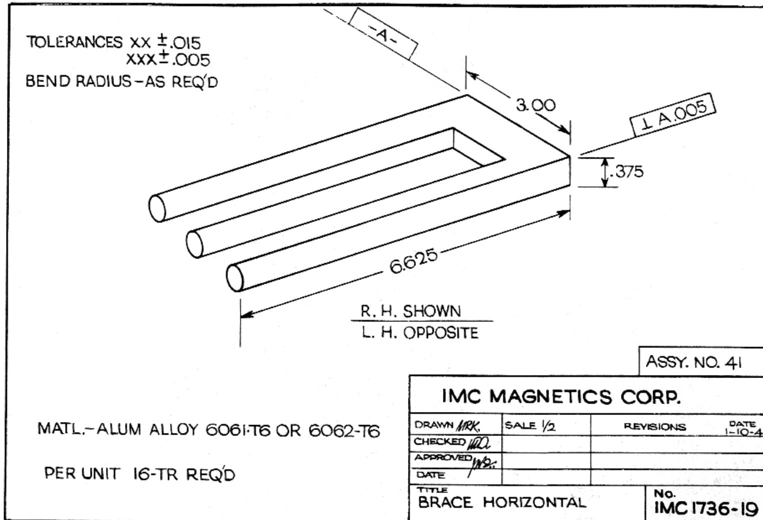

Figure 1: "The Devil's Fork". An optical illusion set into the world of technical design [1]. Artist unknown. Although this sketch is complete with length declarations and tolerances for all 3 dimensions, the manufacturing might take a while.

The visual sense is generally the most used sense of a human being. In our times of informational abundance, we constantly struggle to select valuable information from that which is to be dumped. It starts in the morning when a look at the noisy alarm clock reminds us panicky to get up and going. While being stuck in the daily traffic to work, at work, after work at times of leisure, it is always the visual impressions that mostly influence our actions. Computer screens flash rapidly of constantly changing presentations on more or less reliable web pages. The expression "WYSIWYG" - What You See Is What You Get - has reached the state of a well-known standard for word processing software - rising from the linguistic level of pure advertisement to the absolute minimum of necessary features of the software. The danger about the sheer amount of visual information we receive today lies within the selection process we must undertake. Useless and valuable impression are to be separated from each other, often within

the wink of an eyelid. We tend to rather trust the information which is supported by numbers. Numerical values are absolute, they leave no margin for interpretations. While you can argue whether one apple looks more delicious than others, its weight and thus its price is fixed. "Surely there must be truth in it when the information is supported by lots of numbers" is the common denominator of superficial criticism. Numbers rely to mathematics and engineers, "these guys are educated and know what they are doing.". The power of numbers is even exploited by the advertisement industry. Commercials underpin the quality of the products by quickly scrolling columns of numbers in the background or by colorfully plotting lines in checkered diagrams. These examples out of the common life demonstrate the simplicity to deceive and camouflage facts as well as the credulity of the observer.

On an other intellectual level, but spiked with the same superstition, is the attitude of the common user of commercially available scientific instruments, such as the Scanning Probe Microscope. The points of view can vary from the ignorant "I gave several thousands of dollars for this instrument, so it measures correctly." via the uncritical "I know there's an slight error in the dimensions, but as an approximate estimate the image suffices." to the expert "It says 30.0 μm on the screen, but I know it's only accurate within ± 0.3 μm in reality.". Although the SPM is a highly advanced and sophisticated instrument, a critical eye is to be thrown on all experimental results. Typically, according to the manufacturers, the remaining measuring error along the two lateral axis is within 1-2%. This corresponds to 5 to 10 pixels for each axis in a common image of 512x512 pixel.

In order to optimize the performance of software-controlled SPM, I take a closer look on the measurement error of piezo-driven SPM. This dissertation presents an algorithm that reduces the error during the scan process to the order of the smallest visually observable unit: 1 pixel. The SPM shall thus become more accurate just by replacing the existing software control. Additionally, the calibration procedure, often dependent on subjective manual adjustments of the user, is facilitated and optimized.All this shall relieve the user from speculating too much over what is displayed on the screen.

Kai Dirscherl, Lyngby, 1st of August 2000

Contents

1 Introduction **15**

1.1 Scanning Probe Microscopes 16

1.1.1 Working principle 18

1.1.2 SPM used 23

1.2 Piezoelectricity 24

1.3 Goals of this work versus State-of-the-Art 27

2 Hysteresis **31**

2.1 Experiments 33

2.1.1 Tube scanners 33

2.2 Models for hysteresis 37

2.2.1 Maxwell capacitors 41

2.2.2 Coleman-Hodgdon 50

2.2.3 Enhancing Coleman-Hodgdon 59

2.3 Conclusion 66

3 Creep **69**

3.1 Experiments 70

3.1.1 Tube scanners 70

3.1.2 Stack scanner 72
3.2 Creep during the scan motion 75
3.3 Modelling creep 75
3.3.1 Performance analysis 83
3.4 Conclusion 88

4 Online application 91
4.1 The function LambertW 91
4.2 The control algorithm 93
4.3 Experiments 94
4.4 Linearity analysis 97
4.4.1 Medium tube scanner 98
4.4.2 Short stack scanner 101
4.5 Conclusion 113

5 Further results 117
5.1 Changing scan conditions 117
5.2 Overshoot in z at step edges 121

6 Conclusions 125

Appendix 128

A Recorded images 129

B Offset analysis 135

C Glossary 141

Bibliography 143

Ph.D. Theses at IMM 147

Chapter 1

Introduction

In 1981 Binnig and Rohrer from IBM developed a new way of imaging surfaces at atomic resolution, the Scanning Tunneling Microscope STM [2]. Their invention was rewarded with the Nobel-price in 1986. Within the past 20 years, this imaging tool has undergone a huge developmental leap from scientific education and research laboratories to a whole new branch of industry. The SPM is applied as a metrological instrument for measurement for dimensions in the micrometer and nanometer range [3]. Today, the STM is not only commercially manufactured and available at a global scale, but has also initiated further new techniques of imaging. The STM nowadays represents only one member of the still growing family of Scanning Probe Microscopes SPM. Among the representatives of SPM is the widely spread Atomic Force Microscope AFM [4], the Magnetic Force Microscope MFM and the Electric Force Microscope EFM [5]. These techniques allow the study of the sample's topography, that is the height distribution of the surface, as well as other surface properties, such as electrostatic or magnetic features. As various as the probing principles can be, all SPM share the same engine to realize the periodic scan movement: a piezo crystal. By applying an oscillating control voltage to the piezo crystal, the scanner moves in a criss-cross motion to sample the surface. The physical driving power for this rests within the remanent polarization of the piezo crystal. It also provides the scanner with the necessary resolution in length. One pixel of a scanned image at atomic resolution represents typically a spot with a width at sub-ångström range.

Chapter 1 introduces the working principle of an SPM. A closer look is taken upon the piezo crystal, because as the propelling engine it represents a vital part of any scanning probe microscope. The drawbacks are discussed when applying a piezo crystal within an SPM. The non-linearities as introduced by the piezo can be split up into to major parts: those non-linearities that are time-dependent and those that are not. To the later group, the largest contribution is given by hysteresis. Time-dependent non-linearities are often referred to as "creep". Although these disadvantages are already compensated for by the manufacturers of SPM to a certain extend, they still represent a source of measuring uncertainty. Finally, this chapter concludes by stating the goals of this Ph.D. research project.

Chapter 2 takes a closer look onto hysteresis. Models are described and their applicability to this project is discussed.

Chapter 3 deals with time-dependent relaxation during the scan process. This creep acts superimposed on the hysteresis and influences the shape of the loop. In which way these two phenomena can be separated, and to what level of accuracy, is part of this section.

Then in the following chapter 4 the results of 2 and 3 are combined when describing the control algorithm in order to reduce the measurement error of an SPM to the level of a pixel. The online algorithm is derived and experimentally tested.

Chapter 5 mentions further results of the hysteresis model of chapter 2. Features in the scanned image that have recently pointed only towards time-dependent creep also contain time-independent aspects.

Chapter 6 summarizes the research and concludes.

This dissertation ends with an appendix, a glossary and the bibliography.

1.1 Scanning Probe Microscopes

All SPM share the same basic operating principle. The surface to be imaged is probed by a sharp tip, fig. 1.1. The tip's typical radius of curvature is approximately 10.0 nm, while the typical opening angle is about 30.0 °. The tip is moved in the same zig-zag scan motion over the surface as known from the electron-ray of a TV-set when creating an image on the screen. This scan motion of the tip produces a topographic image by recording

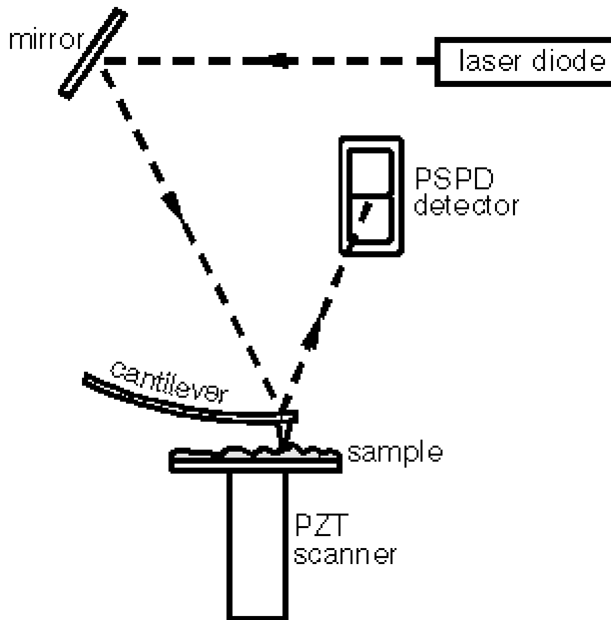

Figure 1.1: Detecting the position of the cantilever. A laser beam bounces off the back of the cantilever onto a position-sensitive photodetector (PSPD). As the cantilever bends, the position of the laser beam on the detector shifts.

the tip position and its height deflection. SPM operate typically in the micrometer to nanometer range. An upper limit of the scan range can be stated as 150.0 μm x 150.0 μm x 6.0 μm for the axes x,y and z. Typically an image consisting of 512x512 pixels is sampled. The resolution depends on the scan range chosen and can be down to 0.1 nm. Yet it is not only the distribution of height over the sample surface that can be recorded. Several different physical characteristics of the sample can be explored depending on the nature of the probing tip and its interaction with the surface. A more detailed insight in different scanning techniques is discussed in the following.

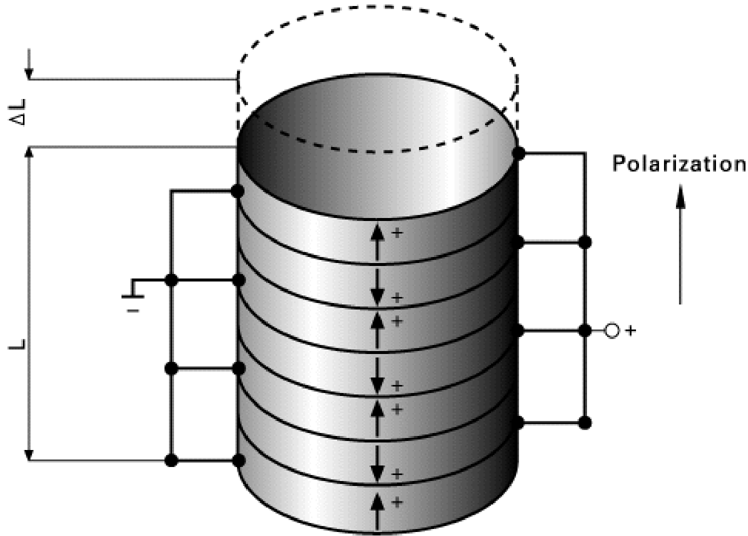

Figure 1.2: A piezo stack is composed of piezoelectric discs with alternating polarization. The electrodes set in between the discs are connected as shown. An applied voltage thus can prolong the length L of the stack by ΔL.

1.1.1 Working principle

The type of SPM used for this project are commercial AFM. A brief introduction to the working principle is presented in [6]. Figure 1.1 shows the principal setup of an AFM. The probing tip sits at the end of a cantilever. Focused on the cantilever is a laser beam. From there the laser is reflected to the centre of a two- or four-segmented photodiode. A deflection of the cantilever then results in a displaced reflection of the laser. The signal from the photodiode typically is applied as a feedback signal. It indicates the deflection of the cantilever. Thus it can be applied to control the contact between tip and sample during the process of scanning. Either the cantilever or the sample is fixed while the other is mounted on a drive of piezoelectric crystal. The piezo drive is responsible for both the scan motion in the lateral x/y-direction and the feedback response for the tip in the z-direction. Two arrangements of piezo material are most common

for the piezo drive. The first uses three piezo stacks, fig. 1.2, which are aligned perpendicular to each other. Thus each euclidean direction x,y,z is controlled by a single independent piezo stack. The other arrangement consists of a hollow cylindrical tube with four outer and one inner electrode, figure 1.3. Here each pair of opposing electrodes creates a bending movement of the tube in either x or y. By biasing all electrodes with the same voltage, the tube extends and thus moves in z. The movement in z is crucial since it is responsible for keeping the tip and the sample in contact during the scan.

There are several interaction modes between tip and sample by which the microscope can trace the sample surface. They take advantage of different forces as tip and sample approach, fig. 1.4. As the tip and the sample are gradually brought together, they first weakly attract each other due to van der Waals forces. This attraction increases until the atoms are so close together that their electron clouds begin to repel each other electrostatically. This electrostatic repulsion progressively weakens the attractive force as the interatomic separation continues to decrease. The force goes to zero when the distance between the atoms reaches a couple of ångströms, about the length of a chemical bond. When the total force becomes positive (repulsive), the atoms are in contact. This is where an SPM operates in "contact mode". The scanning tip touches the sample surface. The contact force is typically set to 10^{-7}N. This is non-destructive for most combinations of tip and sample material. The tip is kept in contact with the sample by a feedback circuit. When a deflection of the cantilever occurs, say the tip moves up a slope and the cantilever is forced upwards, the feedback controller recognizes this by a change in the laser reflection and sends a signal to the piezo drive, fig. 1.1. Now the sample is moved in the opposite direction of the tip-deflection in order to keep the contact force constant. The record of the feedback signal during the complete scan process is then used to map the sample's height distribution. Although the contact force is non-destructive on solid material, fine tissue or soft materials like a polymer would be damaged if not destroyed.

Other ways of tip-sample interaction avoid this disadvantage. The free cantilever can be excited to oscillate close to its resonance frequency, typically about 100.0-500.0 kHz. When now approaching the sample surface the amplitude of the oscillation, typically a few nanometer, is affected by the forces between the approaching tip and the sample. By using the amplitude of the oscillation as feedback signal and keeping it at a constant level, the

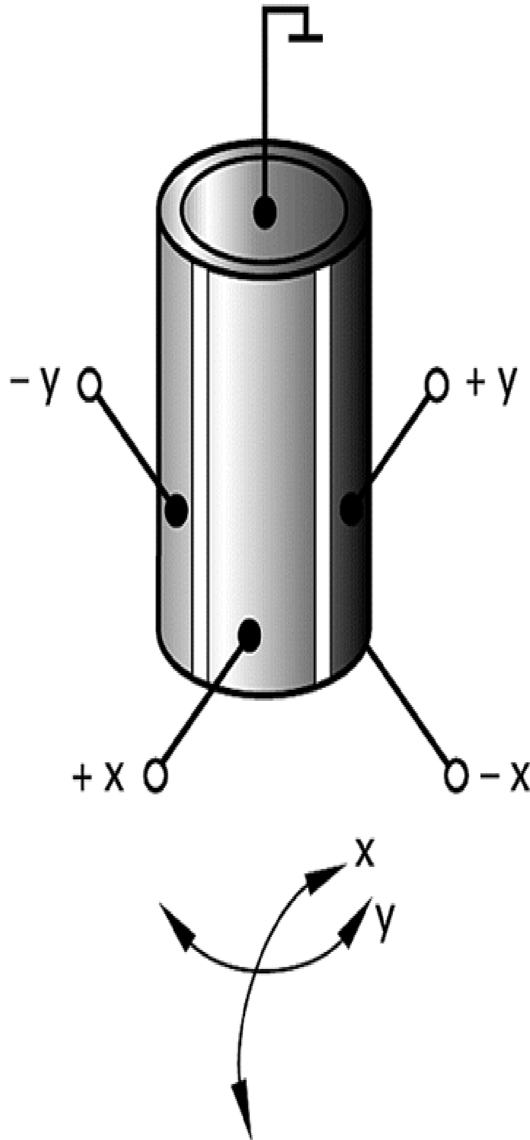

Figure 1.3: A tube made of piezoelectric material is divided into four segments. By biasing opposing electrodes with opposite voltages, a bending moment of the tube is created. The resulting "dogtail" movements can be utilized for motions in the x or y direction.

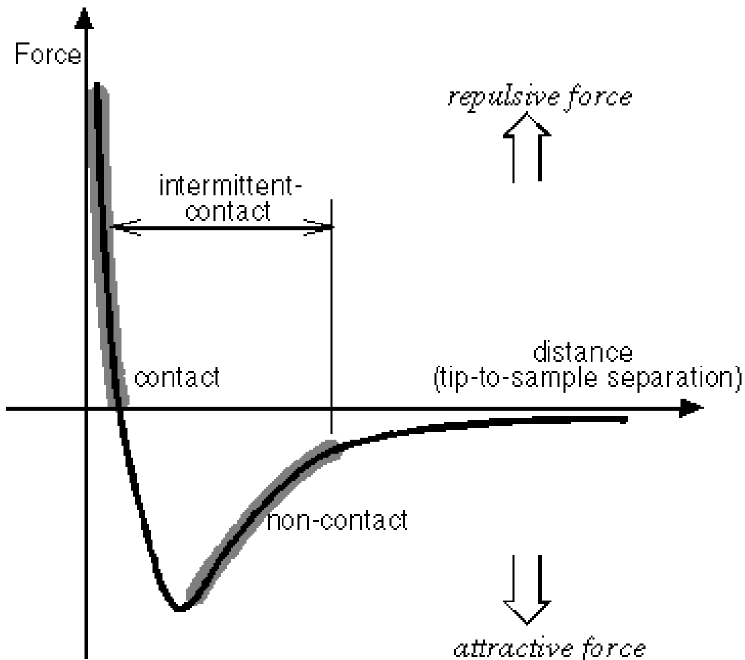

Figure 1.4: The dependence of the van der Waals force upon the distance between the tip and the sample. In the contact regime, the cantilever is held less than a few nanometers from the sample surface, and the interatomic force between the cantilever and the sample is repulsive. In the non-contact regime, the cantilever is held on the order of a few nanometers from the sample surface, and the interatomic force between the cantilever and sample is attractive.

Figure 1.5: A home-made STM. In the centre of the photo the piezo tube is visible. The soldering of control wires to two piezo segments can be seen. The tip is attached to the right of the tube, hovering next to the sample surface to be scanned.

sample can be scanned with intermittent contact or no contact at all, fig. 1.4. These vibrating scan modes also lead to a new branch of SPM. Phase detection microscopy PDM - also referred to as phase imaging - is another technique that can be used to map variations in surface properties such as elasticity, adhesion, and friction. Phase detection refers to the monitoring of the phase lag between the signal that drives the cantilever to oscillate and the cantilever oscillation output signal. Now it is not only possible to map the height distribution but also to gain data about additional physical properties simultaneously.

Other scan techniques equip the cantilever with a tip that is sensitive to different forces such as magnetic, electrostatic, capacitive or material properties like thermal conductivity. In the original STM [2], the feedback signal is provided by the tunnel current between the tip and the sample. A disadvantage of this techniques is that electric conductivity is required for both the tip and the sample. A homemade STM [7] is shown in figure 1.5. However different the tip-sample interactions may be, there is one device almost all SPM share. That is the piezo drive that propels the sample or the tip during the scan process. Alas the piezo crystal possesses properties that need further consideration when analyzing SPM images. A closer look upon piezoelectric ceramics is done later in this paper.

DualScope	Nanoscope III	"The Stage"
DME A/S	Digital Instruments	Technical University Delft
medium tube, 4 cm	long tube, 8 cm	short stack, 3 cm
soft piezo	soft piezo	hard piezo
max.range 40.0 μm	max.range160.0 μm	max.range 5.0 μm
freq. 0.1 - 2.0 Hz	freq. 0.1 - 2.0 Hz	freq. 0.1 - 5.0 Hz
max $\pm$ 230 V	max $\pm$ 220 V	max $\pm$ 175 V
software controlled	software controlled	hardware feedback
length standard	length standard	capacitive sensors
see chapter 3. & 4.	see chapter 2. & 3.	see chapter 3. & 4.

Table 1.1: Specifications of applied SPM. From top to bottom the instrument's name, manufacturer, piezo geometry, piezo material, maximum scan range, typical range of scan frequencies, maximum voltage range, online control mechanism, traceability and occurance within this thesis are listed.

1.1.2 SPM used

The measurements described in this thesis have been executed on three different scanners. Two of them are commercially available tube scanners [8], [9], one is a specially designed stack scanner [10]. Table 1.1 sums up relevant data of the instruments. From top to bottom the instrument's name, manufacturer, piezo geometry, piezo material, maximum scan range, typical range of scan frequencies, maximum voltage range, online control mechanism, traceability and occurance are listed.

In the following, the instruments are referred to by their piezo geometry. The medium tube scanner therefore stands for the DualScope. Both tube scanners are equipped with a software online correction algorithm that changes the voltage signal sent to the piezo in order to obtain a linear scan movement. The length traceability is done with length standards. These are sample surfaces with a systematic pattern such as a line period or a 2-dimensional grating. The short stack scanner is equipped with capacity sensors that directly measure the elongation of the piezo ceramic.

1.2 Piezoelectricity

The word "piezo" is derived from the Greek word for pressure. A brief introduction to piezoelectric material can be found in [11]. In 1880, Jacques and Pierre Curie discovered that pressure applied to a quartz crystal creates an electrical charge in the crystal; they called this phenomenon the piezo effect. Later they also verified that an electrical field applied to the crystal would lead to a deformation of the material. This effect is referred to as the inverse piezo effect. After the discovery it took several decades to utilize the piezoelectric phenomenon. The first commercial applications were ultrasonic submarine detectors developed during World War I and in the 1940s scientists discovered that barium titanate ceramics could be made piezoelectric in an electric field. The piezoelectric effect is often encountered in daily life. For example, in small butane cigarette or gas grill lighters, a lever applies pressure to a piezoelectric crystal creating an electric field strong enough to produce a spark to ignite the gas. Furthermore, alarm clocks often use a piezoelectric element. When AC voltage is applied, the piezoelectric material moves at the frequency of the applied voltage and the resulting sound is loud enough to wake even the strongest sleeper. As stated above, piezoelectric materials can be used to convert electrical energy into mechanical energy and vice versa. For nano-positioning, the precise motion which results when an electric field is applied to a piezoelectric material is of great value. Actuators using this effect first became available around 20 years ago and have changed the world of precision positioning. In an SPM, the inverse piezoelectric effect is used, where an applied electric field introduces mechanical strain to the crystal. As a result, the piezo deforms and can thus move an attached sample or probing tip. Since the piezo effect exhibited by natural materials such as quartz, tourmaline, Rochelle salt, etc. is very small, polycrystalline ferroelectric ceramic materials such as $BaTiO_3$ and Lead Zirconate Titanate (PZT) have been developed with improved properties. Ferroelectric ceramics become piezoelectric when poled. PZT ceramics are available in many variations and are still the most widely used materials for actuator or sensor applications today. PZT crystallites are centro-symmetric cubic (isotropic) before poling and after poling exhibit tetragonal symmetry (anisotropic structure) below the Curie temperature, fig. 1.6. Above this temperature they lose the piezoelectric properties.

Charge separation between the positive and negative ions is the reason for electric dipole behavior. Groups of dipoles with parallel orientation are called Weiss domains. The Weiss domains are randomly oriented in

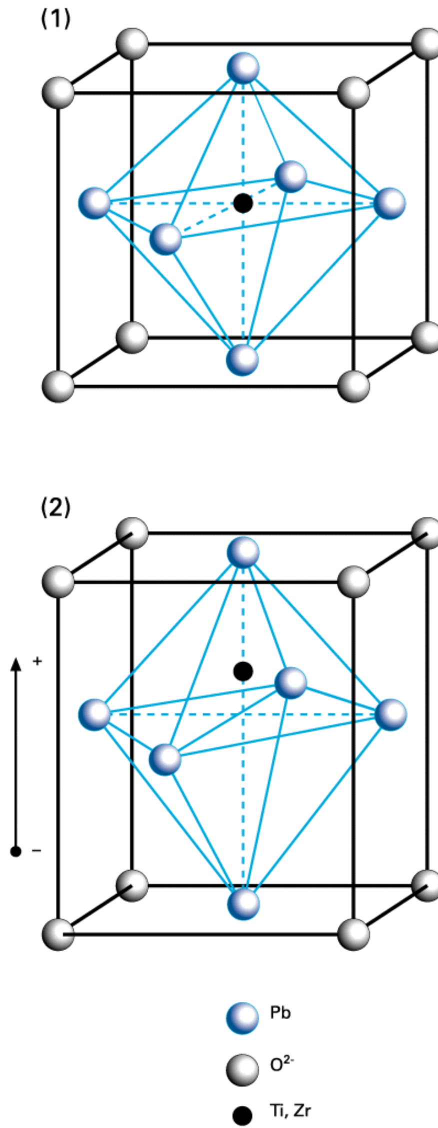

Figure 1.6: Piezoelectric elementary cell; Charge seperation when applying an strong electric field to the piezo above the Curie temperature. (1) before poling (2) after poling.

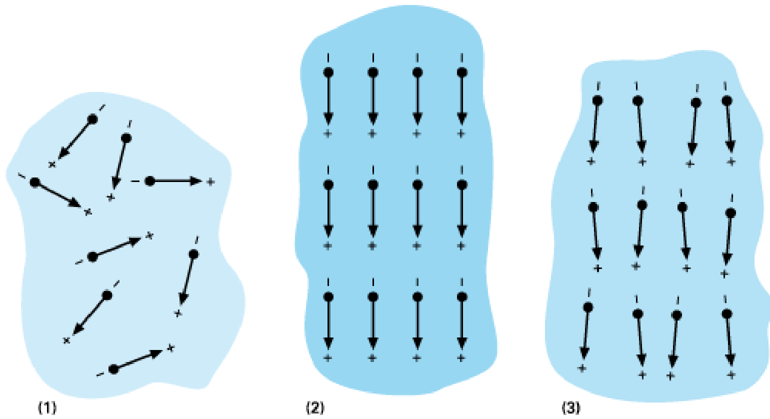

Figure 1.7: Orientation of dipols within the piezo material. (1) before, (2) during and (3) after poling the piezoelectric ceramic.

the raw PZT material, before the poling treatment has been finished. For this purpose an electric field (> 2000 V/mm) is applied to the heated piezo ceramics. The temperature where the piezo loses its polarity and can be affected by an outer electric field is called the Curie temperature. It is typically in the order of 200° C. With the field applied, the material expands along the axis of the field and contracts perpendicular to that axis. The electric dipoles align and roughly stay in alignment upon cooling, fig. 1.7. The material now has a remanent polarization which nevertheless can be degraded by exceeding the mechanical, thermal and electrical limits of the material. As a result, there is a distortion that causes growth in the dimensions aligned with the field and a contraction along the axes normal to the electric field. When an electric voltage is applied to a poled piezoelectric material, the Weiss domains increase their alignment proportional to the voltage. The result is a change of the dimensions - expansion or contraction - of the PZT material.

1.3 Goals of this work versus State-of-the-Art

Two main errors when imaging the lateral plane can be noted when using a piezo driven scanning probe microscope. First, the images obtained are not linear due to hysteresis. The ratio of two measured distances in the image does not correspond to the true ratio on the sample surface. Uncorrected, this can lead to measurement errors of 2% up to 20%, figure 1.8 and [12]. In addition, hysteresis can be the cause for further nonlinear behaviour, for instance when scan conditions such as the scan offset are changed. Secondly, the actual length scale of an image is not equal to what is really measured. This is due to insufficiently calibrated correction parameters that control the amplitude of the control voltage. All in all, the non-linear behaviour of the piezo aggravates the accurate measurement of the sample's dimensions. On top of the rate-independent effects, piezo materials also creep in time and thus give rise to a time-dependent relaxation. These non-linearities superimpose and by doing so it is even more difficult to compensate for them. Manufacturers of SPM are well aware of the drawbacks when using a piezo ceramic as the propelling element of the scanner. All SPM contain a software controlled correction algorithm which changes the voltage signal that is sent to the piezo. The algorithms for hysteresis can be of various style. Polynomial approximations [13][14], exponential models [9] or trigonometric parametrization [15] are mostly used. In the order of 3 to 6 parameters are used for these hysteresis model. Typically they can only be used for the periodic scan movement in the lateral plane. An application for the z-direction is not possible. The typical relative measurement uncertainty after online correction is depending on the scan range. Residual non-linearities within 1-2% are typically claimed of SPM manufacturers for these software algorithms. The trigonometric parameterization yields errors between 1.5% and 6% [15]. Typically, this corresponds to an average misplacement within 5 to 30 pixel per line in a 512x512 image. The measurement error increases with increasing scan range. So the software model becomes less accurate for large hysteresis loops.

There are SPM commercially available that equip the piezo with hardware distance sensors, such as capacitors, which can reduce the error of linearity to a sub-pixel level of 0.06% [16]. These instruments are very expensive and thus only affordable for users with high-end needs and the necessary economic resources. However, atomic resolutions are also hampered because

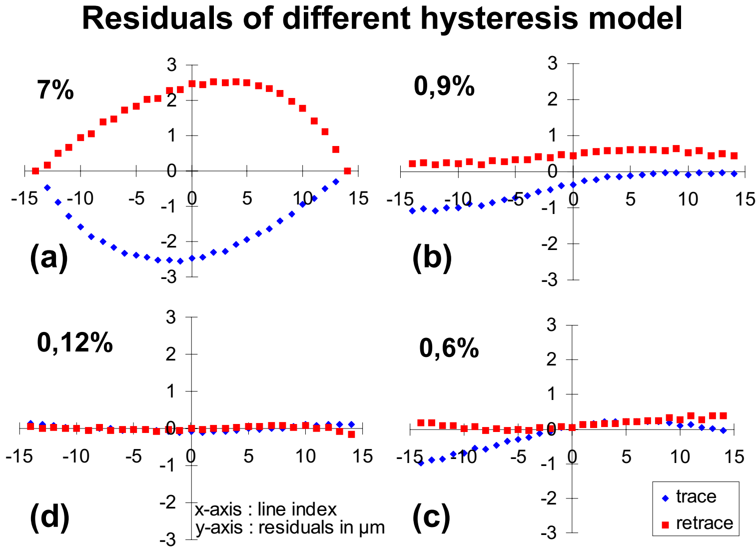

Figure 1.8: Comparison between different correction algorithms for hysteresis. A line pattern with a 3.0 μm period has been scanned without online correction. The scan range was approx 44.0 μm. In the obtained image, the steps have been indexed, number 0 being in the center of the image. The residuals in micrometer between an ideal linear scan and the hysteresis distorted image is shown in (a). The standard deviation of these residuals devided by the scan range yield a measure for the amount of distortion by the hysteresis, 7%. Then the performance of the manufacturer's algorithm for online correction of the scanner is shown (b),(c). The calibration parameters of the algorithm are set to the factory defaults for (b), newly calibrated parameters are used in (c). The residuals in (b) and (c) between the manufacturer's online correction and the ideal scan show a significant decrease in distortion compared with (a). The factory default algorithm (b), 0.9%, performs slightly worse than the newly calibrated algorithm (c), 0.6%. Plot (d) shows the residuals between the measured uncorrected hysteresis and the model for hysteresis derived later in this thesis. The model coincides with the experiment within an error of 0.12%. Clearly the model presented in this thesis is superior to the manufactorer's online correction model.

of the noise of the feedback sensors. Software controlled SPM are widely used today. Yet the attitude of most users towards the instrument can be rather naive and uncritical. The still high costs of a software controlled SPM shams reliability and accuracy. Calibration procedures are rarely performed. Although the instruments come equipped with a factory default for the online correction, they need to be calibrated frequently in order to maintain the same level of accuracy. The actual calibration method often involves subjective actions such as changing a parameter until a displayed image looks linear or marking two points with a known distance in a scanned image. These methods rely on arbitrary influences such as the display quality of the image and above all on the eyesight of the user.

The actual goal of this project is to develop a new software algorithm to correct for the nonlinear image distortions of a SPM online. The residual error of such an online corrected image is to be within the accuracy of one pixel, since this represents the smallest observable unit of the final image. Typically, images consist of 512x512 pixel, so that one pixel corresponds to $\frac{1}{512} \simeq 0.2\%$ per axis. Additionally, the algorithm is to be simple enough for online application with respect to the computational effort and the amount of parameters needed. Yet it shall be flexible enough to describe the complete range of motion with one set of parameters only. This set of parameters is to model and to correct the non-linearities of the complete range of motion. Furthermore, it is aimed for a hysteresis model that is not restricted to a periodic movement in the lateral plane. Also the arbitrary movement of the piezo in the z-direction is to be simulated.

The approach presented here to calibrate an SPM shall also absolve the user from any intervention. At first, appropriate mathematical methods are applied, such as least-squares-technique, to reach the numerical optimum when modeling the non-linearities. By using this objective way of calibrating an SPM, a reliable foundation is created for the recording and comparing of further measurements.

Chapter 2

Hysteresis

Hysteresis is derived from the Greek expression "to arrive late". It represents the major source for image distortion of an SPM. In a ferroelectric material, the hysteresis is well-known between the externally applied electric field E and the internal polarization P. In a piezo, a change of polarization P is a direct result of the ionic movements within the ceramic. Mechanically, P is therefore to a first approximation proportional to the piezoelectric strain S or the elongation, say x, for an unloaded piezo. On the other hand, a change in P yields a proportional change in the electric displacement D [17] and thus in the charge density. So via P, the strain S becomes proportional in the charge Q. Hence the observation that a charge driven piezo scanner is almost linear in its response x [17][18][19]. Additionally, hysteresis can be noticed between E and the crystal's deformation x in response to E. Thus the following chain can describe the type of relations between the relevant physical properties. Here "$\sim$" denotes proportionality while "$\diamondsuit$" indicates a hysteretic relationship.

$$V \sim E \diamondsuit P \sim S \sim D \sim Q \sim x \tag{2.1}$$

Appropriate equations can be found in [20] [21] and in the appendix of [22]. In the experiments presented in this thesis, hysteresis becomes observable in the nonlinear movement of the piezo in the x direction when applying a linear control voltage V to scan a reference standard [23]. The true dimensions of the sample surface, fig. 2.1, become distorted when scanning in the trace direction from left to right, fig. 2.2, and in the opposite retrace

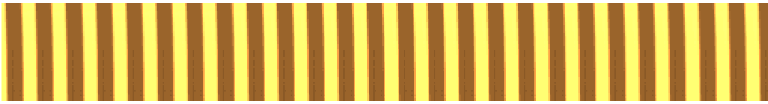

Figure 2.1: Hysteresis-free image of a sample with a line period of 3.0 μm.

direction, fig. 2.3. Hysteresis is per definition time-independent [24]. That is, no matter how fast or slow the external field oscillates, the polarization P always lacks behind E. Any time-dependent relaxation, often referred to as creep, is to be treated separately. Frequency-dependent dynamics can be excluded for the experiments, because the typical frequency range is well below 5 Hz. This is below 0.5% of the systems typical resonance frequency which is in the order of 1kHz for a tube scanner [25]. Thus the scan motion is treated as quasi-static. Usually, hysteresis and creep are superimposed on each other and difficult to separate. Chapter 3 presents a way to engage this drawback.

Manufacturers of SPM try to compensate for the hysteresis and creep. This can be done by changing the shape of the control voltage. Instead of using a triangular waveform which results in a nonlinear scanner movement, the voltage is modified in a nonlinear way in order to produce a linear movement. This represents an easy and cheap method, because the controller only needs to be programmed in this way. However, the linearity of the final movement is depending on the quality of the algorithm involved. Often polynomial or exponential models are used. The amount of parameters is in the order of 3-5. Typically, the nonlinear residual error after online correction remains in the order of 1-2% remain. More advanced solutions include a hardware feedback loop for the piezo positioning [10]. Mostly these are capacitive or interferometric sensors which keep track of the piezo's movement and restrict it to a linear fashion. However, the hardware solutions are either expensive or commercially not available because they are developed and stationed in research institutes. Atomic resolution is also hampered, because of the noise of the feedback sensors. Therefore, a more advanced algorithmic solution is desirable. For most users of SPM, a software solution is acceptable when the remaining measurement error is within pixel resolution. After all, one pixel represents the smallest observable unit in the final image. Typically an image contains 512x512 pixels, so that 1 of 512 pixels corresponds to 0.2% for each direction x and y. In this chapter, several approaches in order to model hysteresis are described.

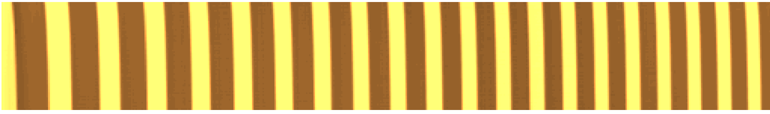

Figure 2.2: Hysteretic image distortion in trace direction from left to right, $\dot{V} > 0$. Scanned is a line pattern with a period of 3.0 μm.

Figure 2.3: Hysteretic image distortion in retrace direction from right to left, $\dot{V} < 0$. Scanned is a line pattern with a period of 3.0 μm.

Two candidates are discussed in depth.

2.1 Experiments

Various experiments with 3 different microscopes were performed during this project in order to unfold the properties of the hysteresis. In this section, experiments on the two tube scanners are described and analysed for hysteresis. In order to avoid image distortions due to frictional tip-sample interaction the long tube scanner is set to use the intermittent contact mode, the medium tube scanner to non-contact mode.

2.1.1 Tube scanners

The only way to measure distances within a scanned image is to use length standards with structures of known dimensions. Since the declared aim is to obtain one algorithm for all possible scan ranges, hysteresis needs to be measured and analyzed before the online correction can be derived. The maximum scan range for the long tube scanner is roughly 160 μm, for the medium tube scanner 40 μm. Two different samples are considered [23][26]. Sample [23] consists of a line pattern with a period of 3.0 μm with a step height of 106.0 nm. In the following this sample [23] is referred to as 1D3000. It is applied for scan ranges between 10 μm and the respective

	sample	
specifications	1D3000	2D200
type	1-dimensional periodic lines	2-dimensional periodic grid
length traceability	3.0 μm period	200.0 nm pitch
feature	106.0 nm step height	70.0 nm indentations
range of application	12 μm - 160 μm	1 μm - 17 μm
see figures	2.1-2.3,2.21,3.1,5.1,5.3,A.1,A.2	A.3,A.4

Table 2.1: Specifications of applied samples. References to scanned images are also given.

maximum. The sample [26] is a two-dimensional grid of pyramidal indentations at a pitch of 200.0 nm. The indentations are 70.0 nm deep. In the following sample [26] is referred to as 2D200. It is used for scan ranges of 17.0 μm down to 1.0 μm. See also table 2.1 for an overview.

With the long tube scanner both samples are scanned. The manufacturer's on-line correction of the SPM is disabled by setting the relevant parameters to zero. Now an uncorrected triangular control voltage is applied to the scanner. Since the image is sampled equidistantly in time, a one-to-one relation between pixel index, time and actual value of the control voltage exists for each scan line.

The first sets of experiments are sampled with the long tube scanner, table 2.2. For sample 2D200, the voltage range is varied from 5 V to 50 V peak-to-peak in steps of 2.5 V, between 50 V and 70 V in steps of 5 V. The ranges from 5 V to 70 V correspond approximately to 1.0 μm to 17.0 μm. This results in a total of 22 scanned voltage ranges. For sample 1D3000, the ranges are between 50 V up to 260 V peak-to-peak in steps of 10 V. Higher voltage ranges are chosen at the following irregular intervals to reduce the amount of data for large ranges. The additional ranges are 275 V, 300 V, 350 V, 400 V and the maximum of 440 V peak-to-peak. The ranges from 50 V to 440 V correspond to approximately 12.0 μm to 160.0 μm. A total of 26 ranges are measured for 1D3000. The amount of data points (V, x) is $n_{data,200} = 1622$ for sample 2D200 and the voltage range 5 to 70 volt peak-to-peak. For sample 1D3000, a total of $n_{data,3000} = 2114$ data points

	instruments	
experiments	long tube scanner	medium tube scanner
hysteresis 1D3000	*voltage range* 50 V - 440 V (max) *approx. scan range* 12 μm - 160 μm *scan frequency* 0.1 Hz *see figures* 2.4,2.10,2.12,2.14-2.19,2.22	*voltage range* 140 V - 460 V (max) *approx. scan range* 12 μm - 40 μm *scan frequency* 0.5 Hz *see figures* 2.5,2.20
hysteresis 2D200	*voltage range* 5 V - 70 V *approx. scan range* 1 μm - 17 μm *scan frequency* 0.1 Hz *see figure* 2.17	not performed

Table 2.2: Experiments to measure hysteresis for the two tube scanner and the two samples. References to figures resulting from the experiments or the following analysis are also given.

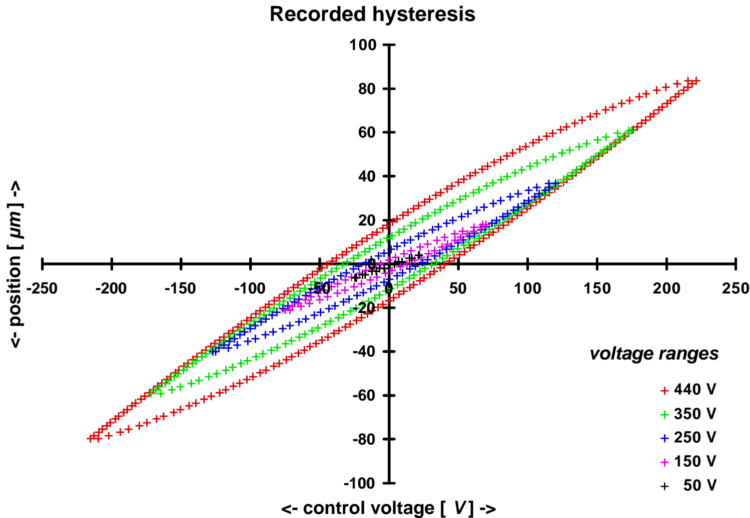

Figure 2.4: Long tube scanner, 1D3000, table 2.2. Measured hysteresis loops for various voltage ranges. Plotted is the position of the scanner x versus the level of control voltage V. The loops obtained with the medium tube scanner and the short stack scanner look the same, only on different scales.

are recorded in the voltage range 50 volt to 440 volt peak-to-peak. This corresponds to scanned distances from 1.0 μm to 17.0 μm and from 12.0 μm to 160.0 μm respectively. So 99% of the total piezo range of motion is covered. Between the scanning of the two samples, seven months have passed. At first, sample 1D3000 has been scanned to provide data for a first analysis, while 2D200 is later used to refine and verify the results. For both sets of experiments, the scan frequency is set to 0.1 Hz to provide a quasi-static movement. This frequency is four orders of magnitude below the resonance frequency of the piezo which is in the order of 1 kHz [25] in the lateral direction. Thus inertial influences can be excluded. The images are placed in the appendix. Figures A.1 and A.2 show the trace and retrace image of sample 1D3000, while 2D200 can be seen in A.3 and A.4. The images are analyzed by "the naked eye". Zooming into them, one line with pixel width is selected. The distance moved by the scanner is transferred

to the known dimensions on the samples. The beginning and the end of the periods are fixed where a step on the surface occurs on 1D3000 or where the lowest point in the indentation is reached for 2D200. Each feature of the samples is thus identified with its corresponding position measured in units of micrometer as well as with its pixel index and the level of control voltage. Figure 2.4 shows a selection of hysteresis loops as obtained with the long tube scanner and sample 1D3000. These loops are also representative for the medium tube scanner and the short stack scanner. There the hysteresis is the same, only on different scales.

The medium tube scanner provides the possibility to scan oblong images. Thus the pixel resolution in the x-direction can be increased from 512 to 2048, while simultaneously reducing the resolution in the y-direction to 16. This drastically reduces the total amount of scan lines and therefore the scan time per image by a factor of 32. With the medium tube scanner only sample 1D3000 is scanned, table 2.2. The scan ranges vary from 12 μm to 40 μm corresponding to 140V to 460V. The scan frequency is set to 0.5 Hz. Again the online correction of the manufacturer is disabled. This time two algorithms are applied to find the steps and thus the period of the sample. The first algorithm is based on the gradient of the image. The points with the highest gradients lie typically on the edges of the steps. These points are extracted to define the period. One disadvantage of the gradient is that high particles on the surface also cause additional large gradients, figure 2.5. Therefore the detected edges had to be verified manually in order to eliminate false peaks. The second algorithm fitted a third order polynomial to the profile. The period is found from the points of interception of the fit and the profile. The polynomial is not sensitive to occasional peaks, yet it can bend out of the center at both ends of the profile, figure 2.5. Still the second method does not require a manual verification of the detected edges.

In the following, the discussion and analysis of hysteresis is based on the experiments with the long tube scanner.only. The medium tube scanner is applied to verify the applicability of the final model for hysteresis.

2.2 Models for hysteresis

In order to describe the physical entity of a piezo, the interactions between external influences and internal states must be considered[21][22], figure 2.6.

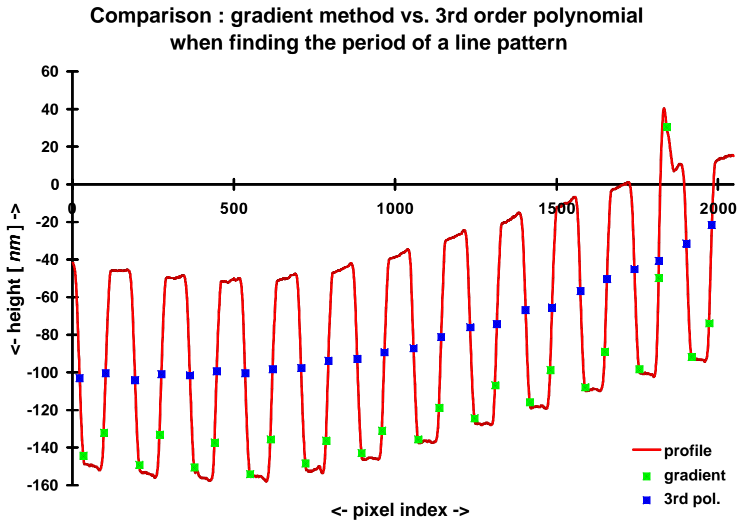

Figure 2.5: Medium tube scanner, 1D3000, table 2.2. The determination of the period of the line pattern can be automized. The gradient method, which retrieves the points with the largest slope, is more sensitive to disturbances such as dust than a fit to a third order polynimal. The particle visual on the second top from the right causes the gradient method to find a false edge. The polynomial fit evens out noisy peaks.

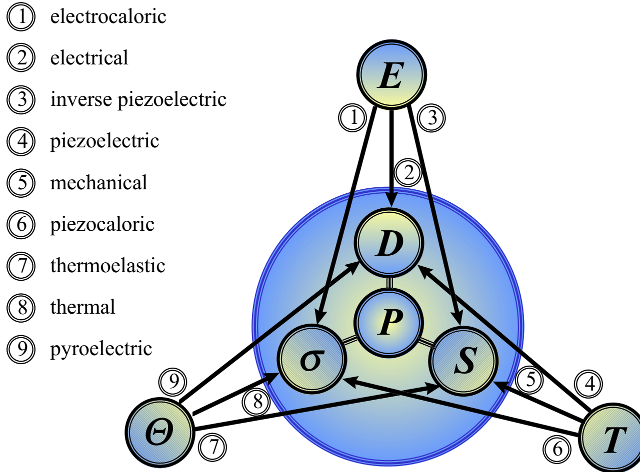

Figure 2.6: Scheme of the interaction processes between the electrical, mechanical and thermal subsystem of a piezo ceramic. The symbols used are E for electric field, D for electric displacement, T for stress, S for strain, Θ for temperature, σ for entropy and P for polarization.

The crystal's polarization P represents the governing quantity within the crystal which links the states of electrical displacement D, entropy σ and strain S. Each of these internal quantities are influenced by the external domains stress T, electric field E and temperature Θ. The nature of all interactions is also shown in figure 2.6. The thermodynamical potential Φ is then given by:

$$\Phi = U - \Theta\sigma - TS - ED \tag{2.2}$$

where the internal energy U is a function of σ, S and D with

$$dU = \Theta d\sigma + TdS + EdD \quad . \tag{2.3}$$

In order to derive the equations of motion for this thermodynamical system of a piezoelectric material, the thermodynamical minimum is to be determined where $d\Phi$ vanishes, $d\Phi = 0$. The obvious advantage of this approach

clearly lies within its detail and comprehensiveness. The model enfolds the piezoelectric material as a whole. It describes any possible interaction of the piezo with its environment during its application in the SPM. The generality of the approach allows a tether for further refinements and specific data. For instance the geometric set-up of the piezo can be included in form of boundary conditions within the mechano-elastic part of the theory [28], [29], [30]. Also finite element analysis of a piezo tube exists [31]. Yet it is exactly the complexity of this approach which makes it impossible to achieve the goals of this project. Far too many quantities and materials constants interact in a non-linear way. The functions to describe the interactions include both integral and differential equations, see [21] or the appendix of [22]. Already at the beginning of the modelling several assumptions about linearity, proportionality and first order approximations need to be done [21] in order to simplify the subject sufficiently. Therefore a lot of effort was put into modelling the hysteresis between the electric field and the polarization of a piezoelectric crystal isolated from the other physical quantities. Some approaches evolve from a physical model of the piezo crystal and its properties [18] [32] [33]. In [32], a one-dimensional lattice model of a ferroelectric is used to simulate the domain structure formed by the dipoles. As a consequence the model predicts a hysteretic dependency between the applied electric field and the response of the ferroelectric. Another physical model for the hysteresis [18] consists of comparing the process of electrically charging the piezo with the mechanical analogon of a stick-slip motion, thus yielding a hysteresis.

Apart from these physical approaches, the hysteresis has been tackled from a purely constitutional mathematical angle, too. Systems of equations that yield a hysteretic loop are utilized to describe the movement of the piezo scanner [34][35],[15][36]. These models vary in their usage of different mathematical tools. Differential equations[34][35] and [37] - [39], integral equations[36], polynomial approximation [14] [40] and parametrization [15] are applied to model hysteresis. These approaches have partly been applied already to the scanner movement of a piezo driven SPM [14][15][36]. Where stated, their residual error is in the order of 1.5-6% [15] [36]. Manufactures of SPM [8][9] also apply algorithms in order to correct for hysteresis and achieve an accuracy typically better than 2%.

The choice of the model that qualify for an online algorithm is based on the previously documented quality of measurements as well as its applicability as an online routine. The amount of parameters required is also decisive.

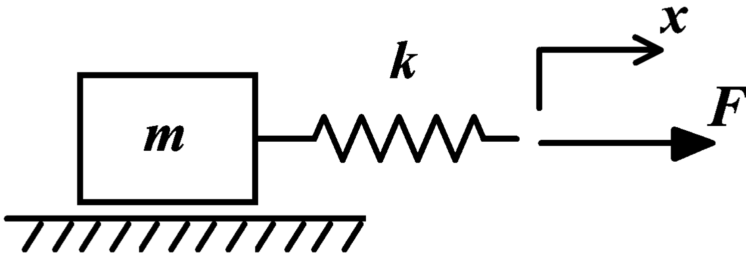

Figure 2.7: Mechanical setup to create a stick-slip hysteresis. The mass m rest with a certain friction on the surface. When the attached spring with constant k is pulled and elongated by x, the mass will first begin to move after the force of the stretched spring kx is larger than the friction force.

Some models, [32], [36], contain 100 or 250 parameters. The physical model [32] even involves the integration of several hundred differential equations, there done by the Runge Kutta method. However, an algorithm for a real-time online control program must not contain parts that require a lot of computational resources. Therefore some models do not seem appropriate for the online purposes of this project. Other approaches, [33] and [41], only give a comprehending approach to the physics without reaching a quantitative conclusion. The two most promising models are the physical model [18] and the constitutional model [34]. In [18], the hysteresis is approximated by piecewise linear functions, while [34] offers possibility to model hysteresis loops for all scan ranges with 3 parameters only. These two models are described and applied to the experiments in the following.

2.2.1 Maxwell capacitors

This approach to model the hysteresis arises from the mechanical analogon of a stick-slip motion. It is then transferred to an equivalent effect in the electric environment. Mathematically the model represents a piecewise linear approximation of the hysteresis loop.

Imagine a mass m to which a spring is connected with spring constant k. The mass m which can move a distance x rests on a lateral surface with friction. The spring is attached horizontally to it, figure 2.7. When pulling the spring slowly with a steadily increasing force F_{pull}, the spring

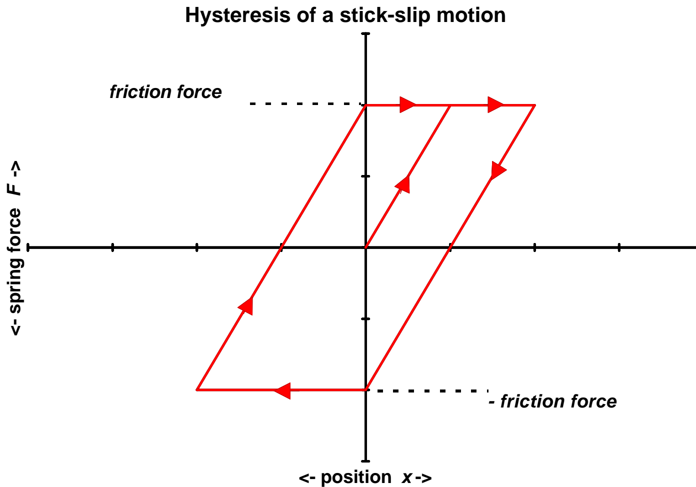

Figure 2.8: Simple hysteresis loop as created by the stick-slip motion of mass with a spring attached. Starting in the origin, the spring is stretched by x and hence the force applied to the mass increases linear in x. When the spring force equals the friction force, the mass begins to move. Now the applied force of the spring remains constant while the position of the springs endpoint x continues to increase until the direction is reversed. Then the spring force decreases linear in x until it equals the friction again, now in the opposite direction. Reversing the direction again closes the hysteresis loop.

will stretch. The endpoint of the spring moves from its original neutral position x_b^0 to a new x. The spring elongates by $\Delta x = x - x_b^0$ until $F_{pull} = k\Delta x$ equals the friction $F_{friction}$ between the mass and the surface. Then m starts to slide on the surface while the spring remains elongated by $\Delta x_+ = \frac{F_{friction}}{k}$. Simultaneously, the original neutral resting position x_b^0 of the mass is shifted with further increasing x to $x_b^1 = x - \Delta x_+$. When now reversing the direction and pushing the spring back towards the mass, the force F_{pull} decreases with decreasing x. The mass however remains at the position x_b^1. Finally when the spring is compressed by $\Delta x_- = -\frac{F_{friction}}{k}$ of its original length, the mass starts to move in the opposite direction. The neutral position x_b^1 shifts again with further decreasing x to $x_b^2 = x - \Delta x_-$. In this way a hysteresis is created between the force F_{pull} and the position of the endpoint of the spring x, figure 2.8.

This rather crude hysteresis loop can be refined by combining a set $(m_i, k_i)_{i=1}^n$ of n masses m_i and n springs with different spring constants k_i in parallel. When plotting the position of the springs' combined endpoints versus the overall applied force, the hysteresis curve created is piecewise linear. The shape of the hysteresis then depends on the choice for $(m_i, k_i)_{i=1}^n$.

The mechanical model of a stick-slip motion can be transferred to the electric domain as the charging of an ideal hypothetical Maxwell capacitor. The spring constant k corresponds to the inverse $1/C$ of a capacity C, the position x to a charge q and the breaking force $F_{friction}$ to a saturation voltage v. The charging of a capacitor with an increasing charge q continues until the voltage over the capacitor has reached it saturation limit $q = vC$. With further charging the capacity shifts its point of mean charge q_b according to the direction of the applied voltage. The created hysteresis complies with the mechanical model in figure 2.8. Again, a large amount of Maxwell capacitors in series smooths the loop by piecewise linear approximation.In [18], an electromechanical model of a piezo is proposed as shown in figure 2.9. The circuit is basically divided into two parts connected in serial, the first containing the Maxwell capacitors for hysteresis and the second the elements for the electromechanical coupling. The control voltage V_{in} is applied to the circuit and split up into V_{mc} over the Maxwell capacitors and V_t over the electromechanical transformer. The relevant equations are:

$$q = Tx_{mc} + CV_t \tag{2.4}$$

$$V_t = V_{in} - V_{mc} \tag{2.5}$$

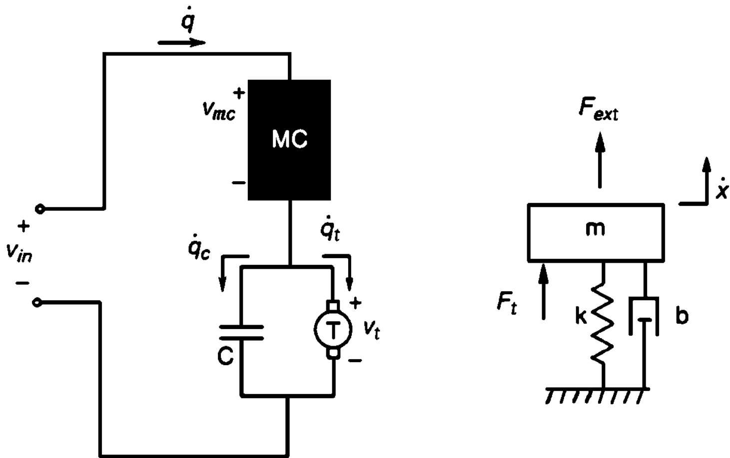

Figure 2.9: Electromechanical model of a piezo ceramic. A voltage v_{in} generate a current $\dot{q}$ which creates hysteresis by successively charging Maxwell capacitors MC. In addition the ceramic acts as a capacitance C and an electromechanical transducer T. Mechanically, the ceramic can be described as a damped mass-spring system. For definitions see text.

$$V_{mc} = \sum_{i=1}^{n} V_i \tag{2.6}$$

$$F_t = TV_t \tag{2.7}$$

$$F_t + F_{ext} = m\ddot{x}_{mc} + b\dot{x}_{mc} + kx_{mc} \tag{2.8}$$

$$V_i = \begin{cases} \frac{(q-q_{b_i})}{C_i} \text{ if } \left|\frac{(q-q_{b_i})}{C_i}\right| < v_i \\ v_i \operatorname{sgn}\left(\dot{q}\right) \text{ and } q_{b_i} = q - C_i v_i \operatorname{sgn}\left(\dot{q}\right) \text{ else} \end{cases} \tag{2.9}$$

where q is the total charge in the ceramic, T is the electromechanical transformer ratio, x is the stack endpoint displacement, C is the linear capacitance in parallel with the transformer. F_t is the transduced force from the electrical domain, m, b and k are the mass, damping and stiffness of the ceramic, and F_{ext} is the force imposed from an external mechanical load. Equation (2.8) describes second order dynamics. In contrast to the high-frequency applications at 100Hz to 1000Hz as discussed in [18], the scan frequency of 0.1 Hz is applied for the experiments discussed here. Therefore a quasi-static movement can be assumed. Additionally the influence of any external force F_{ext} is ignored. Thus (2.8) becomes

$$kx_{mc} = F_t \quad . \tag{2.10}$$

Solving the system of equation for $x(V_{in})$ yields

$$x_{mc}\left(V_{in}, q\left(V_{in}; j\right); j\right) = \frac{T}{k} \cdot \left[V_{in} - \right. \tag{2.11}$$
$$\left. - \left(\sum_{i=j+1}^{n} \frac{q\left(V_{in}; j\right) - q_{b_i}}{C_i} + \sum_{i=1}^{j} v_i \operatorname{sgn}\left(\dot{q}\right)\right)\right]$$

with

$$q\left(V_{in}; j\right) = \frac{\frac{T^2}{k} + C}{1 + \left(\frac{T^2}{k} + C\right)\sum_{i=j+1}^{n} \frac{1}{C_i}} \cdot \tag{2.12}$$
$$\cdot \left[V_{in} + \sum_{i=j+1}^{n} \frac{q_{b_i}}{C_i} - \sum_{i=1}^{j} v_i \operatorname{sgn}\left(\dot{q}\right)\right]$$

where j denotes the index of the latest fully charged Maxwell capacitor

$$j = \max\left\{i \in \{1, 2, ..., n\} \,\middle|\, \left[q - \left(q_{b_i} + C_i v_i \operatorname{sgn}\left(\dot{q}\right)\right)\right] \operatorname{sgn}\left(\dot{q}\right) > 0\right\} . \tag{2.13}$$

Performance analysis

The hysteresis is modelled with $n = 10$ Maxwell capacitors. A least-squares-fit is applied for the set of 23 parameters $\left(T, k, C, (C_i, v_i)_{i=1}^{10}\right)$.This minimizes the squared difference between the experimental data $x_{spm}(V)$ and the model prediction $x_{mc}(V)$:

$$\min_{\left\{T,k,C,(C_i,v_i)_{i=1}^{10}\right\}\in\mathbf{R}^{23}} \sum_{i=0}^{n_{data}} \left[x_{spm}(V_i) - x_{mc}(V_i, q(V_i))\right]^2 \quad . \tag{2.14}$$

The experimental data is taken from largest hysteresis loop of the long tube scanner at the voltage range $[-220\ \mathrm{V}, 220\ \mathrm{V}]$ where $n_{data} = 220$ edges have been observed for both the trace and the retrace branch. The optimization method of Nelder and Mead is chosen [42] because it does not require the first derivative of the function to be minimized. The algorithm is initialized with the parameter values as found in [18]:

$$\begin{aligned} q_{b_i} &= T x_{spm}(V_0) + C(V_0 - V_{mc}) \quad \forall i = 1, 2, ..., 10 \\ j &= 0 \\ & T, k, C, (C_i, v_i)_{i=1}^{10} \ \text{ as in [18]} \\ & (V_0, x_0) \ \text{ as determined by the experiment} \ . \end{aligned} \tag{2.15}$$

The algorithm stopped with a standard deviation of 1.2 μm which corresponds to 0.7% of the complete scan range. The residuals are shown in figure 2.10. The following parameters are found:

parameters
$T = 5.478054\ \frac{C}{\mu m}$
$k = 9.754736 \cdot 10^6\ \frac{N}{\mu m}$
$C = -1.51587 \cdot 10^{-6}\ F$

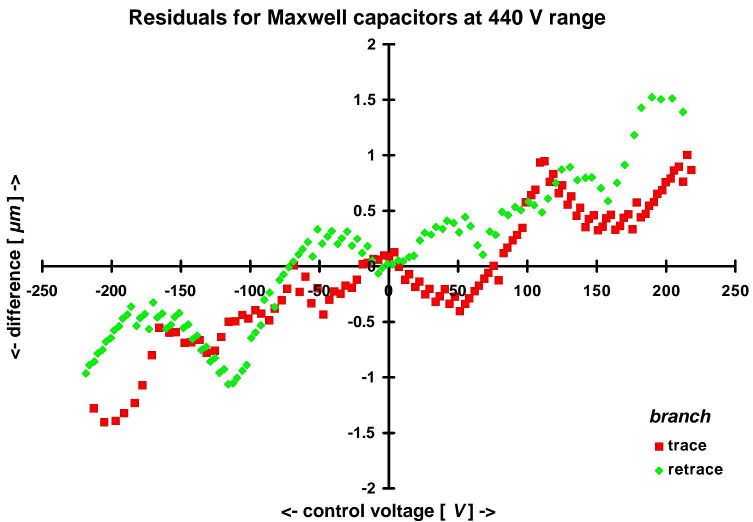

Figure 2.10: Difference in position versus control voltage between the measured hysteresis and the fitted Maxwell capacitors for the voltage range 440 V of the long tube scanner, 1D3000, table 2.2. The piecewise linear residuals relate to the individually active Maxwell capacitor. The overall tilt indicates a further residual systematic error.

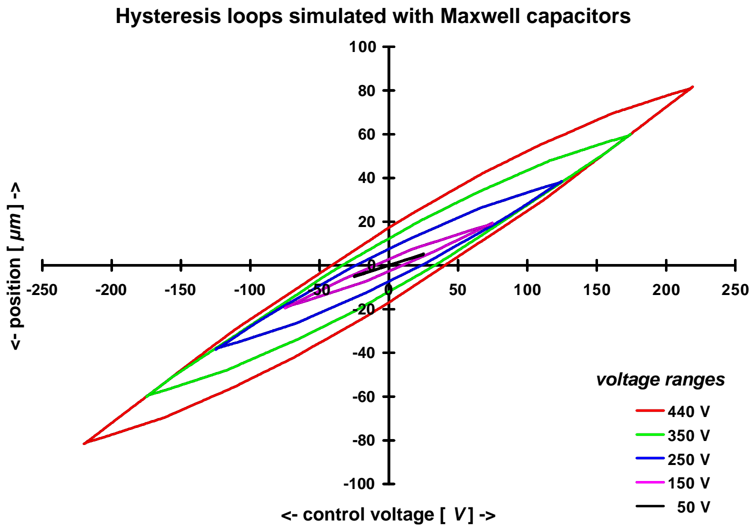

Figure 2.11: Hysteresis loops of position x versus control voltage V as simulated by the fitted Maxwell capacitors. The voltage ranges correspond to those of the experiment with the long tube scanner.

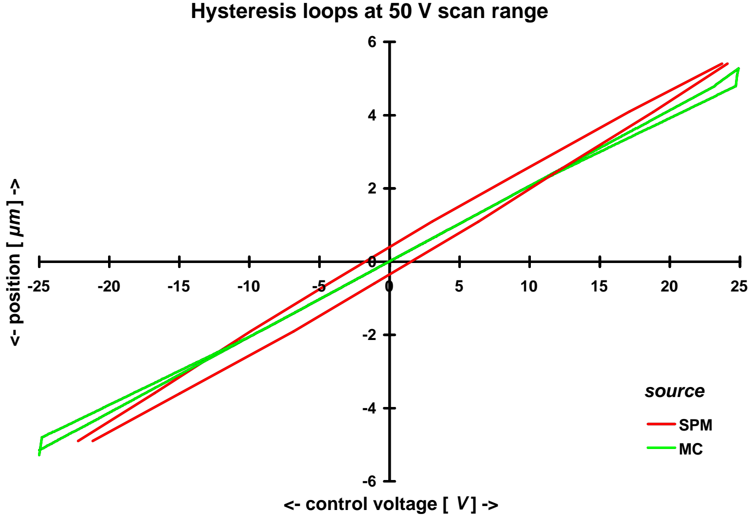

Figure 2.12: Comparing the measured hysteresis from the long tube scanner, 1D3000, table 2.2, versus the simulation with the fitted Maxwell capacitor model MC for a voltage range of 50 V. The impact of the badly fitted negative saturation voltage and capacity can be seen at the turning points of the MC loop. Only 4 Maxwell capacitors are active for this range. Therefore the simulated loop consists of 2x4 piecewise linear functions. This is insufficient to accurately model the measured loop.

Maxwell capacities $[F]$	saturation voltage $[V]$
$C_1 = 3.612157 \cdot 10^{-7}$	$v_1 = -5.823154 \cdot 10^{-1}$
$C_2 = 2.028868 \cdot 10^{-6}$	$v_2 = -6.162183 \cdot 10^{-1}$
$C_3 = 5.003868 \cdot 10^{-6}$	$v_3 = 8.813270 \cdot 10^{-1}$
$C_4 = 2.212764 \cdot 10^{-6}$	$v_4 = 7.514071$
$C_5 = 6.643181 \cdot 10^{-6}$	$v_5 = 5.367377$
$C_6 = 6.385794 \cdot 10^{-6}$	$v_6 = 8.437768$
$C_7 = 1.639462 \cdot 10^{-5}$	$v_7 = 4.814231$
$C_8 = 1.234018 \cdot 10^{-5}$	$v_8 = 7.126937$
$C_9 = 8.992753 \cdot 10^{-6}$	$v_9 = 1.692832 \cdot 10^{1}$
$C_{10} = 9.180117 \cdot 10^{-6}$	$v_{10} = 2.519103 \cdot 10^{1}$

A simulation of hysteresis loops is shown in figure 2.11 for different voltage ranges with the fitted model. Taking a closer look at the parameters reveals that some of them have been determined at a physically wrong value. So a negative capacitance $C = -1.51587 \cdot 10^{-6}$F is found as well as several negative saturation voltages v_1, v_2 of Maxwell capacitors. One might argue that this either corresponds to a necessary preliminary decharging of the capacitors at the beginning of the loop or that physical restrictions must be included in the minimization algorithm. Yet this model lacks further qualifications for a possible online-control. At first there is the need of keeping track which Maxwell capacitors are fully charged or in the process of charging/decharging. Secondly this model is basically a combination of piecewise linear functions. The more linear expressions, that is Maxwell elements $(C_i, v_i)_{i=1}^{n}$, are introduced, the more accurately the hysteresis loop can be modelled. The drawback of this approach is shown in figure 2.12. There the parameters $T, k, C, (C_i, v_i)_{i=1}^{10}$ are set as determined by the fit in order to simulate the loops for smaller scan ranges. As it shows, less Maxwell capacitors are actively contributing to the shape of the hysteresis for smaller scan ranges. Only 4 Maxwell capacitors are active for the smallest scan range $[-25\text{ V}, 25\text{ V}]$, resulting in an identical straight line for trace and retrace except at the turning points. There the negative level of saturation voltage is noticeable as short spikes. Since the level of accuracy is determined only by the amount of Maxwell capacitors, the number needed in order to model small as well as large ranges exceeds the 23 parameters used until now. This is not recommended, on the contrary it is suggested that "a real-time application may be better served by fewer elements..." [18], p73. Therefore this approach turns out to be inapplicable.

2.2.2 Coleman-Hodgdon

The constitutional model of Coleman and Hodgdon has been used to describe the hysteresis in ferromagnetic soft material. Simulated hysteresis loops are in good compliance with those experimentally obtained. The model as described by Coleman and Hodgdon [34],[35] consists of an ordinary linear differential equation for the hysteresis in ferromagnetic materials.

$$\dot{B} = \alpha \left| \dot{H} \right| [f(H) - B] + \dot{H}\, g(H) \tag{2.16}$$

Here H denotes the applied magnetic field, B the magnetic flux and $\alpha \in \mathbf{R}^{+}$. When transferring (2.16) to the experiments with the SPM, the excit-

ing external field H can be considered equivalent to the control voltage V applied to the piezo. Its response, originally B, is recorded as the movement in the lateral plane, say the translation by x in the x direction. Arguing with (2.1), (2.16) can be written as:

$$\dot{x} = \alpha \left|\dot{V}\right| [f(V) - x] + \dot{V}\, g(V) \quad . \tag{2.17}$$

The following conditions are required of the functions $f(V)$ and $g(V)$. $f(V)$ is odd, monotone increasing, piecewise smooth, real-valued and has a derivative f' which has a finite limit $f'(\infty)$ for large V. $g(V)$ is even, piecewise continuous, real-valued with an existing limit for large V so that $g(\infty) = f'(\infty)$.The direction $\mathrm{sgn}(\dot{V})$ of the field V enters the equation by the absolute value $\left|\dot{V}\right| = \dot{V}\,\mathrm{sgn}(\dot{V})$ of V. When the position x at time $t = 0$ is specified $x(0)$ and V is given as a piecewise smooth function of t on $[0, T]$ with $0 < T < \infty$ then the differential equation (2.17) can be solved to obtain x. The resulting curve with the parametrization $t \mapsto (V(t), x(t))$, $0 \le t \le T$, has a slope dx/dV that is well defined for each t at which $\dot{V}(t)$ does not change sign. The control voltage $V(t)$ follows a triangular waveform, thus $\dot{V}(t) \neq 0$ at each t except at the turning points. So within the time period for one triangular flank, equation (2.17) can be safely divided by $\dot{V}(t)$:

$$\frac{\dot{x}}{\dot{V}} = \frac{dx}{dV} = \alpha\, \mathrm{sgn}\left(\dot{V}\right) [f(V) - x] + g(V) \quad . \tag{2.18}$$

It is clear from equation (2.18) that the constitutive equation (2.17) is rate-independent in the following sense: Re-scaling of the function V, i.e. replacement of V by a function $\hat{V}$ obeying $\hat{V}(h(t)) = V(t)$ with h a continuously differentiable function on $[0, T]$ having $dh/dt > 0$ and $h(0) = 0$, leaves the curve of $(V(t), x(t))$ invariant and merely changes the parametrization of the curve to $\tau \mapsto (V(\tau), x(\tau))$, $0 \le \tau \le h(T)$, $\hat{x}(h(t)) = x(t)$. Furthermore, from (2.17) it follows that $\dot{V} = 0 \Rightarrow \dot{x} = 0$. So this model cannot describe a time-dependent response of the piezo to, say, a step function. In the typical working condition of an SPM, a linearly alternating triangular control voltage is applied. Therefore in the analysis of the experiments it can be assumed that the piezo drive has reached a stable state where time-dependent effects are neglectingly small versus the time-independent non-linearities. Equation (2.18) can now be solved for both scan directions. The two solutions $x_{\pm}(V)$ of (2.18) with opposite sign of $\dot{V}$ are distinguished

by indexing them with the direction of the applied field $\mathrm{sgn}(\dot{V})$. The general solution of (2.18) is

$$
\begin{aligned}
x_{\mathrm{sgn}(\dot{V})}(V) &= e^{-\mathrm{sgn}(\dot{V})\alpha V} \cdot \\
&\cdot \left[\int \left(\mathrm{sgn}\left(\dot{V}\right) \alpha f(V) + g(V) \right) e^{\mathrm{sgn}(\dot{V})\alpha V} dV + C_{\mathrm{sgn}(\dot{V})} \right] \quad .
\end{aligned} \tag{2.19}
$$

It can be seen that $g(0)$ is the slope of the virgin curve in the origin and α the rate of transition for dx/dV from $g(0)$ to $g(\infty) = f'(\infty)$. Coleman and Hodgdon propose $f(V)$ piecewise linear and $g(V)$ piecewise constant. This is in good accordance with the properties of ferromagnetically soft materials[34].

$$
\begin{aligned}
f(V) &= \begin{cases} a\,(V + V^*) - bV^*, & V < -V^* \\ bV, & -V^* \le V \le V^* \\ a\,(V - V^*) + bV^*, & V > V^* \end{cases} \\
g(V) &= \begin{cases} u, & -V^* \le V \le V^* \\ a, & V < V^* \text{ and } V > V^* \end{cases}
\end{aligned} \tag{2.20}
$$

Here V^* denotes the threshold voltage, outside of which the piezoelectric material becomes saturated and the hysteresis loop starts to flatten out. During all experiments described in this thesis, no plots of hysteresis loops for the different SPM have indicated that a threshold voltage V^* is passed. The second order derivative d^2x/dV^2 has not changed sign, even for the largest voltage range. The hysteresis never showed any convergence towards a point of saturation. Therefore it can be safely assumed that the piezo scanner operates within the threshold area $[-V^*, V^*]$. As a consequence, the model simplifies to the case $-V^* \le V \le V^*$ with $f(V) = bV$ and $g(V) = u$. Hence V^* is omitted. Equation (2.18) becomes

$$
\frac{dx}{dV} = \alpha\,\mathrm{sgn}\left(\dot{V}\right)[bV - x] + u \quad . \tag{2.21}
$$

The ordinary linear differential equation (2.21) can now generally be solved for both the trace and the retrace direction. The trace direction is defined for $\mathrm{sgn}\left(\dot{V}\right) = +1$, the retrace direction for $\mathrm{sgn}\left(\dot{V}\right) = -1$. The two solutions only differ in the sign of the parameter α. For the sake of simplicity, both solutions will be combined in the same line. The affiliated direction is distinguished by the index t for trace and r for retrace respectively.

$$
x_{t/r}(V) = bV \mp \frac{b-u}{\alpha}\left(1 - C_{t/r}e^{\mp\alpha V}\right) \tag{2.22}
$$

The remaining integration constants $C_{t/r}$ are to be determined by boundary conditions. For the ordinary process of scanning, the control voltage V oscillates between two peaks V_m, V_M, $V \in [V_m, V_M]$. The boundary conditions for a closed hysteresis loop are thus

$$\begin{aligned} x_t(V_m) &= x_r(V_m) \\ x_t(V_M) &= x_r(V_M) \end{aligned} \tag{2.23}$$

Note that the model (2.21) can also be solved for arbitrary boundary conditions, such as occur in the z-direction. Using the system (2.23) as boundary conditions for (2.22) yields the special solution for closed hysteresis loops

$$x_{t/r}(V) = bV \mp \frac{b-u}{\alpha}\left(1 - \frac{2}{e^{\mp\alpha V_m} + e^{\mp\alpha V_M}} e^{\mp\alpha V}\right) \quad . \tag{2.24}$$

The loop is created by an exponentially decaying expression $\pm\frac{(b-u)}{\alpha}C_{t/r}e^{\mp\alpha V}$ towards a linear asymptote bV with a changing offset $\mp\frac{b-u}{\alpha}$ depending on the scan direction, figure 2.13. The linear asymptote $f(V) = bV$ represents the linear response if the hysteresis of the piezo was not present. The coefficient b can thus be interpreted as the electromechanical coupling or the sensitivity of the piezo. At this point it is appropriate to introduce the voltage range $V_R = V_M - V_m$. The voltage range is the peak-to-peak range of the applied control voltage, while the scan range denotes the actually moved distance of the scanner as observable in the image. The choice of $V_M = -V_m$ applies to a typical voltage range symmetric around 0 V, and hence $V_R = 2V_M$.

Performance analysis

The parameters of (2.24) are fitted to the experiments using a least-squares algorithm. The sum of squared differences between the model (2.24) and the experimental data is minimized with respect to the parameters b, u and α. This least-squares fit yields the minimum sum LSF

$$LSF = \min_{b,u,\alpha \in \mathbf{R}} \sum_{i=1}^{n_{data}} \left(x_{t/r}(V_i) - x_i\right)^2 \quad . \tag{2.25}$$

With sample 1D3000, a total of $n_{data,3000} = 2114$ data points are recorded in the voltage range 50 V to 440 V peak-to-peak. In order to evaluate

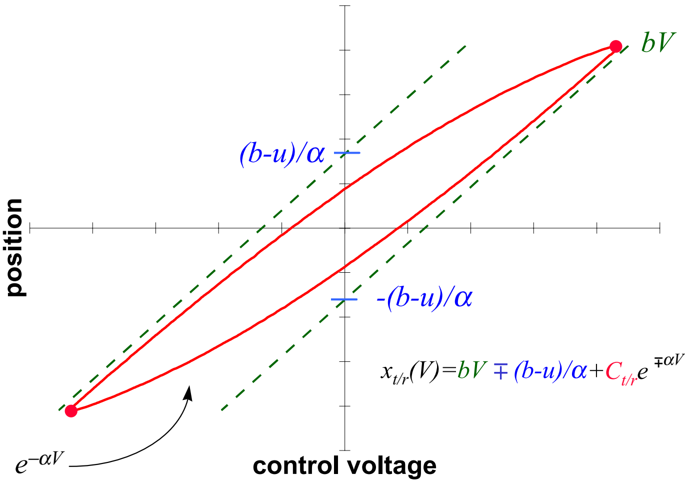

Figure 2.13: Principle of the model for a hysteresis of position x versus control voltage V. A straight line bV is shifted up or down with an offset $(b - u)/\alpha$ depending on the scan direction. An exponential decay $e^{-\alpha V}$ towards this line creates the hysteresis loop. The correct choice of integration parameter $C_{t/r}$ secures that the branches are connected at the upper and lower turning point to form a loop.

the performance of the fit for each scan range individually, the standard deviation

$$\sigma_i = \sqrt{\frac{LSF_i}{n_i - \nu}} \tag{2.26}$$

of the i-th range is calculated. Here LSF_i is the sum of squared residuals and n_i the number of data points for the i-th voltage range. The degrees of freedom of the fit ν is equal to the number of fitted parameters. For this first fit, $\nu = 3$ for b, u and α. The relative error e_i^{rel} for the i-th voltage range is determined by dividing the standard deviation σ_i with the total distance Δx_i covered by the piezo for range i:

$$e_i^{rel} = \frac{\sigma_i(b, u, \alpha)}{\Delta x_i} \quad . \tag{2.27}$$

Thus the quantity e_i^{rel} states the uncertainty of the fit relative to the scanned distance. Multiplying e_i^{rel} with 100 yields the error in percent. The goal of reducing the scan error to one pixel or less can thus be written as

$$e_i^{rel} < \frac{1}{512} \simeq 0.2\% \quad . \tag{2.28}$$

The results of (2.25) are shown in figure 2.18 below, see the uppermost marked "orig." plot. There they are compared with the results of refined models as discussed below. The parameters are determined as $b = 0.47$ $\left[\frac{\mu m}{V}\right]$, $u = 0.19$ $\left[\frac{\mu m}{V}\right]$, $\alpha = 6.68 \cdot 10^{-3}$ $\left[V^{-1}\right]$. The total sum of squared residuals is $LSF = 2505.17$ with relative error ranging from 1-12%. Obviously model (2.24) does not qualify for the purposes of this project. Yet after taking a closer look at the residuals for individual scan ranges, it becomes clear that a systematic error remains after the fit, see figures 2.14, 2.15 and 2.16. By comparing the orientation of the residuals for the smallest, an intermediate and the largest fitted scan range, the changing linear tilt of the residuals becomes obvious. While the residuals lie along a line with positive slope for the 50 V range fig. 2.14, the residuals for the 440 V range are distributed in a non-linear way along a line with negative inclination, fig. 2.16. The residuals for the 275 V range do not show any linear systematic. Therefore it can be concluded that the tilting of the hysteresis loops undergoes a transition from being negative for small ranges to being positive for large ranges. This effect is not modelled by (2.24). There the tilt s of a hysteresis loop, or the slope of the centre line of the loop connecting the lower and upper turning point, is given for a symmetric scan

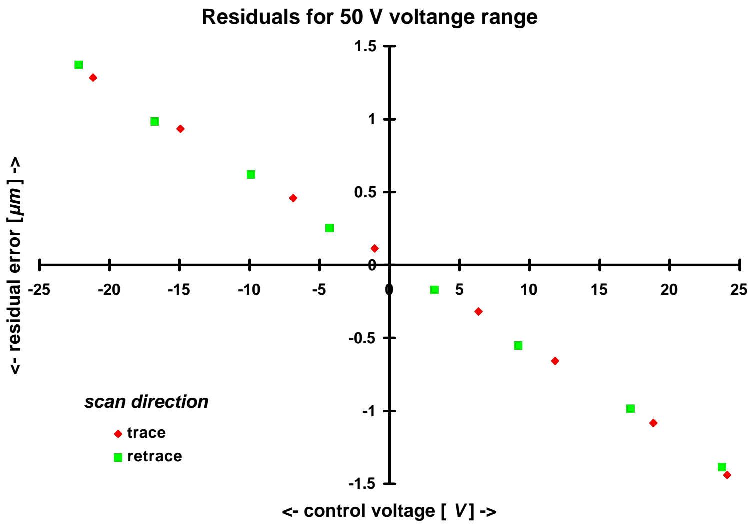

Figure 2.14: Long tube scanner, 1D3000, table 2.2. Residuals of the smallest voltage range at 50 V after the fit. Clearly a linear systematic error with negative slope is visible. Plotted are the residuals in micrometer versus the level of control voltage V.

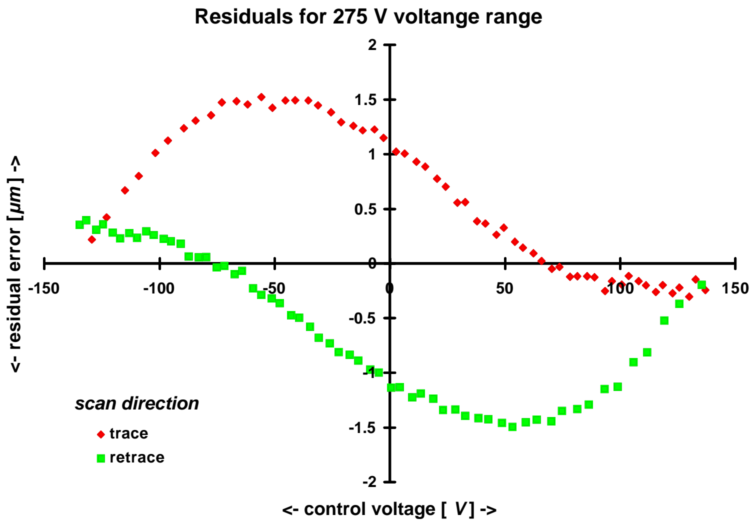

Figure 2.15: Long tube scanner, 1D3000, table 2.2. Residuals of the voltage range at 275 V after the fit. Only a non-linear systematic error is recognizable. Plotted are the residuals in micrometer versus the level of control voltage in V.

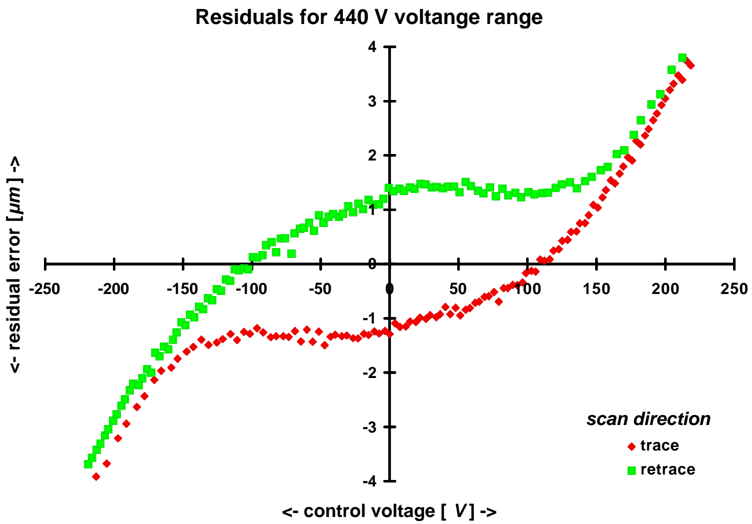

Figure 2.16: Long tube scanner, 1D3000, table 2.2. Residuals of the largest voltage range at 440V after the fit. Plotted are the residuals in micrometer versus the control voltage in V. Now the linear systematic error becomes visible with a positive slope. Superimposed is a non-linear error.

around the origin by

$$s\left(V_M; b, u, \alpha\right) = \frac{x_t\left(V_M\right) - x_t\left(V_{-M}\right)}{2V_M} = b - \frac{b-u}{\alpha V_M}\tanh\left(\alpha V_M\right) \quad . \tag{2.29}$$

Here it is shown that the model of Coleman-Hodgdon does indeed predict a change of the loop's tilt depending on the voltage range $V_R = 2V_M$. For $V_M \to 0 \Rightarrow \frac{\tanh(\alpha V_M)}{\alpha V_M} \to 1$, hence $s\left(0; b, u, \alpha\right) = u$ the slope of the virgin curve. For $V_M \to \infty \Rightarrow \frac{\tanh(\alpha V_M)}{\alpha V_M} \to 0$ and $s\left(\infty; b, u, \alpha\right) = b$. Yet this transition between b and u is obviously not enough in order to describe the experiments. Therefore a new least-squares fit is performed where an individual sensitivity parameter b_i is introduced for each of the 22 scan ranges. Now the sum of squared residuals is reduced dramatically, $LSF_{22} = 14.79$. Plotting b_i versus V_R, the optimized sensitivities increase systematically with the voltage range as shown in figure 2.17.

Although α is responsible for the transition from u to b as seen in (2.29), a fit for individual α_i has not confirmed that the parameter α is a function of the voltage range. The fitted α_i are randomly distributed around the original value α without significantly improving the result of the first fit. As a consequence, different models are set up in order to describe the change of the sensitivity b.

2.2.3 Enhancing Coleman-Hodgdon

Three different models for the changing sensitivity b are compared. The curve as shown in figure 2.17 is modelled by the following functions:

$$b_1(V_R) = b + a_1 V_R + a_2 V_R^2 \tag{2.30}$$

$$b_2(V_R) = b + a_3 \ln(V_R - a_4) \tag{2.31}$$

$$b_3(V_R) = b - a_5 e^{-a_6 V_R} \tag{2.32}$$

These are then inserted into (2.24) replacing the sensitivity b in the linear term:

$$x_{t/r}^j(V) = b_j(V_R)V \mp \frac{b-u}{\alpha}\left(1 - \frac{2}{e^{\mp\alpha V_m} + e^{\mp\alpha V_M}} e^{\mp\alpha V}\right), \; j = 1,2,3 \tag{2.33}$$

The first model (2.30) represents the straight forward approach to describe figure 2.17 by a second order approximation. Its least-squares fitted value

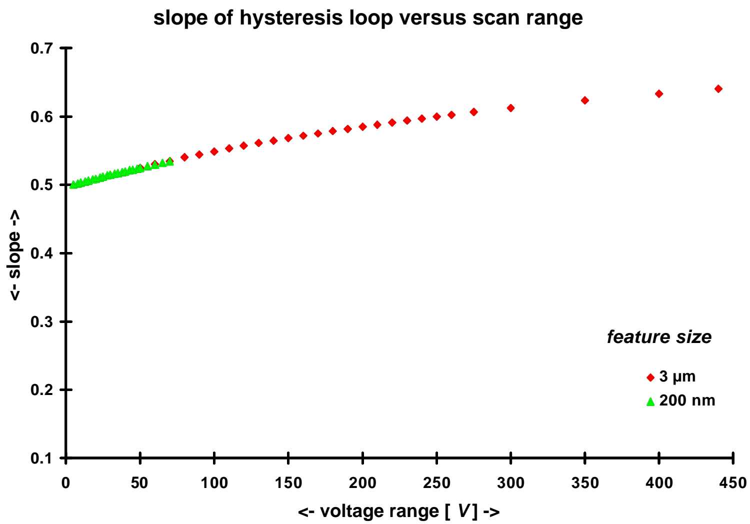

Figure 2.17: Long tube scanner, 1D3000 and 2D200, table 2.2. Sensitivity b of as a function of the voltage range. When fitting individual sensitivities for each observed voltage range, the values of b follow an asymptotic exponential.

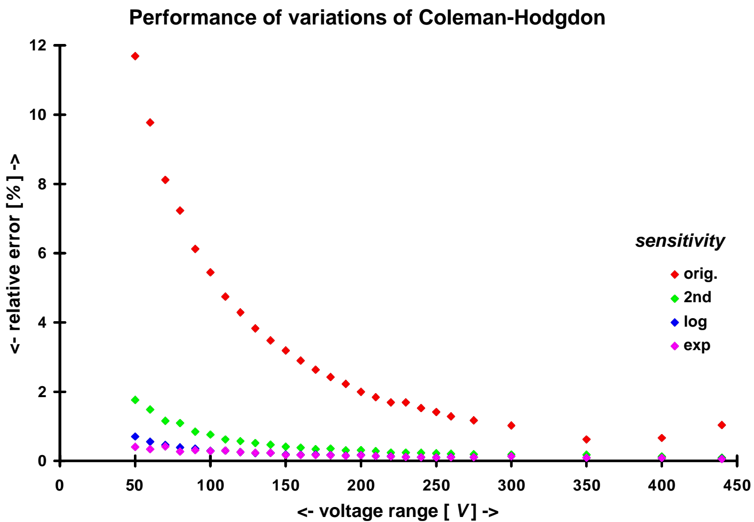

Figure 2.18: Long tube scanner, 1D3000, table 2.2. Comparing the performance of different hysteresis model. Plotted are their relative errors versus the voltage range range. The original model "orig." yields the largest errors. By refining the model successively with a second order polynomial "2nd", a logarithmic "log" and an exponential function "exp", we can reduce the error significantly.

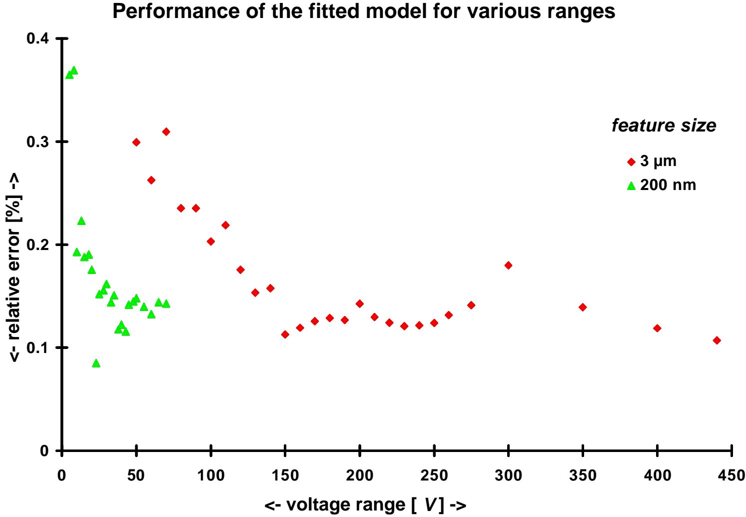

Figure 2.19: Enhanced model for long tube scanner, 1D3000 and 2D200, tables 2.2 and 2.3. For 99% of the complete voltage range, most errors are within 0.2%, corresponding to one pixel. The slight increase at each lower range of the two samples, at around 50 V and 5 V respectively, reflects the measurement uncertainty for ranges with only few sample features per image.

is $LSF_1 = 47.6$. Equation (2.30) clearly is an improvement compared to (2.24). Still the residual errors can be lowered further by using (2.31). There $LSF_2 = 16.42$. Especially for the small scan ranges (2.31) outperforms (2.30). Being monotone functions, both $b_1(V_R)$ and $b_2(V_R)$ predict that the sensitivity continues to increase with increasing scan range V_R. In contrast to this, $b_3(V_R)$ limits the sensitivity by an asymptote that is approached exponentially. (2.32) yields the lowest residual errors of all three models, fig 2.18. The sum of the squared residuals $LSF_3 = 14.92$ is strikingly close to the fit for individual sensitivities b_i with $LSF_{22} = 14.79$. Now the accuracy of (2.24) with the refinement (2.32) is sufficient. The error when simulating the hysteresis mathematically is well within 0.2%, see also [43]. Therefore it is decided to include the data of the sample 2D200 in the least-squares analysis, raising the amount of experimental data points to

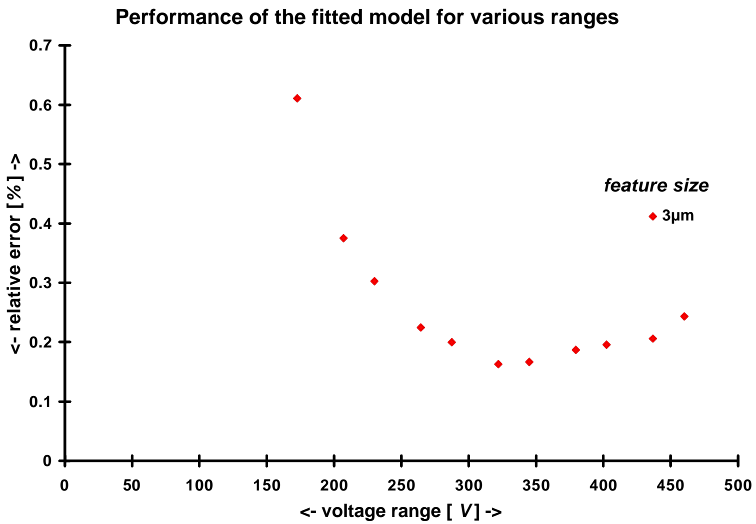

Figure 2.20: Medium tube scanner, 1D3000, tables 2.2 and 2.3. After fitting the experiment, most errors are within 0.3%. The increase at the lower range reflects the measurement uncertainty for ranges with only few sample features per image.

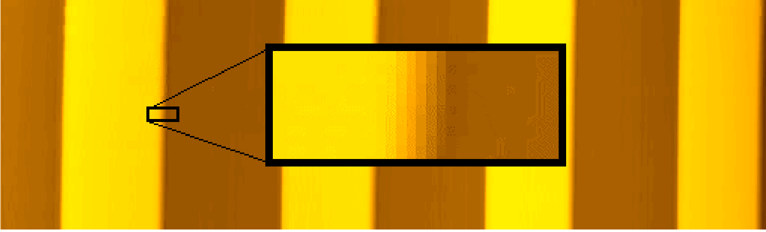

Figure 2.21: Zooming into the SPM image of 1D3000 at a small voltage range. The transitions from top to bottom level cover several pixels. The measurement uncertainty when determining the pixel index of the center of the flank is reflected by the larger residual error of the fit.

$n_{data} = 3736$. Thus the voltage ranges can be reduced from the previous minimum of 50 volt peak-to-peak down to 5 volt peak-to-peak. Hereby 99% of the scanners maximum voltage range of 440 volt peak-to-peak is covered. The performance of the final model

$$x_{t/r}(V) = \left(b - a_5 e^{-a_6 V_R}\right) V \mp \frac{b-u}{\alpha}\left(1 - \frac{2}{e^{\mp\alpha V_m} + e^{\mp\alpha V_M}} e^{\mp\alpha V}\right) \quad (2.34)$$

is shown in figure 2.19.

Most of the relative residual errors are in the order of 0.2% or below. The values of the parameters settled at $b = 0.64 \left[\frac{\mu m}{V}\right]$, $u = 0.38 \left[\frac{\mu m}{V}\right]$, $\alpha = 3.44 \cdot 10^{-3} \left[V^{-1}\right]$, $a_5 = 0.18 \left[\frac{\mu m}{V}\right]$, $a_6 = 3.04 \cdot 10^{-3} \left[V^{-1}\right]$.

The hysteresis loops measured on the medium tube scanner are also fitted to (2.34). The performance of the fit is shown in figure 2.20. Most of the errors are below 0.25% as well. The parameters are determined as $b = 0.18 \left[\frac{\mu m}{V}\right]$, $u = 7.9 \cdot 10^{-2} \left[\frac{\mu m}{V}\right]$, $\alpha = 2.55 \cdot 10^{-3} \left[V^{-1}\right]$, $a_5 = 4.7 \cdot 10^{-2} \left[\frac{\mu m}{V}\right]$, $a_6 = 2.66 \cdot 10^{-3} \left[V^{-1}\right]$.

The reason for an increasing error at the smaller voltage ranges for each sample and scanner, below 100 V and 15 V for the long tube scanner and below 220 V for the medium tube scanner, lies within the increasing measurement error. The higher lateral resolution for small ranges causes the calibration features, the flanks of the lines for 1D3000 and the center of the pits for 2D200 to cover several pixels, fig. 2.21. Therefore the position of the features are only determinable within a few pixels, thus the larger

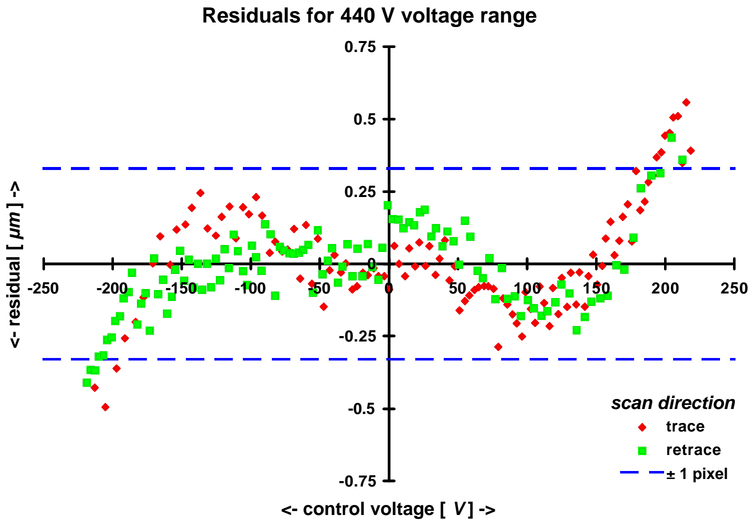

Figure 2.22: Long tube scanner, 1D3000, tables 2.2 and 2.3. Example of the residuals after fitting the hysteresis of the 440V voltage range to the enhanced hysteresis model. The error is well within the range of ± 1 pixel. Merely at the turning points the model performs with an error that is slightly larger than on pixel.

error of the fit. A typical plot of residuals of the final model (2.34) is shown in figure 2.22. The two dotted horizontal lines represent the limit of accuracy for ± 1 pixel. Although the model has a remaining non-linear systematic error which is mostly visible at the turning points, the overall performance is in the order of a pixel. This accuracy is achieved with one model and 5 parameters for almost the complete scan range of the SPM. As a by-product of the analysis, a numerically optimum way of parameter determination has been introduced. This liberates the user from manually adjusting the values of the SPM hysteresis correction.

2.3 Conclusion

Experiments have been performed to measure the hysteresis of an SPM. Two samples have been applied for different voltage ranges. Sample 1D3000 covers the voltage ranges 50 V to 440 V peak-to-peak, while sample 2D200 is used for ranges between 5 V and 70 V peak-to-peak. The frequency has been kept at a constant level of 0.1 Hz. Two models for hysteresis have been discussed. The first model derives the hysteresis from the electric equivalent of a stick-slip motion. This results in an approximation of the hysteresis with piecewise linear functions. A total of 23 parameters is fitted to the measured hysteresis at the voltage range of 440 V. It is required to keep track of the history of changes introduced to the model during the simulation. The fit yielded a standard deviation of 0.7%. Yet some parameters are determined in a physically wrong way. While this can be corrected by using a fitting routine with boundary conditions, the model is not qualified for online application. 23 parameters are not enough to simulate the hysteresis loops for small scan ranges

The other model for hysteresis consists of the solution of an ordinary linear differential equation with 3 parameters. The solution for a closed hysteresis loop is given by a linear asymptote with changing offset for an exponential. This simple analytical model has been fitted to 26 voltage ranges, a total of 2114 data points. Although a tilting of the hysteresis loop with increasing voltage range is inherent within the model, it is found that this does not suffice to describe the tilt of the measured hysteresis loops. An exponential expression is included to consider the tilting of the loops as observed in the experiments. This increases the amount of parameters to 5. The thus enhanced model is then fitted to all observed 48 voltage ranges, a total of

instruments	experiments	results
long tube scanner hysteresis 1D3000 & 2D200	*voltage range* 5 V - 440 V (max) *approx. scan range* 1 μm - 160 μm *scan frequency* 0.1 Hz *see figure* 2.19	*parameters* $b = 0.64$ $u = 0.38$ $\alpha = 3.44 \cdot 10^{-3}$ $a_5 = 0.18$ $a_6 = 3.04 \cdot 10^{-3}$ *modelling error* $\lesssim 0.2\%$
medium tube scanner hysteresis 1D3000	*voltage range* 140 V - 460 V (max) *approx. scan range* 12 μm - 40 μm *scan frequency* 0.5 Hz *see figure* 2.20	*parameters* $b = 0.18$ $u = 7.9 \cdot 10^{-2}$ $\alpha = 2.55 \cdot 10^{-3}$ $a_5 = 4.7 \cdot 10^{-2}$ $a_6 = 2.66 \cdot 10^{-3}$ *modelling error* $\lesssim 0.3\%$

Table 2.3: Summary of the offline fit of the measured hysteresis loops to the enhanced model.

3736 data points. This corresponds to 99% of the total range of motion of the tube scanner. The modeling error of the hysteresis is within 0.2% for all ranges. Only for those ranges where the image resolution increases the measurement uncertainty for the hysteresis, the modeling error is slightly higher, up to 0.4%.

By using a least-squares fitting routine, the numerically optimum values are determined for the parameters of the model. It is conceivable that future calibration procedures relieve the user from manually calibrating the microscope. The SPM can be programmed to record the hysteresis for a set of different voltage ranges and find the appropriate parameters by an automatic image analysis with a succeeding fit.

Chapter 3

Creep

Piezo-electric material is known to display time-dependent relaxation, called "creep". This can be observed when loading a piezo with a mass [20] or applying a step voltage [44], and then measuring the strain as it changes in time. Creep is caused by time-depending changes in the borders and re-orientation of the dipole domains [20]. Typically a logarithmic dependency of strain versus time is assumed. By choosing a logarithmic function, the question of the valid time frame is left open. Since the logarithm is strictly monotone increasing, clearly the piezo would reach any desired expansion if only one waits long enough. For times close to zero, the logarithm shoots towards $-\infty$. The second drawback can be corrected for by an offset in time. The question about the valid time frame however remains.

Manufacturers of software controlled SPM also apply algorithms in order to correct for frequency-dependent image distortions. Typically this involves a logarithmic or 3rd order polynomial with 2-4 parameters.

During the periodic scan process of a SPM extreme situations do not occur such as a single step in the control voltage. It is rather more evident to investigate the time-dependent relaxation that occurs for different scan frequencies during the scan motion. This is presented in this chapter.

Figure 3.1: Long tube scanner, visualization of time-dependency, 1D3000, table 3.1, trace image. The voltage range is constant at 110 V, the scan frequency has been changed as shown while acquiring the image. It is clearly demonstrated how scan frequency affects the scanned distance.

3.1 Experiments

Basically two different set of experiments are performed. The first set is only used for the visualization of creep during the scan motion. From these experiments a model is derived. The second set of experiments is then taken to determine the parameters of the model. The default online corrections of the SPM have been disabled. The expression calibration frame may be introduced here. It means the set of all of voltage ranges and scan frequencies that have been considered for the calibration procedure of the algorithm for one scanner.

3.1.1 Tube scanners

In order to qualitatively examine the effect of different scan frequencies on the hysteresis, the sample 1D3000 is scanned at a constant voltage range of 110 V with the long tube scanner. The frequency is step-wise increased from 0.1 Hz to about 7.6 Hz.

In the second set of experiments, the medium tube scanner has been set

	instruments	
experiments	long tube scanner	medium tube scanner
visualization of time-dependency 1D3000	*voltage range* 110 V *approx. scan range* 60 μm *scan frequency* 0.1 Hz - 7.6 Hz *see figure* 3.1	not performed
hysteresis+creep 1D3000 calibration frame	not performed	*voltage range* 172.5 V - 402.5 V *approx. scan range* 15 μm - 35 μm *scan frequency* 0.1 Hz - 1.4 Hz *see figures* 3.5-3.8

Table 3.1: Experiments to measure hysteresis and time-dependent effect for the two tube scanner. The experiment marked "calibration frame" is used as calibration for the future online application of the correction algorithm. References to figures resulting from the experiments or the following analysis the are also given.

to scan the sample 1D3000 with varying frequency and voltage range. The voltage ranges vary from 172.5 V to 402.5 V. This corresponds to scan ranges from 15.0 μm to 35.0 μm, about 50% of the total scan range. The frequencies range from 0.1 Hz up to 1.4 Hz. 5 different ranges and 6 different frequencies resulted in a total set of 30 experiments. Again the horizontal resolution is set to the maximum of 2048 pixel while reducing the vertical resolution to 16 pixel. One of the resulting 16 pairs of trace/retrace profiles in x-direction is chosen to be analyzed further. A third-order polynomial is fitted to the profile. The pixels closest to the points where the polynomial intercepts the profile are chosen as the center of the flanks. Identifying these flanks with the sample's known period of 3.0 μm yields the position of the flank in micrometer, refer again to fig. 2.5. The level of control voltage is determined by the pixel index of the flank.

3.1.2 Stack scanner

A special designed stack scanner [10], fig 3.2, is equipped with capacitive sensors, so the position of the piezo is recorded immediately without having to use the dimensions of a length standard. This feedback system can be used to linearize the movement of the stage [27]. Typically the scanner position is sampled with 10kHz. This leaves large reserves even for high scan frequencies. In order to reduce the amount of information from 10000 points per second to a reasonable number, the control program has been programmed to down-sample the records to a constant 512 data points (V, x) per hysteresis loop. The maximum voltage range is 350 V peak-to-peak. This yields a scan range of about 5.0 μm.

For visualization of the hysteresis loops at various frequencies, the frequencies have been varied from 0.2 Hz up to 20 Hz while keeping the voltage range constant at 280 V or approximately 2.8 μm.

The experiments done with the short stack scanner are also analyzed for the dependency of creep. The stack scanner is programmed to perform an oscillating movement in the x-direction, driven by a triangular control voltage. The experiments consisted of a recorded sequence of 8 loops after the instrument has scanned the preset range already for 4 times. This was done so that the hysteresis loops could stabilize. Again the loops are sampled with 512 points per period. The frequency is varied between 0.1 Hz and 2.5 Hz, the voltage range between 35 V and 315 V.

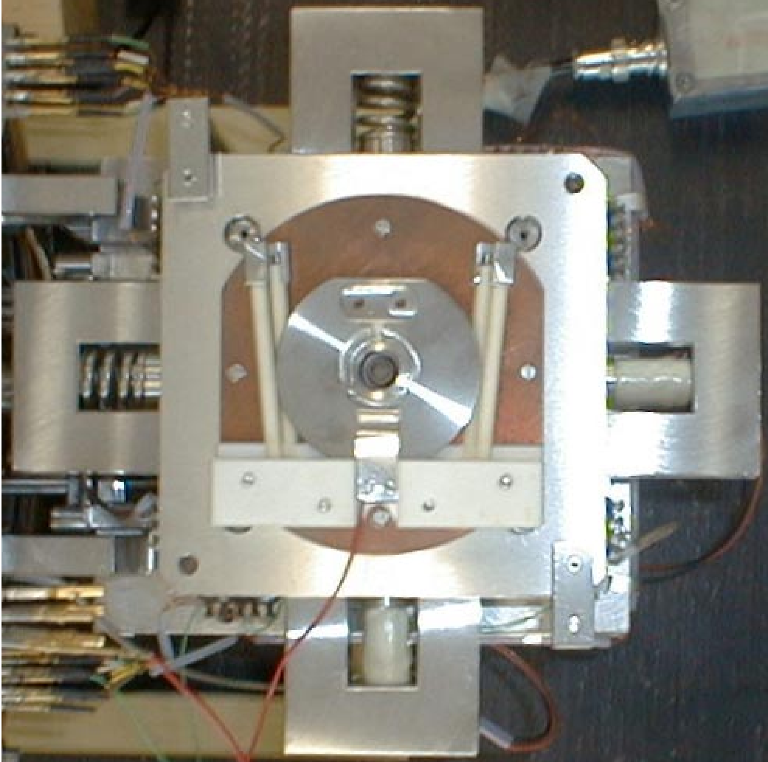

Figure 3.2: Foto of a stack scanner. At the bottom and to the right the piezo stacks can be seen, while the springs to counteract the piezo expansion are mounted on the opposite sides. One side of the square plate in the center is approximately 15 cm.

experiments	short stack scanner
visualization of time-dependency	*voltage range* 280 V *approx. scan range* 2.8 μm *scan frequency* 0.2 Hz - 20 Hz *see figure* 3.3
hysteresis + creep calibration frame	*voltage range* 35 V - 315 V *approx. scan range* 0.4 μm - 4 μm *scan frequency* 0.1 Hz - 2.5 Hz *see figures* 3.9-3.12

Table 3.2: Experiments to measure hysteresis and time-dependent effects for the short stack scanner. The experiment marked "calibration frame" is used as calibration for the future online application of the correction algorithm. References to figures resulting from the experiments or the following analysis the are also given.

3.2 Creep during the scan motion

Time-dependent image distortions are best visualized when comparing a series of images where the voltage range is kept constant and only the scan frequency has been changed. In figure 3.1 the scanned trace image of sample 1D3000 is displayed. The voltage range of 110 V is kept constant through the whole image. The scan frequency has been varied during the scan from top to bottom as written next to the image. It is clearly shown that the SPM scans larger areas at smaller frequencies. Since the scan process can be regarded as quasi-static for frequencies below 1 Hz, dynamics of the scanner can not be the reason for this behaviour. Thus it is concluded that this effect is caused by time-dependent relaxation of the piezo, creep. For small scan frequencies, i.e. for a large time per trace/retrace period, the piezo covers a larger area given more time to expand. This effect is reproducible for all voltage ranges. Corresponding to these experiments, figure 3.3, displays the hysteresis loops of three different scan frequencies. The loops were recorded with the short stack scanner. Again it is verified that the stack scanner behaves qualitatively in the same way as the tube scanners. It is demonstrated that scanning at a constant voltage range with decreasing frequency enlarges the scan range. This is visualized in figure 3.3 as a change of tilt of the loops. Note that the loop for 20 Hz shows influences of dynamics of motion. The area covered by the loop is larger and the turning points are not as sharply pronounced as for the other two loops. Additionally there are damped oscillations immediately after the turning points indicating the transient dynamics of the scanner. Although the data for 20 Hz is not considered in the following analysis, it is plotted here for reason of comparison.

3.3 Modelling creep

In the previous section it has been shown that creep changes the effective sensitivity of the piezo. In order to model the observed time-dependent piezo effects, the following points are assumed.

- The rate-independent hysteresis algorithm (2.24) describes the hysteresis for very fast scanning, neglecting any dynamics.
- On top of this hysteresis, time-dependent piezo creep is superimposed during the scan motion. The slower the scan, the more the piezo can

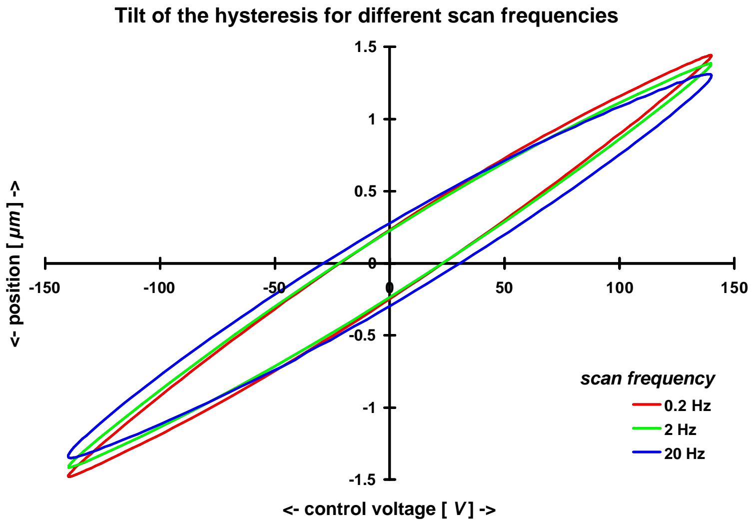

Figure 3.3: Short stack scanner, visualization of time-dependency, table 3.2. Plotting the piezo's position versus the applied control voltage for three different scan frequencies. The lower the frequency, the more tilt of the hysteresis can be observed. Note that the loop for 20 Hz exhibits dynamics, therefore the area covered by the loop is larger than the others.

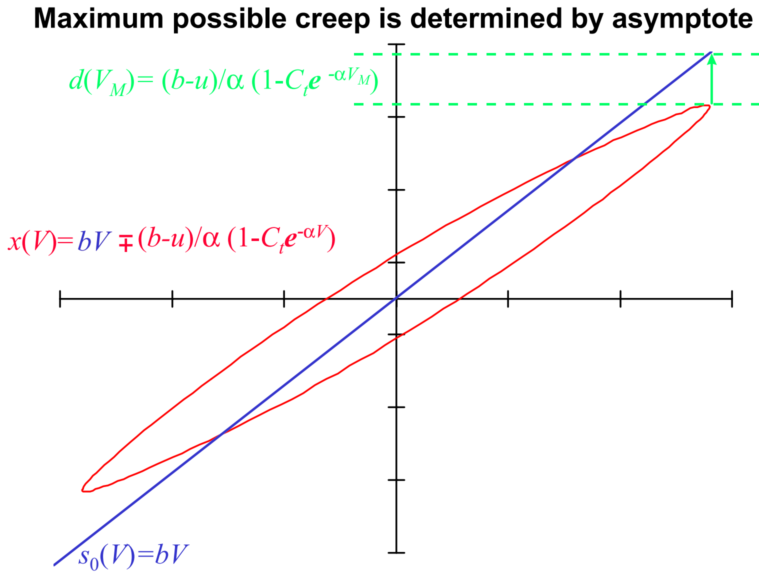

Figure 3.4: Approach to model creep during the scan motion. The hysteresis loop is assumed to tilt towards the line $s_0(V) = bV$ given by the sensitivity coeffient b. The maximum amount the piezo can creep $d(V_M)$ is then the difference between $s_0(V)$ and the upper turning point at $x(V_M)$.

creep, thus the larger the tilt of the hysteresis loop.

- Finally it is assumed that there exists a natural limit to the possible amount the piezo can creep and is set by the line $s_0(V) = bV$ through the origin, figure 3.4.

The original hysteresis model (2.24) builds the base for this approach. Although knowing that a refinement exists (2.34), it is decided to start with the original model. Later it is shown that the derived model for hysteresis and creep includes the earlier obtained enhancement of the hysteresis model. The choice of the limit in the final assumption above, illustrated in fig. 3.4, is evident because the constant b is the piezo's actual sensitivity. So $s_0(V)$ represents the physical limit of the piezo's expansion. An extremely slowly oscillating control voltage would cause the turning points of the loop to lie close to $s_0(V)$. Then the actual maximum possible amount of creep $d(V_M)$ for the upper turning point V_M in the trace direction is determined by:

$$\begin{aligned} d(V_M) &= s_0(V_M) - x_t(V_M) \\ &= \frac{b-u}{\alpha}\left(1 - C_t e^{-\alpha V_M}\right) \quad , \end{aligned} \tag{3.1}$$

see figure 3.4. The amount of creep $x_c(V_M)$ that depends on the scan frequency ω is then a fraction $k(\omega)$ of the maximum creep $d(V_M)$:

$$x_c(V_M) = k(\omega)\, d(V_M) \quad . \tag{3.2}$$

In all of the experiments, only a linear change in the hysteresis loops is observed when varying the scan frequency. A further set of experiments with different voltage offset confirmed the observation that the linear tilt of the loops is symmetric around the centre $V_C = \frac{(V_M+V_m)}{2}$ of the voltage range $V_R = V_M - V_m$ independent of the offset. Only the occurrence of b as sensitivity bV is to be changed in the hysteresis model (2.24). The other parameters entering the non-linear expressions of (2.24) remain at the same value. Therefore the contribution of creep to the hysteresis is modelled to be linear in the control voltage. So for any control voltage during the scan $V \in [V_m, V_M]$, the amount of creep to be added to the hysteresis is

$$x_c(V; \omega, V_M, V_C) = k(\omega)\, d(V_M)\, \frac{V - V_C}{V_M - V_C} \quad . \tag{3.3}$$

The amount of creep $x_c(V; \omega, V_M, V_C)$ is not only depending on the frequency ω and the point of voltage reversal V_M, but also on the voltage range

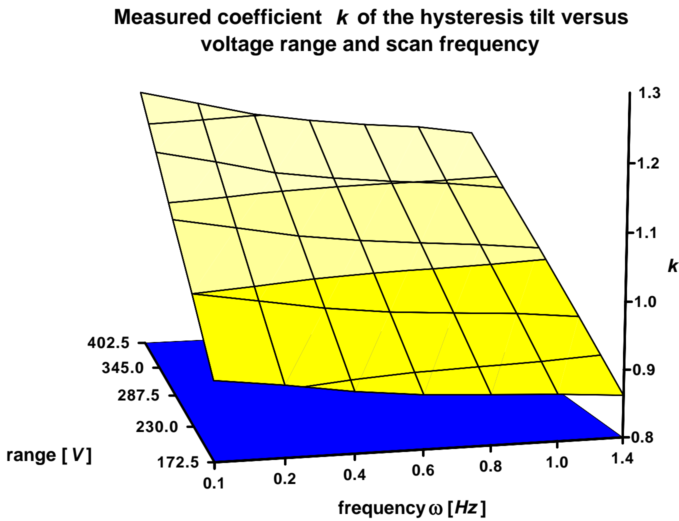

Figure 3.5: Medium tube scanner, 1D3000, table 3.1, calibration frame. Coefficients k_i as found by fitting individual values for all observed ranges and frequencies.

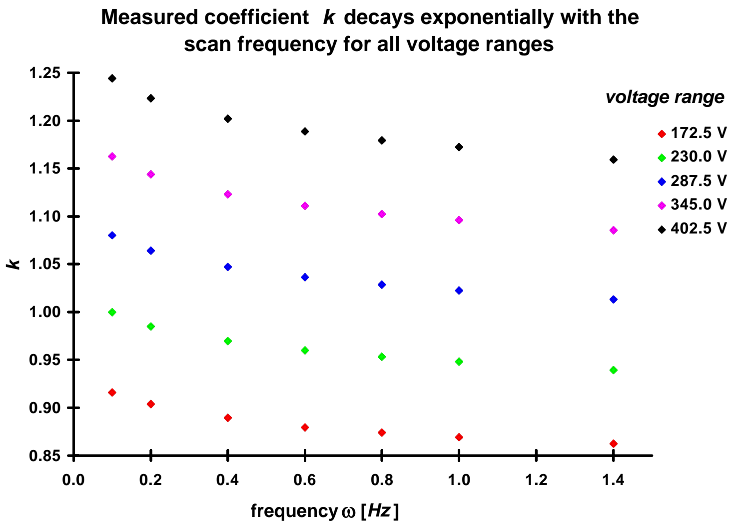

Figure 3.6: Medium tube scanner, 1D3000, table 3.1, calibration frame. Plotting the values of the fitted coefficients k^i versus the scan frequency for different voltage ranges. The exponential decay of the k^i in the frequency is clearly visible for all voltage ranges.

$V_R = V_M - V_m$. Remember that the integration constant C_t in $d(V_M)$ is a function of V_M and V_m and is responsible for the point-symmetry of the hysteresis loops around the centre of V_R at $\left(\frac{V_M+V_m}{2}, x_t\left(\frac{V_M+V_m}{2}\right)\right)$. Therefore $x_c\left(V;\omega,V_M,V_C\right) = -x_c\left(V;\omega,V_m,V_C\right)$. Now it has been shown that (3.3) is independent of the voltage offset. Therefore only a symmetric voltage range $[V_{-M}, V_M]$ with $V_R = 2V_M$ around $V_C = 0$ V needs to be discussed for the sake of simplicity. In order to determine the functional dependency of $k(\omega)$ on the frequency, (3.3) is added to the original (2.24). The resulting equations

$$x_{t/r}(V) = \left(b + k\left(\omega\right)\frac{d\left(V_M\right)}{V_M}\right)V \mp \frac{b-u}{\alpha}\left(1 - \frac{2}{e^{\pm\alpha V_M} + e^{\mp\alpha V_M}}e^{\mp\alpha V}\right) \tag{3.4}$$

are then fitted to the second set of experiments where range and frequency varies. The coefficient $k(\omega)$ is treated as a set of individual parameter k^i_{ω,V_M}, $i = 1,..,30$, one for each experiment. By doing this, the fit yields the optimum values for the k^i_{ω,V_M} for each combination of range and frequency. The thus fitted coefficients are displayed in figure 3.5. The overall sum of squared residuals is $LSF_k = 5.11$.

By forming profiles parallel to the x- and y-axis of the values of the k^i_{ω,V_M} in figure 3.5, it is found that they are exponential in the frequency, fig. 3.5, as well as linear in the voltage range, fig. 3.7. This yields the final model for the complete non-linear movement of the piezo as:

$$k\left(\omega,V_M\right) = \left(1 - A_1 e^{-\frac{1}{\omega\tau}}\right)\left(A_2 V_M + A_3\right) \quad . \tag{3.5}$$

Inserting (3.5) and (3.1) into (3.3) yields

$$x_c\left(V;\omega,V_M\right) = \left(1 - A_1 e^{-\frac{1}{\omega\tau}}\right)\left(A_2 V_M + A_3\right)\frac{b-u}{\alpha}\left(1 - C_t e^{-\alpha V_M}\right)\frac{V}{V_M} \quad , \tag{3.6}$$

$x_c\left(V;\omega,V_M\right)$ is linear in V.

A new sensitivity $\hat{b}\left(\omega,V_M\right)$ is now defined as the sum of the original parameter b and $\frac{k(\omega)d(V_M)}{V_M}$:

$$\hat{b}(\omega,V_M) := b + \frac{b-u}{\alpha V_M}\left(1 - A_1 e^{-\frac{1}{\omega\tau}}\right)\left(A_2 V_M + A_3\right)\left(1 - C_t e^{-\alpha V_M}\right) \quad . \tag{3.7}$$

$\hat{b}(\omega,V_M)$ represents the sensitivity of the piezo as a function of the scan frequency and the voltage range. The general model $\hat{x}_{t/r}(V)$ for hysteresis

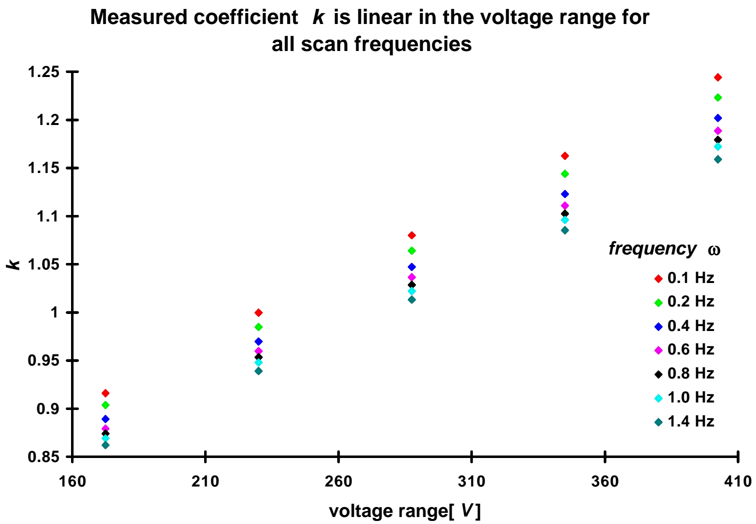

Figure 3.7: Medium tube scanner, 1D3000, table 3.1, calibration frame. Plotting the values of the fitted k^i versus the voltage range for different scan frequencies. The linearity of the k^i in the voltage range is clearly visible for all scan frequencies.

and superimposed creep becomes the sum of the rate-independent closed-loop solution (2.24) and equation (3.3) which is dependent on the frequency ω and via V_M on the voltage range:

$$\begin{aligned} \hat{x}_{t/r}(V) &= x_{t/r}(V) + x_c\left(V;\omega, V_M\right) \\ &= \hat{b}\left(\omega, V_M\right) V \mp \frac{b-u}{\alpha}\left(1 - C_{t/r} e^{\mp\alpha V}\right) \quad . \end{aligned} \tag{3.8}$$

Just as the refined model for rate-independent hysteresis (2.34), equation (3.8) also contains a range dependency and change of tilt that is assymptotic in the voltage range. When the scan frequency is constant as for the experiments fitted to (2.34), the two models act in an equivalent way.

3.3.1 Performance analysis

After the model for hysteresis with superimposed creep has been set up (3.8), again a least-squares-fit is applied to determine the 7 parameters α, b, u, τ, A_1, A_2, A_3 of the model. The overall performance of this final fit to the medium tube scanner is shown in figure 3.8. The fit yields $LSF = 5.33$ which does not differ significantly from the fit for unrestricted k^i at $LSF_k = 5.11$. The optimum parameters are $\alpha = 3.23 \cdot 10^{-3}$ $\left[V^{-1}\right]$, $b = 0.081$ $\left[\frac{\mu m}{V}\right]$, $u = 0.016$ $\left[\frac{\mu m}{V}\right]$, $\tau = 2.666$ $[s]$, $A_1 = 0.081$, $A_2 = 2.78 \cdot 10^{-3}$ $\left[V^{-1}\right]$, $A_3 = 0.681$.

The applicability of the model with the short stack scanner is now verified. Again the parameters of the model (3.8) are fitted to the measured hysteresis loops. The voltage range varied between 35 V and 315 V, approximately 400.0 nm to 4.0 μm, corresponding to 10%-90% of the total voltage range. The scan frequency is changed between 0.1 Hz and 2.5 Hz. The parameters are $\alpha = 0.862$ $\left[V^{-1}\right]$, $b = 0.546$ $\left[\frac{\mu m}{V}\right]$, $u = 0.177$ $\left[\frac{\mu m}{V}\right]$, $\tau = 2.519$ $[s]$, $A_1 = 0.103$, $A_2 = 0.821$ $\left[V^{-1}\right]$, $A_3 = 0.872$. The overall performance is shown in figure 3.9. As with the other microscope, the model can simulate all voltage ranges and frequencies within an relative residual error in the order of 0.3 % and better - with one exception. For small ranges and small frequencies a larger deviation is noticeable. This is due to drift and can be seen in figure 3.10. Plotting the total recorded data, that is all 8 loops, for the voltage range of 35 V at 0.1 Hz, and zooming into the endpoints, reveals the reason for the large modelling error. Obviously the endpoints, and thus the loops, undergo a drift. The residuals of the fit also reveal a

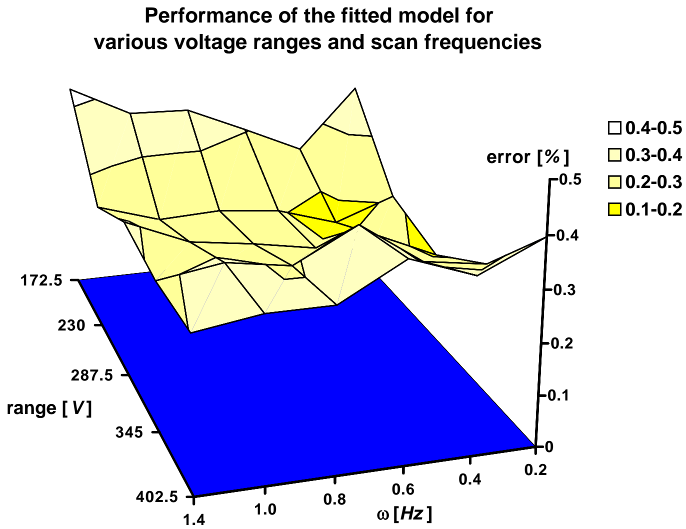

Figure 3.8: Medium tube scanner, 1D3000, tables 3.1 and 3.3, calibration frame. After fitting the model $\hat{x}_{t/r}(V)$, the relative residual error of the fit are well below 0.5% for each observed scan range (175 V - 400 V) and frequency (0.2 Hz -1.4 Hz).

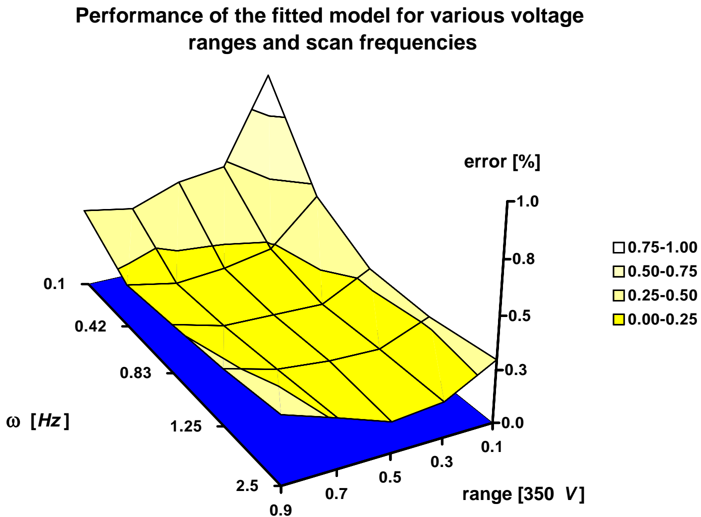

Figure 3.9: Short stack scanner, table 3.2 and 3.3, calibration frame. After fitting the model $\hat{x}_{t/r}(V)$, the relative residual error of the fit are well below 0.5% for most of the observed scan ranges (35 V - 315 V) and frequency (0.1 Hz -2.5 Hz). A large error exists only for the smallest voltage rang and frequency. This is due to drift.

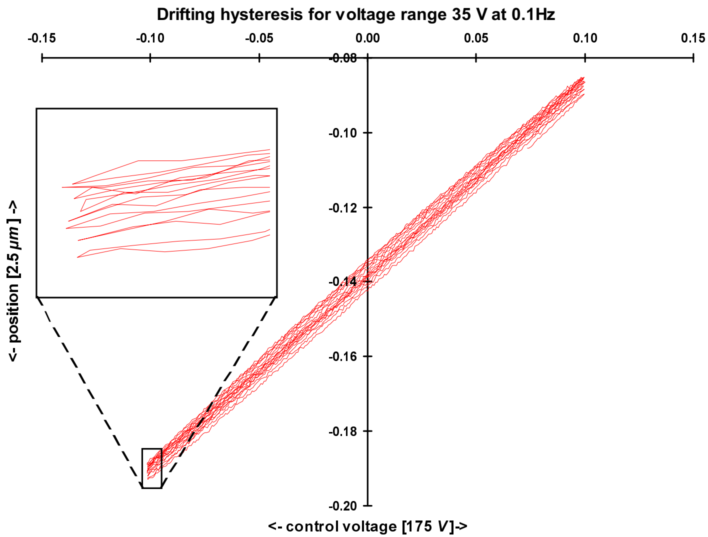

Figure 3.10: Short stack scanner. Eight recorded hysteresis loops at 0.1 Hz and a voltage range of 35 V. This corresponds to a scan range of about 500.0 nm. The uniform drift of the position becomes clearly visible in the displacement of the end points of the hysteresis. The amount of drift is about 0.4 nm/s.

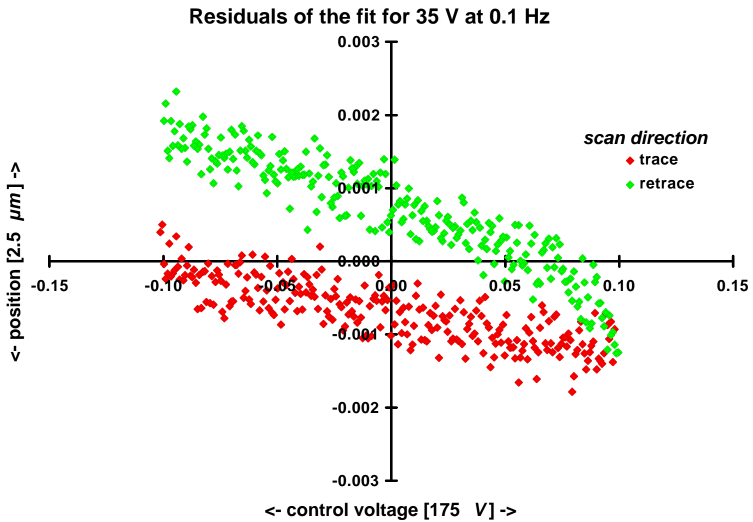

Figure 3.11: Short stack scanner. Residuals of the fit for the voltage range of 35 V at 0.1 Hz. The residuals for trace and retrace are not connected at the lower turning point of the loop due to drift. The amount of drift is about 0.4 nm/s.

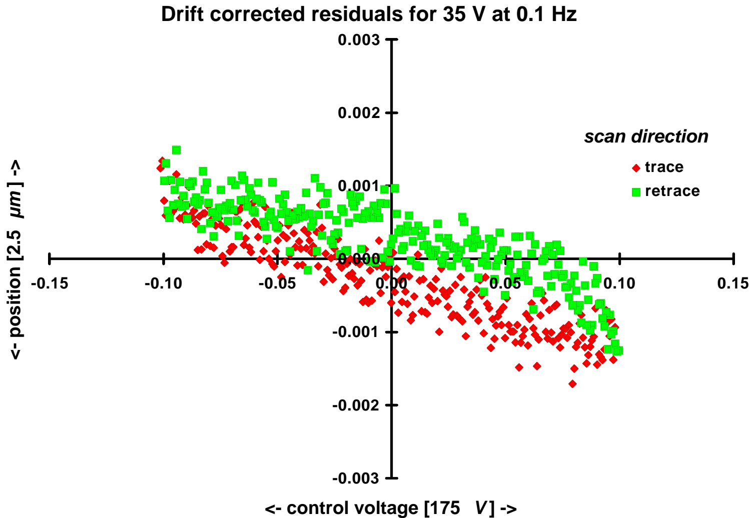

Figure 3.12: Short stack scanner. Residuals for the voltage range of 35 V at 0.1 Hz after drift correction. Now the residuals for trace and retrace connect again at the lower turning point of the loop.

gap between the starting point and the end point of the loop, figure 3.11. The drift is time-dependent. The error it causes vanishes for higher scan frequencies at the same voltage range. Using the data of the voltage range of 35 V, the drift is calculated to be approximately 0.4 nm/s. Due to its small amount it becomes typically observable first at scan ranges below 1.0 μm. Using a linear drift model, the error can be reduced to 0.6%, figure 3.12. However, this drift correction is only included for the sake of completeness. It is not included in the final model for hysteresis and creep because drift is not observed for scan ranges above 1.0 μm.

3.4 Conclusion

The time-dependent relaxation phenomenon called creep has been discussed. Experiments have been performed where the voltage range has

instruments	experiments	results
medium tube scanner 1D3000 calibration frame	*voltage range* 172.5 V - 402.5 V *approx. scan range* 15 μm - 35 μm *scan frequency* 0.1 Hz - 1.4 Hz *see figure* 3.8	*parameters* $\alpha = 3.23 \cdot 10^{-3}$ $b = 0.081$ $u = 0.016$ $\tau = 2.666$ $A_1 = 0.081$ $A_2 = 2.78 \cdot 10^{-3}$ $A_3 = 0.872$ *modelling error* $\lesssim 0.4\%$
short stack scanner capacitive sensors calibration frame	*voltage range* 35 V - 315 V *approx. scan range* 0.4 μm - 4 μm *scan frequency* 0.1 Hz - 2.5 Hz *see figure* 3.9	*parameters* $\alpha = 0.862$ $b = 0.546$ $u = 0.177$ $\tau = 2.519$ $A_1 = 0.103$ $A_2 = 0.821$ $A_3 = 0.872$ *modelling error* $\lesssim 0.3\%$

Table 3.3: Summary of the offline fit of the experiments to the model for hysteresis and time-dependent non-linearity. The parameters determined here are used later in the online algorithm.

been kept constant at 110 V, corresponding to roughly 60.0 μm, while the scan frequency has been changed systematically from 0.1 Hz up to 7.6 Hz. During the process of scanning, creep causes the piezo to move longer distances for smaller frequencies. This has also been displayed as a tilting of the hysteresis loop depending on the scan frequency. Supposing that creep is superimposed on hysteresis and observing that it contributes only to the linear part of the hysteresis model, time-dependent relaxation is modeled to change the effective sensitivity of the piezo. That is, the linear coefficient of the hysteresis model has been complemented to adapt for different frequencies. Further analysis of the experiments showed that the sensitivity changes exponentially in the frequency.

Two further sets of experiments have been performed where systematically

the voltage range as well as the frequency has been changed. The medium tube scanner has been set to scan the sample 1D3000 with varying frequency and voltage range. The voltage ranges vary from 172.5 V to 402.5 V. This corresponds to scan ranges from 15.0 μm to 35.0 μm, about 50% of the total scan range. The frequencies range from 0.1 Hz up to 1.4 Hz. 5 different ranges and 6 different frequencies resulted in a total set of 30 experiments. The short stack scanner has performed experiments driven by a triangular control voltage. The loops are sampled with 512 points per period. The frequency has been varied between 0.1 Hz and 1.4 Hz, the voltage range between 35 V and 350 V, corresponding to .0.5 μm to 5.0 μm. The model is then fitted to the experiments of each scanner. The overall performance of the model is within the aim of 0.2% for both instruments. Only for small ranges, 500.0 nm at low frequencies, 0.1 Hz, instrumental drift of about 0.4 nm/s causes the modelling error to be in the order of 0.9%. A linear drift correction reduces the error to 0.6%.

Chapter 4

Online application

In chapter 2 and 3, the approach has been introduced how to model the hysteresis as observed during the scan movement of a SPM. The equations (3.8) found have proven to describe hysteresis and creep within a residual error of one pixel. The observed hysteresis for different scan ranges and scan frequencies has been simulated by calibrating only one set of 7 parameters. This collimates the goals. Therefore the online application of the model is now treated. It is then included as a control algorithm in the software of a commercially available SPM in order to obtain linear images already during the process of scanning. All that the user has to state is the desired scan range x_r and the scan frequency ω. The algorithm then takes care of calculating the adequate voltage range V_r as well as the actual control voltage $V(x)$. Therefore, the model (3.8) needs to be inverted, thus obtaining the control equation $V(x)$ from the descriptive hysteresis model $x(V)$. The key function of the inverse is formed by the non-analytic LambertW(.), a function called after Johann Heinrich Lambert, a contemporary of Euler and Lagrange around 1760 [45][46]. Finally the performance of the online algorithm is analyzed by calculating the linearity of the obtained images.

4.1 The function LambertW

This chapter begins with the definition of the function LambertW(x) [45][46].

Definition 1 *The function* LambertW(x) *of* x *yields the value so that*

$$\text{LambertW}\left(x\right)e^{\text{LambertW}(x)} = x \quad . \tag{4.1}$$

Note that for $x \leq -\frac{1}{e}$ LambertW(x) is not defined and for $-\frac{1}{e} \leq x \leq 0$ there exist two real solutions. This ambiguity does not pose a problem, since branches of hysteresis loops are inverted that are piecewise monotone, continuous and differentiable. Therefore the inverse exists uniquely as a piecewise monotone, continuous and differentiable function. The actual values of LambertW$\left(x\right)$ are later determined in the control program by use of the Newton-Raphson method to the definition (4.1). This also ensures unambiguity.

In order to invert (3.8), the hysteresis equation is simplified and reduced it to its principal structure. The function to be inverted has the form of

$$x(V) = c_1 V + c_2 e^{c_3 V} + c_4 \tag{4.2}$$

where c_1, c_2, c_3, c_4 are constants with

$$c_1 \quad : \quad = \hat{b}(\omega, V_m) \tag{4.3}$$

$$c_2 \quad : \quad = \pm\frac{b-u}{\alpha}\frac{2}{e^{\mp\alpha V_m} + e^{\mp\alpha V_M}} \tag{4.4}$$

$$c_3 \quad : \quad = \mp\alpha \tag{4.5}$$

$$c_4 \quad : \quad = \mp\frac{b-u}{\alpha} \quad . \tag{4.6}$$

Ignoring these constants, the basic functional dependency of x from V in (4.2) consists of a sum of two expressions: one that is linear and one that is exponential in V:

$$x(V) = V + e^V \quad . \tag{4.7}$$

After substitution of x by e^x in (4.1) follows

$$\text{LambertW}\left(e^x\right)e^{\text{LambertW}(e^x)} = e^x \tag{4.8}$$

or

$$\text{LambertW}\left(e^x\right) = e^{-\,\text{LambertW}(e^x)+x} \quad . \tag{4.9}$$

This equality is important since it tells that the LambertW(.) of an exponential e^x is equal to the exponential of the exponent x minus LambertW$\left(e^x\right)$ itself. Choosing now $V(x)$ as the exponent of the right-hand side in (4.9),

$$V(x) = -\,\text{LambertW}(e^x) + x \tag{4.10}$$

the inverse of.(4.7) is found. This is verified when inserting (4.10) in (4.7). It yields the identical mapping $x = x$. Similarly, the inverse of the hysteresis model (4.2) is given by

$$V(x) = \frac{x - c_4}{c_1} - \frac{1}{c_3}\,\text{LambertW}\left(\frac{c_2 c_3}{c_1} e^{\frac{c_3(x-c_4)}{c_1}}\right) \quad . \tag{4.11}$$

4.2 The control algorithm

When applying the inverse (4.11) online, the calibration parameters α, b, u, τ, A_1, A_2, A_3 must be determined in advance. In chapter 3 the method has been described how to extract the numerically optimal parameters from a set of uncorrected SPM images. This has been done by a least-squares fit between the model (3.8) and the measured hysteresis loops. On top of the parameters, the scan range x_R as well as the scan frequency ω are quantities defined by the user of the SPM. Still one further parameter remains unknown in the inverse (4.11). This is the voltage range V_R that is to correspond to the desired x_R. V_R is part of the constants c_1 and c_2, equations (4.3) and (4.4), hidden in the upper turning point V_M. On first sight, it seems as if this creates a paradoxon. Actually by means of (4.11), the scan range V_R must be determined which results in the desired scan range x_R, yet V_R is needed in order to apply (4.11) as V_R enters as a parameter in both the sensitivity b and the integration constants $C_{t/r}$. An easy way out of this trouble is found by returning to the model function (3.8). Using the calibration parameters in the original model $x(V)$, V_R can be iterated for prior to the application of the inverse. The Newton-Raphson iteration is applied to find the root of the following help function for the range h_R:

$$h_R(V; x_r) = (x_t(V) - x_t(-V)) - x_R \quad . \tag{4.12}$$

Newton-Raphson is initialized with $V_R^0 = \frac{x_R}{b}$. The convergence threshold is set to 10^{-8} It converges rapidly within 5 iterations. The root V^* of (4.12) with $h_R(V^*; x_R) = 0$ as returned by Newton-Raphson is then half of the sought voltage range V_R that corresponds to the scan range x_R. $V_R = 2V^*$ or $V_M = 2V^*$ for a symmetric scan around the origin.

Another obstacle for the online application presents the non-analytic function LambertW(.). Again its value is calculated by applying the Newton-Raphson method to a help function h_L for LambertW(.):

Let $z = \frac{c_2 c_3}{c_1} e^{\frac{c_3(x-c_4)}{c_1}}$ denote the argument of LambertW(.) at the position x, then the help function for the Newton-Raphson iteration is given by

$$h_L(w; z) = we^w - z \quad . \tag{4.13}$$

Newton-Raphson is initialized with $w^0 = z$ and a convergence threshold of 10^{-8}. The root w^* of (4.13) with $h_L(w^*; z) = 0$ provides the needed function value LambertW$(z) = w^*$. The iteration has been tested for a variety of different scan length x_r.With less than 6 iterations, the convergence is sufficiently fast in order to allow online application of (4.11) in real-time.

4.3 Experiments

After receiving the manufacturer's permission to alter the control of the medium tube scanner, the online algorithm is implemented to replace the original online correction. The parameters are set as determined in the hysteresis experiments. Two online experiments with sample 1D3000 are performed with a period of 6 weeks between them. In order to convert the scan range to voltage for reason of comparison with the earlier offline calibration, the value in μm for the scan range is to be multiplied with 11.5 to yield the voltage range in V. The first set of online corrected scans comprises the scan ranges 15.0 μm, 30.0 μm and 36.0 μm recorded at scan frequencies of 0.1Hz, 0.2Hz, 0.5Hz, 1Hz and 1.5Hz. The second set of experiments used scan ranges from 15.0 μm up to 35.0 μm in steps of 3.0 μm. The frequencies are between 0.2 and 1.0 Hz at steps of 0.2 Hz and one at 1.4 Hz. The resolution of the image is set to 2048x16 pixels. This allows a high resolution in x direction and a sufficiently low time of scanning for a complete image.

The control algorithm of the short stack scanner has been reprogrammed to include the correction algorithm. This is done as a Simulink model. A problem occurred when trying to include the Newton-Raphson iteration. The controller of the stage cannot compile algebraic loops of that kind, where the output of an iteration step is used again as an input for the procedure. Therefore a small routine has been written in C, which has been then pre-compiled and linked to the Simulink model. The short stack scanner is programmed to scan ranges from 500.0 nm to 3.0 μm, corresponding to approximately 85% of the maximum range. The frequency is varied between 0.1Hz and 5.0 Hz. Note that the experiments for calibration only

experiments	medium tube scanner
online correction (a) 1D3000	*scan range* 15μm, 30μm, 36μm *voltage range* 172V, 345V, 414V *scan frequency* 0.1 Hz - 1.5 Hz *see figures* 4.1,4.2
online correction (b) 1D3000	*scan range* 15μm - 35μm *voltage range* 172V - 402V *scan frequency* 0.2 Hz - 1.4 Hz *see figures* 4.3-4.7

Table 4.1: Online experiments performed with the medium tube scanner. The online algorithm is calibrated to the relevant experiment "calibration frame" of the previous chapter.

experiments	short stack scanner
online correction capacitive sensors	*scan range* 0.5 μm - 3 μm *voltage range* 35 V - 210 V *scan frequency* 0.1 Hz - 7.6 Hz *see figures* 4.8,4.9
online correction capacitive sensors low frequency	*scan range* 2.5 μm *voltage range* 175 V *scan frequency* 2 mHz *no figure*
online correction capacitive sensors change of offset	*scan range* 0.5 μm - 2 μm *voltage range* 35 V - 140 V *scan frequency* 0.5 Hz, 1 Hz, 2 Hz *scan offset* -52.5 V - +52.5 V *see figures* 4.10-4.12

Table 4.2: Online experiments performed with the short stack scanner. The online algorithm is calibrated to the relevant experiment "calibration frame" of the previous chapter.

covered the frequency range of 0.1 Hz to 2.5 Hz. So the control algorithm is tested outside the specifications of the calibration procedure.

Also on the short stack scanner, a frequency of 2mHz is used to test the quality of the online correction when using the same set of parameters for slow scan movements, such as occurs in the y-axis. For an image of 512x512 pixel, the scan frequency in y-direction is 1024 times smaller than in the x-direction. The performance of the algorithm is tested for slow scanning purposes with a scan range of 2.5 μm at 2mHz.

The online correction is also tested when scanning with an offset on the short stack scanner. The frequency is kept constant at either 0.5 Hz, 1.0Hz or 2.0 Hz. Then the scan range is varied between 0.5 μm and 2.0 μm in steps of 0.5 μm. The offset is then applied to the voltage signal after the algorithm has calculated the control voltage for a symmetric scan. The offset are from -52.5 V to 52.5 V in steps of 17.5 V.

4.4 Linearity analysis

Now the experiments are analyzed after the online algorithm has been included in the control program of the two scanners. Two major errors of an online correction are important.

- The residual non-linearity which determines the degree of image distortion, that is whether a certain distance within the image covers a different amount of pixels in different parts of the image.
- The error in length calibration is the difference between the nominal scan range x_R and the defacto measured range $x'_R = x(V_M) - x(V_m)$.

Determination of x'_R poses a problem, especially for the experiments with the sample 1D3000. There, the detection of length is dependent on the features of the sample, the flanks of the steps in a line pattern. Ideally one flank should coincide with pixel 1, another with pixel 512. Then the scanned distance is found by multiplying the number of periods in the image with 3 μm. The width of one pixel corresponds to approximately 30 nm, so a manual precision placement of the sample at the desired position is almost impossible. Neither the first and/or the last pixel coincides with a flank. Therefore the measured range is estimated in the following way.

The recorded data points (p_i, x_i)per scan range, pixel index p_i and the position x_i of the i-th flank, are used for linear regression. This linear fit

yields the slope $\frac{\Delta x}{\Delta p}$ and offset m of the ideal line through the data as well as the standard deviation σ of the regression. The slope $\frac{\Delta x}{\Delta p}$ represents the linear sensitivity of the scanner. The offset can be neglected because it represents the distance between the point represented by the first pixel and the occurrence of the first flank. This shift is not relevant for the value of the scan range. Now the estimated measured range $\bar{x}'_R$ is given by

$$\bar{x}'_R = n\frac{\Delta x}{\Delta p} \tag{4.14}$$

where n is the total number of pixels, here $n = 2048$. The relative error in length calibration e_l^{rel} is then defined by subtracting x_R from the nominal scan range $\bar{x}'_R$ and dividing the difference with x_R:

$$e_l^{rel} := \frac{\bar{x}'_R - x_R}{x_R} \quad . \tag{4.15}$$

Note that the here defined error e_l^{rel} in fact is a correction, that means the error is actually $-e_l^{rel}$. However, here the choice of definition is done in order to provide a positive error when scanning too long and a negative error when scanning to short. This relates more obviously to the observations. Thus $e_l^{rel} > 0$ indicates a measured range that is longer than the preset range, $e_l^{rel} < 0$ indicates a shorter measured range respectively.

The error of non-linearity e^{rel} is calculated by dividing the standard deviation σ of the regression with $\bar{x}'_R$.

$$e^{rel} = \frac{\sigma}{\bar{x}'_R} \quad . \tag{4.16}$$

The percent values for the error are obtained by multiplying e^{rel} with 100.

4.4.1 Medium tube scanner

Two online experiments are performed with a period of 6 weeks between them. In order to convert the scan range to voltage for reason of comparison with the earlier offline calibration, the value in μm for the scan range is to be multiplied with 11.5 to yield the voltage range in V. The result of the first set of online corrected scans are shown in figures 4.1 and 4.2. The residual non-linearities of this set of experiments are well below 0.3%, figure 4.1, the error in length is in the order of 0.4% and below, figure 4.2.

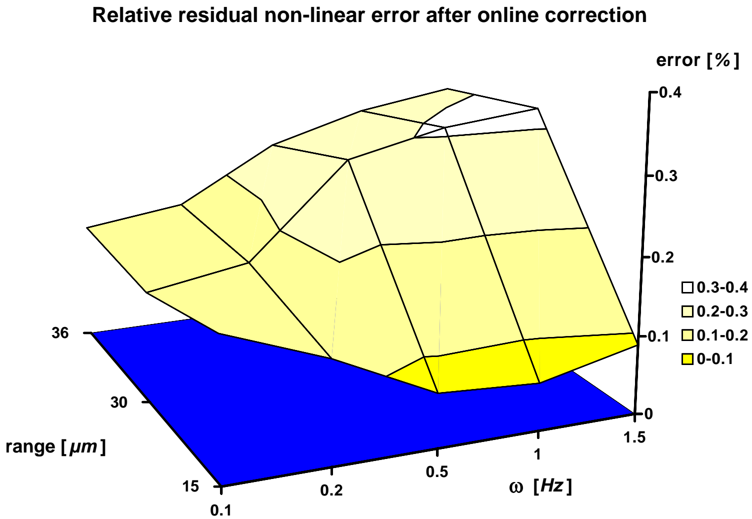

Figure 4.1: Medium tube scanner (a), 1D3000, tables 4.1 and 4.3. Performance of the online correction for the residual non-linear error. The errors are plotted versus scan range and frequency. Most errors are 0.3% and better.

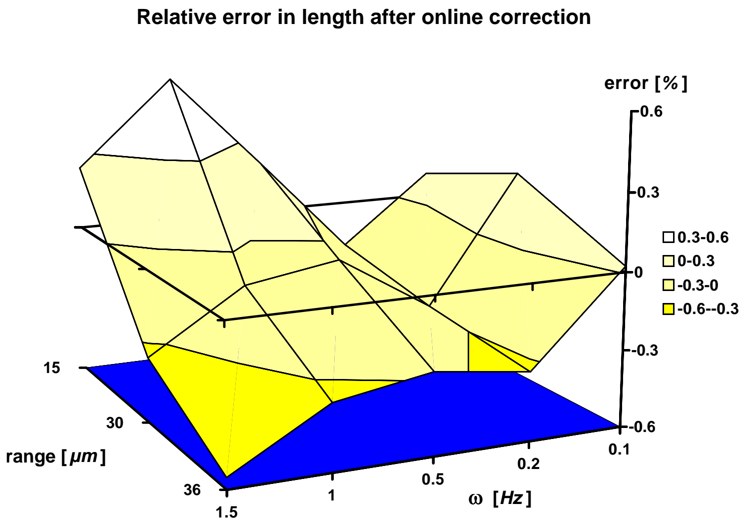

Figure 4.2: Medium tube scanner (a), 1D3000, tables 4.1 and 4.3. Performance of the online correction for length calibration. The errors are plottet versus scan range and frequency. Most errors are within ±0.3%.

The second set of online experiments is done six weeks after the first in order to verify the stability of the instrument with respect to the control algorithm. While the relative non-linear errors are to a large part still within 0.2%, figure 4.3, the error in length seems to have increased to about 1.0%, figure 4.4. Obviously the scanned range is now larger than desired, a distance corresponding to 5 pixel in a 512x512 image for each scan range. The variation of these errors, however, is within a range of ± 0.5% as can be seen in figure 4.5, with the standard deviation of 0.37%. There all scan ranges have been multiplied with a constant factor in order to centre the errors around 0%. This multiplication simulates an offline correction factor which can be used to adjust the dimension of the image offline.

The reasons for this obviously higher sensitivity can be manifold. The temperature of the piezo material at the time of the calibration experiment can be different from the experiments with the online correction. Apart from the well-known fact that piezo material changes its mechanical coupling factors depending on the temperature [20], even within the range of room temperature, experiments have verified this quantitatively for the long tube scanner in [47]. A variation of the sensitivity in the order of 1% must always be taken into account when comparing the measurement of a newly started SPM with one that is "warmed up" after having operated for a few hours. In [47] this phenomenon is described where the long tube scanner was started early in the morning, kept constantly operating until late afternoon while recording images at each hour. It was observed that the scanner's response over the whole day reveals a gradual change in the sensitivity in the order of 0.8% from start till end. Therefore it is concluded that the calibration parameters of control algorithm and the model itself still keep the error of length calibration within 0.37%, but that the overall sensitivity of the instrument displays an offset. For reasons of comparison, the typical distribution of the non-linear residuals after online correction, figure 4.6, is presented as well as with the uncorrected and correct scan for the range of 30.0 μm at 0.6 Hz, figure 4.7.

4.4.2 Short stack scanner

The time period between the calibration and the online application of the model is 8 months. During this time, the instrument was dismantled, moved to a new location and set up again. Figure 4.8 shows the relative errors

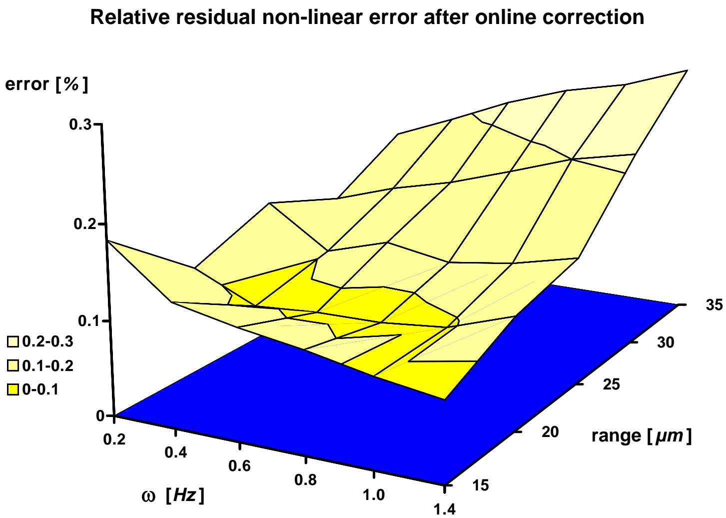

Figure 4.3: Medium tube scanner (b), 1D3000, tables 4.1 and 4.3. Residual non-linear errors after an online correction. The errors are well below 0.5% for each observed scan range and frequency.

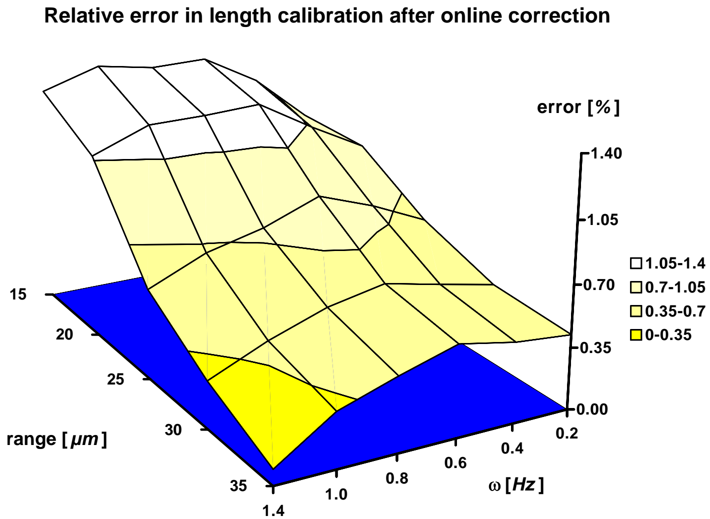

Figure 4.4: Medium tube scanner (b), 1D3000, tables 4.1 and 4.3. Errors in length after online correction per scan range and frequency. Clearly the scanned length is in the order of 1% larger than the nominal. This can be due to arbitrary changes of the properties of the piezo.

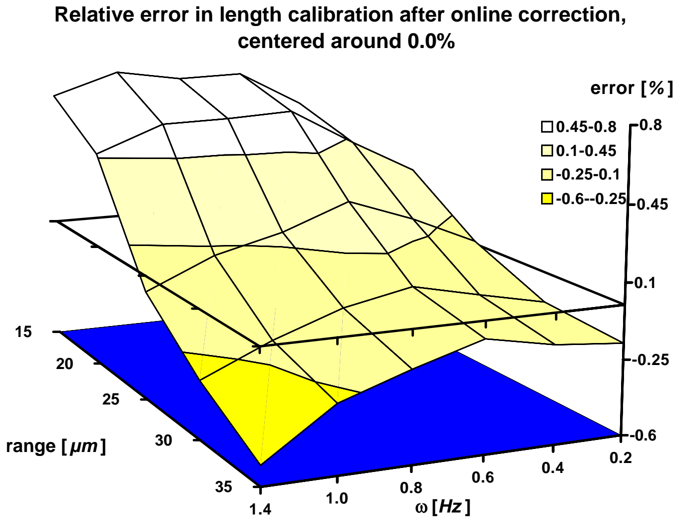

Figure 4.5: Medium tube scanner (b), 1D3000, tables 4.1 and 4.3. The measured and online corrected scan ranges have been multiplied with a constant factor in order to center the errors around 0%. This multiplication simulates an offline correction factor which can be used to adjust the dimension of the image offline after the scanning. Here it is done for purposes of visualisation. The standard deviation of the errors around 0% is 0.37%.

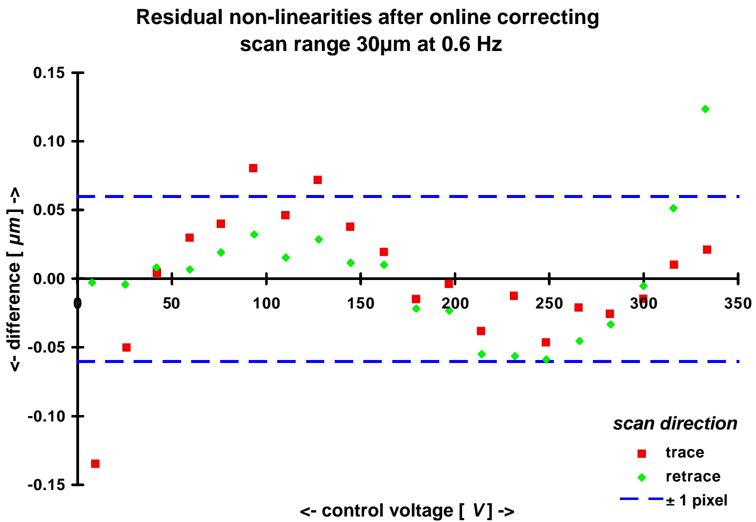

Figure 4.6: Medium tube scanner (b), 1D3000. The residual non-linearity of an online corrected scan. Most residuals are within the belt of ±0.2%, corresponding to ± 1 pixel.

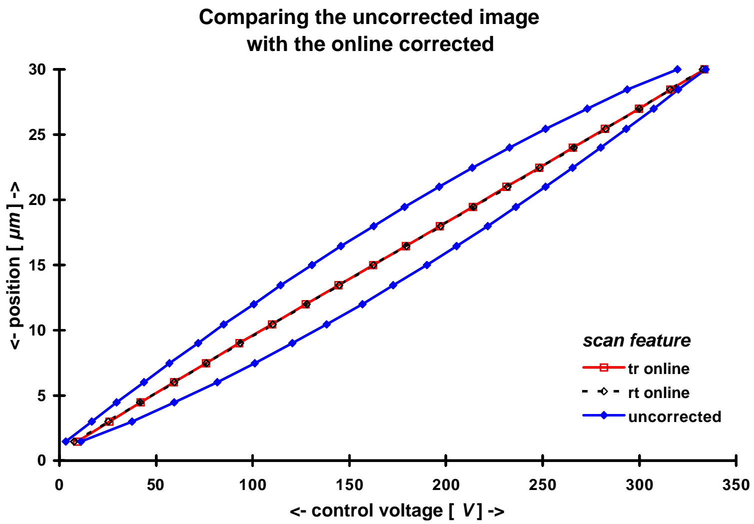

Figure 4.7: Medium tube scanner, 1D3000. An uncorrected hysteresis loop is plotted together with the online corrected loop. The slight shift of the two loops is caused by the arbitrary offset of the position of the sample.

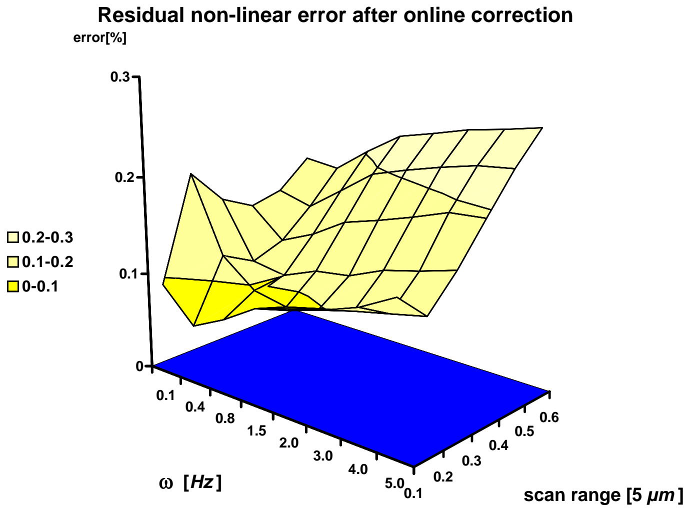

Figure 4.8: Short stack scanner, tables 4.2 and 4.4. The relative residual non-linear errors of the online correction versus scan range and frequency. Even for frequencies above the highest calibration frequency of 2.5 Hz, the overall non-linearity is well below 0.3%.

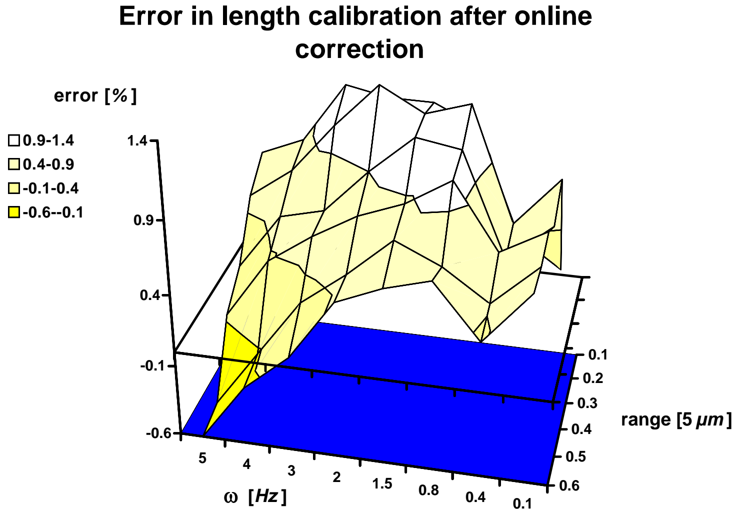

Figure 4.9: Short stack scanner, tables 4.2 and 4.4. The relative error in lenght calibration of the online correction versus scan range and frequency. Note that the frequencies are not equidistant. The main systematic contribution to the errors is given by the scan frequencies. On average it is scanned 0.76% too far, the errors spread around the average with a standard deviation of 0.32%. Above 2.0 Hz, the error decreases monotoniously.

for the residual non-linearity, while figure 4.9 displays the error in length.

The errors for non-linearities are within 0.2% for the majority of scan ranges and frequencies. The continuous increase of the errors for larger ranges and higher frequencies indicates a systematic increase of the residual non-linearity.

The errors in length show large deviations from the nominal scan range. The scanner moves between 1.4% too far and 0.6 % too short. Neglecting the frequencies above 2.0Hz outside the calibration frame, reveals that the scanner always moves too long. For all scan ranges and the frequencies between 0.1Hz and 2.0Hz, the average error is 0.76%. The variation of the error in length around the average, as given by the standard variation of these errors, is only 0.32%. The maximum difference from the average

error is 0.72%. So admittedly the scan range is on average 0.76% larger than desired, yet the variation within this systematic enlargement is 0.32%. When scanning faster than 2.0Hz, that is outside the calibration frame, an almost linear decrease in of the scan length is observable. This is to be expected because the correction for the time-dependent scan error happens in the linear part of the model. It also indicates that the abridgement of the scan range is due to insufficient extrapolation qualities of the creep correction of the algorithm. For the frequencies outside the calibration frame, 3- 5 Hz, the mean error in is 0.33% with a variation of 0.5%.

The opposite behaviour is observable for very slow scans. When scanning a range of 2.5 μm at a frequency of 2 mHz, that is 2 orders of magnitude outside the calibration frame, the actual range is 11 % longer than the nominal range (not shown). The residual non-linearity however remains with 0.28 % within two pixels (not shown). This verifies the conclusion that the scan ranges outside the calibration frame are shortened for higher frequencies and prolonged for shorter frequencies.

Experiments with different scan offset are performed, too. Only the experiments at 1.0 Hz are discussed here representatively. The results of the other two sets at 0.5 Hz and 2.0 Hz are shown in the appendix for sake of clarity, figures B.1 - B.4. Here, figure 4.10 displays the non-linear errors which are well below 0.2%. Figure 4.11 shows the errors in length for different offsets and scan ranges. On average, the actually scanned range is 1.29% larger than the nominal. The deviation is acceptable with 0.37%. At zero offset, the quality of the online correction does not differ from the corresponding earlier experiments symmetric around 0.

When comparing the average error of all scan ranges per offset, figure 4.12, it can be seen that although the average error in length increases with decreasing offset, the variation of the randomly distributed errors per offset is within 0.2%. The systematic decrease in error with increasing offset can be explained by the set-up of the short stack scanner. First of all, a piezo ceramic is known to have different piezoelectric coefficients for applied voltages in or against the direction of polarization [20]. This does not matter for a tube scanner, because there the movement is the result of a combined extension/contraction for opposing tube quadrants. For a piezo stack it is different. There the extension is exclusively in the direction of polarization and the contraction against the polarization. This yields different forces for the two directions. In addition to this effect, the piezo stack is pre-loaded with a spring. When assuming that the spring

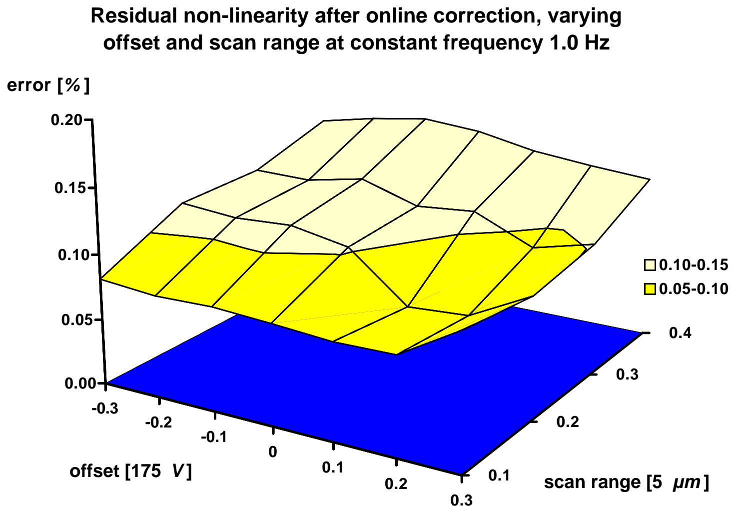

Figure 4.10: Short stack scanner, tables 4.2 and 4.4. Plotting the relative residual errors of non-linearity for different scan offsets and scan ranges at a constant frequency of 1.0 Hz. It is clearly seen that the non-linear error is independent of the offset and well below 0.2 %.

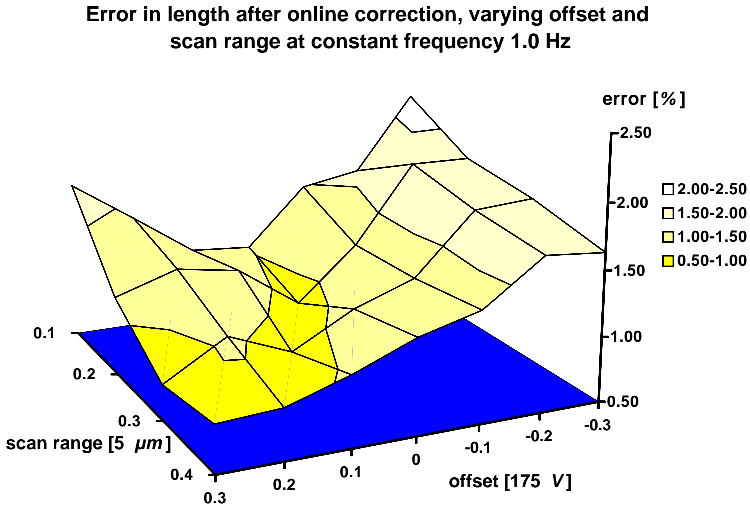

Figure 4.11: Short stack scanner, tables 4.2 and 4.4. The error in length plotted versus the scan range and offset for a constant frequency of 1.0 Hz. The linear decrease with increasing offset coincides with the growing counterforce applied by the spring. For the scan range of 0.1·5.0 μm, an increase of the error in length is noticable. This can be due to different piezo strains for electric field applied in direction of or opposite to direction of polarization.

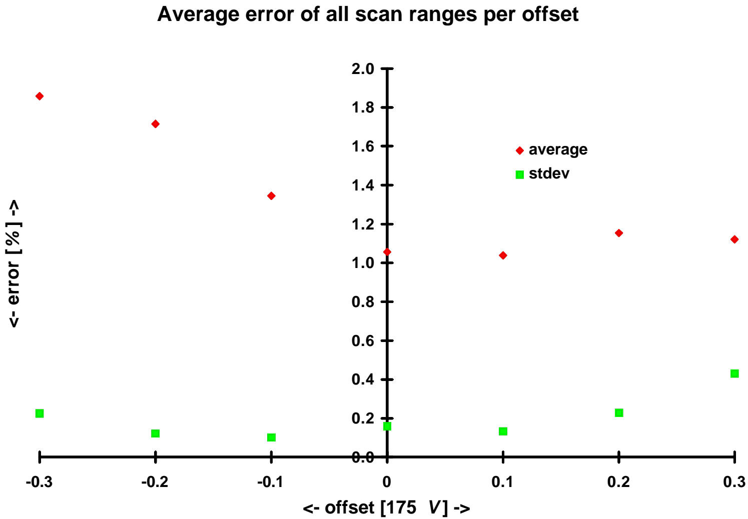

Figure 4.12: Short stack scanner, tables 4.2 and 4.4. The relative errors in length of all scan ranges of each offset are averaged and their standard deviation determined. The error in length is reduced linearly with increasing offset. Only for the positive offsets an increase in error is observable. The linear decrease can be caused by the linear spring. For large offsets, small scan ranges do not cross 0 V. Therefore the increase of the average error and standard deviation for positive offsets can be caused by the unsymmetric force exerted by a piezo stack for voltage applied in direction of or opposite to the direction of polarization. With exception of the largest positive offset, the errors in length per offset only vary within 0.2%.

constant is constant for the observed ranges of extension and contraction, the applied force of the spring on the stack is linear in the displacement. A combination of these two effects can cause the error of length to change with the offset as shown in figure 4.11. The smallest scan range, 500.0 nm, corresponds to a voltage of 14 V, therefore zero volt is not crossed when using the offsets of 52.5 V or -52.5 V. At the offset 52.5 V, the error in length increases again, indicating a change of dominance for the two counteracting effects of spring force and piezo force.

It has been shown that the correction for non-linearity works within pixel accuracy as does the length calibration. Although the short stack scanner covers a distance typically 1% larger than desired, the variation within the errors in length are in the order of 0.3% for all scan ranges and frequencies of the calibration frame. Therefore it is concluded that the online algorithm is stable, but the properties of the instrument have changed. The only major inaccuracy for length calibration occurs when being applied outside the frequency range that was used to calibrate the correction parameters.

4.5 Conclusion

The performance of the online correction has been verified successfully. The combined model of hysteresis and creep has been inverted. The key function of the control algorithm is the function LambertW(.). This function is not analytical. Its values are therefore determined by a Newton-Raphson iteration. With 5 iterations it has proven fast enough for online application. Online experiments have been carried out on two different scanners, one tube scanner and one stack scanner. The scan ranges used are from 15.0 μm up to 35.0 μm for the medium tube scanner, and from approximately 500.0 nm to 3.0 μm for the short stack scanner. The frequency is varied between 0.1 Hz and 1.5 Hz for the medium tube scanner and between 0.1Hz and 5.0 Hz for the short stack scanner. The residual non-linearity of an online corrected scan remains for both instruments within the order of 0.2%. Only the total scanned length varies for both scanner within 1.0% of the nominal value. However, per instrument and set of experiments, the variation is within 0.4%. Thus it can be concluded that the non-linear change of the piezo sensitivity is modelled well by the algorithm for varous scan ranges and frequencies, but the piezo ceramic itself changes its properties and consequently its sensitivity changes due to environmental influences.

medium tube scanner	experiments	results
online correction(a) 1D3000	*scan range* 15μm,30μm,36μm *voltage range* 172V,345V,414V *scan frequency* 0.1 Hz - 1.5 Hz *see figures* 4.1,4.2	*residual nonlinearity* $\lesssim$ 0.3% *variation in length* $\pm$0.3%
online correction(b) 1D3000	*scan range* 15μm - 35μm *voltage range* 172V - 402V *scan frequency* 0.2 Hz - 1.4 Hz *see figures* 4.3-4.5	*residual nonlinearity* $\lesssim$ 0.2% *variation in length* $\pm$0.4% (offset 0.8%)

Table 4.3: Summary of the online experiments with the medium tube scanner.

Experiments outside the calibration frame have also been done. At frequencies above 2.5 Hz, the short stack scanner reveals a decrease in sensitivity of up to 1.5% at 5Hz. For a frequency of 2 mHz, two orders of magnitude smaller than the smallest of the calibration frame 0.2 Hz, the scanned length is 11% larger than the nominal of 2.5 μm. The errors of non-linearity for both the fast and slow scan remain however in the order of 0.2%. Thus it is concluded that the non-linearity is well corrected for all frequencies, yet the length correction only applies for frequencies within the calibration frame. Online experiments with different offsets also return non-linearities better than 0.2%. The error in length however is superimposed with linear dependencies of the sign and magnitude of the offset. This can be caused by the mechanical set-up of a loaded spring to counter the piezo stack.

short stack scanner	experiments	results
online correction capacitive sensors	*scan range* 0.5 μm - 3 μm *voltage range* 35 V - 210 V *scan frequency* 0.1 Hz - 5 Hz *see figures* 4.8-4.9	*residual nonlinearity* $\lesssim 0.2\%$ *variation in length* *inside calib. frame* $\pm 0.3\%$ (offset $+0.8\%$) *outside calib. frame* $\pm 0.5\%$ (offset $+0.3\%$)
online correction capacitive sensors low frequency	*scan range* 2.5 μm *voltage range* 175 V *scan frequency* 2 mHz *no figure*	*residual nonlinearity* 0.3% *error in length* 11%
online correction capacitive sensors change of offset	*scan range* 0.5 μm - 2 μm *voltage range* 35 V - 140 V *scan frequency* 1 Hz *scan offset* -52.5 V - +52.5 V *see figures* 4.10-4.11	*residual nonlinearity* $\lesssim 0.2\%$ *variation in length* $\pm 0.4\%$ (offset $+1.3\%$)

Table 4.4: Summary of the online experiments with the short stack scanner.

Chapter 5

Further results

Further results of the project are presented which are interesting to remark. On top of the nonlinear loop, hysteresis can be the cause for transient yet time-independent relaxation movements once the stationary scan loop is left. This occurs for instance when scan range or scan offset is changed. Then the piezo does not instantaneously reach a new stationary scan loop. The differential character of the model (2.21) allows to simulate the response of the piezo to an arbitrary voltage signal. This also leads to the applicability in the z-direction. The rate-independent model is used to qualitatively explain distortions in the z-direction.

5.1 Changing scan conditions

The hysteresis model (2.21) is based on an ordinary linear differential equation. This means that the solution (2.22) is flexible within the choice of boundary conditions. By changing the boundary conditions it is possible to study the time-independent piezo movement during for example a change of the voltage offset during the scan process. This leads to an image distortion as seen in figure 5.1. There the sample [23] is scanned in an upward direction at a frequency of 0.5 Hz. During the scanning, the x-offset has been changed from -80 V to 0 V. The recorded image displays curved lines although the lines on the sample are still straight at the new scan position. This effect is now simulated with the model.

Figure 5.1: Long tube scanner. Sample 1D3000 is scanned upwards at a frequency of 0.1 Hz. At the centre of the image the scan offset was changed from -80 V to 0 V while the SPM continued scanning. The curvature is typically related to "creep" but also contains time-independent transition.

Let the piezo move from a position (V_0, x_0) in the trace direction. Until now, the voltage range has been $[V_m, V_M]$. When the user now introduces a shift in the scan offset ΔV to new scan range $\left[V_m^{'}, V_M^{'}\right] := [V_m + \Delta V, V_M + \Delta V]$ with $V_0 < V_m^{'} < V_M^{'}$, the initial boundary conditions for the first trace/retrace loop become:

$$\begin{aligned} x_t(V_0) &= x_0 \\ x_t(V_M^{'}) &= x_r(V_M^{'}) \quad . \end{aligned} \tag{5.1}$$

Solving (2.22) involving (5.1) yields:

$$x_t(V) = bV - \frac{b-u}{\alpha}\left(1 - e^{-\alpha(V-V_0)}\right) + (x_0 - bV_0)\, e^{-\alpha(V-V_0)} \tag{5.2}$$

$$\begin{aligned} x_r(V) &= bV + \frac{b-u}{\alpha}\left(1 - 2e^{-\alpha\left(V_M^{'}-V\right)}\right) + \\ &+ \left(x_0 - bV_0 + \frac{b-u}{\alpha}\right) e^{-\alpha\left(2V_M^{'}-V-V_0\right)} \quad . \end{aligned} \tag{5.3}$$

For each successive trace/retrace loop, the scanning occurs within the fixed peak-to-peak interval $\left[V_m^{'}, V_M^{'}\right]$, so boundary conditions similar to (2.23)

are applied. After n completed loops the position $x_r^n\left(V_m^{'}\right)$ is given by

$$\begin{aligned} x_r^n\left(V_m^{'}\right) &= bV_m^{'} + \frac{b-u}{\alpha}\left(\frac{\left(1-\sqrt{q}\right)^2}{1-q}\right) + q^{n-1}\cdot \\ &\cdot\left[\frac{b-u}{\alpha}\left(1-2e^{-\alpha\left(V_M^{'}-V_0\right)} - \frac{\left(1-\sqrt{q}\right)^2}{1-q}\right) + \right. \\ &\left. + e^{-\alpha\left(2V_M^{'}-V_m^{'}-V_0\right)}\left(x_0 - bV_0 + \frac{b-u}{\alpha}\right)\right] \end{aligned} \tag{5.4}$$

with $n > 0$ and

$$q = e^{-2\alpha\left(V_M^{'}-V_m^{'}\right)} \quad . \tag{5.5}$$

Note that for $n \longrightarrow \infty$ (5.5) converges to the solution at $V_m^{'}$ of the retrace direction $x_r\left(V_m^{'}\right)$of (2.24) because $q < 1$ and

$$\frac{\left(1-\sqrt{q}\right)^2}{1-q} = 1 - \frac{2e^{\alpha V_m^{'}}}{e^{\alpha V_m^{'}} + e^{\alpha V_M^{'}}} \quad . \tag{5.6}$$

From (5.4) it follows that the distance between two succeeding points $x_r^{n+1}(V)$ and $x_r^n(V)$ can be written as a ratio of the distance of the initial two points

$$\left[x_r^{n+1}(V) - x_r^n(V)\right] = q^{n-1}\left[x_r^2(V) - x_r^1(V)\right] \tag{5.7}$$

or using (5.5)

$$\frac{\left[x_r^{n+1}(V) - x_r^n(V)\right]}{\left[x_r^2(V) - x_r^1(V)\right]} = e^{-2\alpha\left(V_M^{'}-V_m^{'}\right)(n-1)} \quad . \tag{5.8}$$

So q defines a ratio of convergence and is a function of the material parameter α and scan range $V_R^{'} = V_M^{'} - V_m^{'}$. Let λ denote the width of the area on the sample surface that corresponds to a pixel. Using (5.4) and solving

$$x_r^{n+512}(V) - x_r^n(V) < \lambda \tag{5.9}$$

for n yields a condition for how many scan loops are required in order to produce an image without observable transient hysteretic response over the next 512 scan lines.

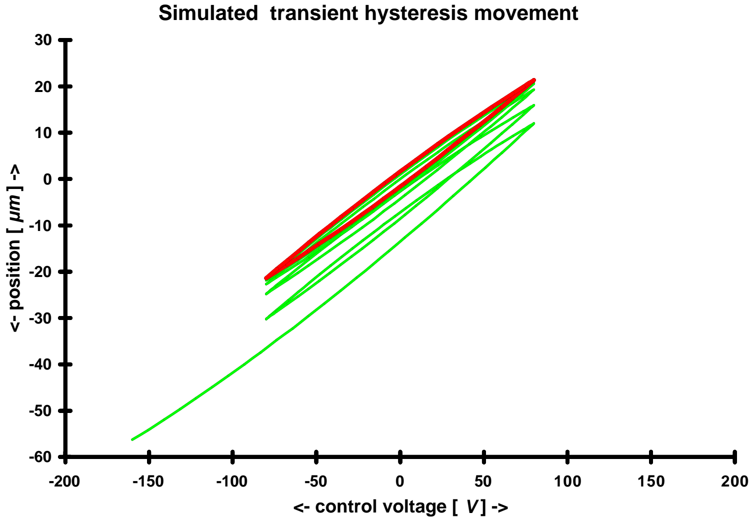

Figure 5.2: Simulated change of voltage offset. Trajectory of the piezos position while shifting voltage range from [-160 V, 0 V] to [-80 V, 80 V]. Due to transient hysteresis (green), the piezo requires several scan periods at the new range in order to converge to a steady loop (red).

In figure 5.2 the simulation of the transient hysteresis movement is displayed along with the final closed loop hysteresis. It demonstrates the movement in the x-direction after the offset of scanning has been changed from -80 V to 0 V. Note that this kind of curvature in figure 5.1 is often interpreted as a time-dependent creep only, although it contains rate-independent movement. For the long tube scanner, (5.9) predicts a stable images after 9 loops which is not the case for the image in figure 5.1. Since the piezo relaxes also in time [19], it is clear that (5.4) cannot completely quantitatively model the observed curvature.

5.2 Overshoot in z at step edges

Figure 5.3 shows the difference between the voltage signal and the true height of the piezo as measured by sensors at a 106.0 nm step. The images are recorded in trace direction on a SPM with capacitive sensors for closed loop feedback control [16]. A profile, figure 5.4, of the differential image reveals overshoots at the flanks of the step in the direction of scanning. These overshoots cannot be explained by a defect of the feedback loop in the z-direction, because this would have impact on both the height signal as well as the converted voltage signal. So the voltage in the z-direction decays exponentially while the piezo remains always at the same height level. The inverse of equation (5.2) allows the simulation of a step in the length domain, say in the z-direction, and monitor the rate-independent response in the control voltage domain. Note that the enhanced model with a time-dependent term (3.8) cannot be applied in the z-direction because the movement is not periodic as in the lateral plane. This is however a condition for the time-dependent algorithm only. The boundary condition is set to start the movement at an initial position (x_0, V_0) with connected branches in the following. In order to observe transient movement due to converging hysteresis loops, an oscillating movement in the length domain is necessary. This can be created by instrumental noise of the feedback loop or simply by surface roughness.

A step of 106.0 nm is simulated, superimposing a hypothetical roughness of 0.5 nm to create tiny loops in the z-direction. The result is shown in figure 5.5. There the converted voltage signal as controlled by the feedback loop is displayed as well as the true surface. The roughness in the z-direction is not visible to the user in neither the voltage signal nor on the surface. However, the exponential decay of the voltage caused by the roughness is visible and coincides qualitatively with the observed overshoot at a step in z.

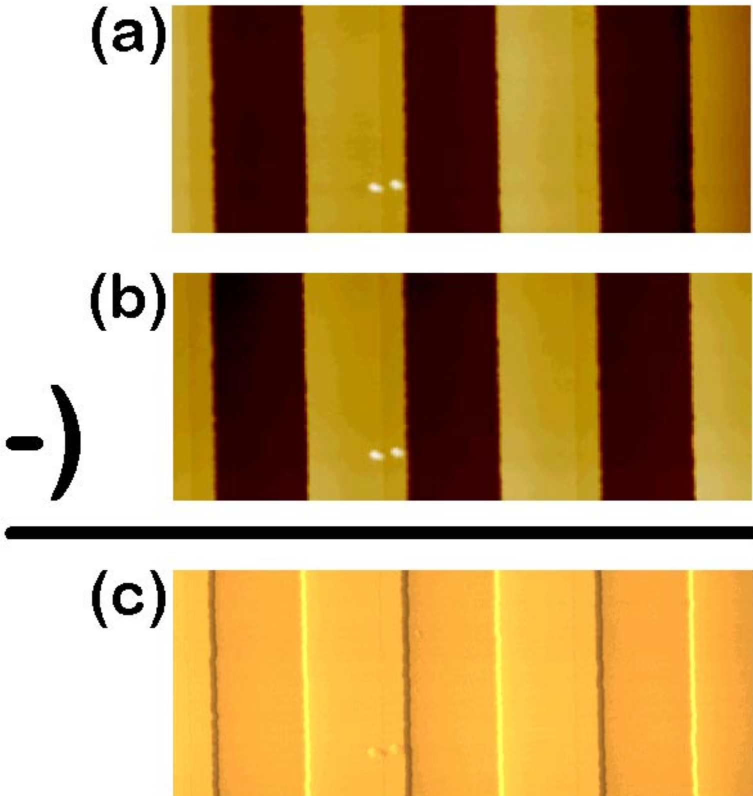

Figure 5.3: Trace scan of 1D3000 on a feedback control SPM with capacitive sensors. Image (a) shows the height of the sample surface as recorded with the voltage signal sent to the piezo. Image (b) is the simultaneously measured height with capactive feedback sensors. Taking the difference (a)-(b) of the recorded height values, the result (c) reveals discrepancies after each step is passed. Two incidentally scanned dust particles can be used as reference points.

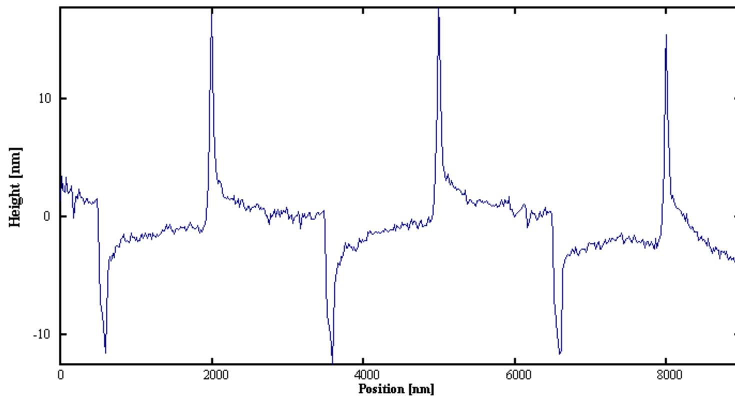

Figure 5.4: Profile of the differential image (c) of the previous figure. The discrepanices are in the direction of the step, that is a positive overshoot at a step upwards and a negative at a step down respectively. This means that the voltage sent to the piezo overshoots and decreases then exponentially in order to keep contact with the piecewise level sample surface.

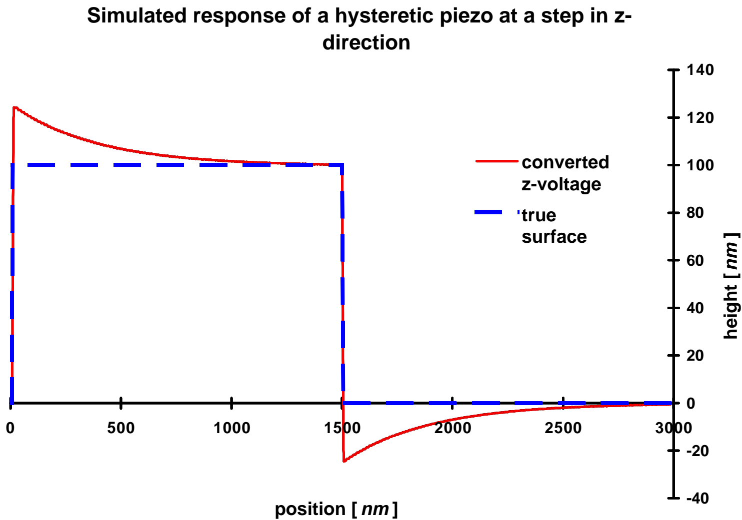

Figure 5.5: Using the model for hysteresis, the overshoot at a step can be simulated as transient hysteresis loops caused by minute noise, such as sample roughness or variations in the control voltage. The shape of the voltage signal is shown that is required in order to maintain a constant contact with the sample surface. Qualitatively, the simulated overshoots resemble the experiment, see previous figure.

Chapter 6

Conclusions

The aim of this project was to develop an applicable online algorithm in order to control the voltage used for an SPM so that the remaining measurement error is in the order of the smallest observable unit - one pixel. This has been achieved for a typical image of 512x512 pixels where one pixel per dimension corresponds to 0.2%. This is summarized in table 6.1.

Three different scanners have been used, one long tube scanner for scan ranges up to 160.0 μm, one medium tube scanner for scan ranges up to 40.0 μm, and one short stack scanner for ranges up to 5.0 μm. Two samples have been applied as reference standard for the tube scanners. The short stack scanner is equipped with capacitive sensors. There the position of the piezo drive is measured directly from the output signal of the sensors.

The model for hysteresis consists of the solution of an ordinary linear differential equation with 3 parameters. This simple analytical model has been fitted to 26 voltage ranges, a total of 2114 data points. An exponential expression is included to consider the tilting of the hysteresis loops for varying ranges as observed in the experiments. This enhancement increases the amount of parameters to 5. These are then fitted to all observed 48 ranges from 1.0 μm to 160.0 μm for the long tube scanner, a total of 3736 data points. This corresponds to 99% of the total range of motion of the SPM. The modeling error for the hysteresis is well within 0.2% for most ranges.

The second major source of image distortion is time-dependent relaxation

	instrument		
experiments	Long tube	Medium tube	Short stack
offline *hysteresis* chapter 2	*volt. range* 5 V-440 V (99% of max) *frequency* 0.1 Hz *error of fit* $\lesssim$ **0.2**%	*volt. range* 140 V-460 V (70% of max) *frequency* 0.5 Hz *error of fit* $\lesssim$ **0.3**%	not performed
offline *hysteresis* *creep* calib. frame chapter 3	not performed	*volt. range* 172 V-402 V (50% of max) *frequency* 0.1Hz-1.4Hz *error of fit* $\lesssim$ **0.4**%	*volt. range* 35V - 315V (80% of max) *frequency* 0.1Hz-2.5Hz *error of fit* $\lesssim$ **0.3**%
online *hysteresis* *creep* chapter 4	not performed	*scan range* 15μm-35μm (50% of max) *frequency* 0.2Hz - 1.4 Hz *non-lineaity* $\lesssim$ **0.3**% *variation* *in length* $\pm$**0.4**%	*scan range* 0.5μm-3μm (50% of max) *frequency* 0.1Hz - 2Hz *non-lineaity* $\lesssim$ **0.2**% *variation* *in length* $\pm$**0.4**%

Table 6.1: Summary of the main results. For an image consisting of 512x512 pixels, the errors of modelling the non-linear behaviour of the piezo scanner piezo offline is in the order of 1-2 pixel, 0.2-0.4% and better. The online version of the algorithm corrects for the non-linearities within 1-2 pixel, 0.2-0.4% and better, too. At least half of the total possible scan/voltage range has been checked. The scan frequencies are those typically applied for a scan. It is concluded that the algorithm presented in this thesis can correct for the non-linearities of any piezo-driven scanner, independent on the piezo geometry (tube or stack).

phenomenon, also known as creep. The model for hysteresis is adapted to also describe the non-linear change of piezo-sensitivity for different scan frequencies, increasing the number of parameters to 7. Two sets of experiments have been performed where systematically the voltage range as well as the frequency has been changed. The medium tube scanner has been set to scan with varying frequency from 0.1 Hz up to 1.4 Hz and varying voltage range from 15 μm up to 35 μm. Five different ranges and six different frequencies resulted in a total set of 30 experiments. When fitting the parameters of the model to them, errors better than 0.3% are returned. The short stack scanner has performed experiments driven by a triangular control voltage. The loops are sampled with 512 points per period. The frequency has been varied between 0.1 Hz and 1.4 Hz, the range between 0.5 μm and 5.0 μm. Here the fit of the model also yielded an error in the order of 0.2%.

By using a least-squares-fit for the determination of the parameters, the calibration of the model's parameters yields the numerically optimum. This stands in contrast to the calibration procedures of commercial SPM. There the user is required to perform a set of experiments manually and adjust the parameters by eye-sight. The numerical method does not only determine the parameters objectively and to a higher accuracy, but it also offers the possibility to automatize the process of calibration. In principle the user now only needs to insert a certified length standard at the right orientation into the SPM, press a button "calibration" and return after some time when the calibration is done. In the meantime a pre-programmed set of images with different voltage ranges and scan frequencies has been recorded, analyzed for its features that determine the length, and fitted to the correction model.

After the model for hysteresis and creep has proven to simulate the measured image distortion accurately, it has been inverted to yield the algorithm used for online correction. The key function of the control algorithm is the function LambertW(.). The medium tube scanner and the stack scanner have been programmed to incorporate the online model. The scan ranges are from 15.0 μm up to 35.0 μm for the medium tube scanner, and from approximately 500.0 nm to 3.0 μm for the short stack scanner. The frequency is varied between 0.1 Hz and 1.5 Hz for the medium tube scanner and between 0.1Hz and 5.0 Hz for the short stack scanner. The residual non-linearity of the online corrected scan remains for both instruments within the order of 0.2%. Only the total scanned length varies for both scanner

within 1.0% of the nominal value. However, viewed isolated per instrument and set of experiments, the variation of the errors in length is within 0.4%. Thus it can be concluded that the algorithm describes the non-linear change of piezo sensitivity very well for different scan ranges and frequencies, but the piezo ceramic itself changes its properties and consequently changes its overall sensitivity due to environmental influences. Experiments outside the calibration frame have also been done. At frequencies above 2.5 Hz, the short stack scanner reveals a decrease in sensitivity of up to 1.5% between 2.5 Hz and 5Hz. Thus it is concluded that the non-linearity is well corrected for, yet the length correction only applies for frequencies within the calibration frame.

Further discussion of the properties of the rate-independent model revealed that scan distortions often related to time-dependent creep also include a rate-independent component of transient hysteresis. At a sudden change of scan conditions, such as a change in scan offset, the hysteresis undergoes a transient movement and converges to a new stable position after a certain amount of loops have been performed, independent of the scan frequencies. This behaviour in the lateral plane is also seen for the piezo response in height. Overshoots at steep edges have been qualitatively simulated as transient hysteresis.

Summarizing it is concluded that the aim of this work is achieved. The residual image distortions after online correction are pixel-sized. One set of 7 parameters is universally valid for all scan ranges and frequencies. The calibration of the algorithm can be performed automatically with a numerically optimum fit algorithm. The rate-independent model for hysteresis is flexible enough to model the lateral periodic scan motion as well as arbitrary changes, such as a new scan offset or even high steps on the sample surface in the z-direction.

Appendix A

Recorded images

In this section of the appendix, further SPM images are shown. They have been recorded in pairs of trace and retrace in order to measure the hysteresis. Two reference standards have been used. One line pattern 1D3000 with a reference period of 3.0 μm and a 2-dimensional grating 2D200 with a reference pitch of 200.0 nm. During the recording of a pair of images, the voltage range has been changed systematically in order to obtain more hysteretic data at once. The sample 1D3000 is applied for voltage ranges between 50 V and 440 V peak-to-peak, while 2D200 is used for voltage ranges between 5 V and 70 V peak-to-peak. Only one representative pair of image is displayed for sample 2D200, for the ranges from 15 V to 30 V.

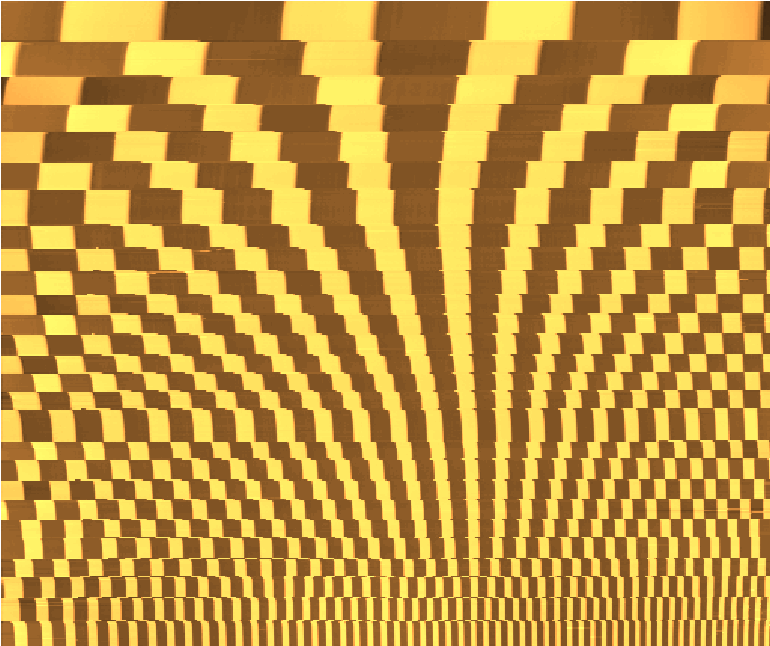

Figure A.1: Long tube scanner, tables 2.1 and 2.2. A sample of lines spaced by 3.0 μm is scanned in trace direction. The height step between light and dark is 106 nm. The scan size is changed during the scan from top to bottom. The voltage ranges are between 50 V (top) to 440 V (bottom). Note that the patterns are stretched on the left while compressed on the right. This is due to the hysteresis of the piezo.

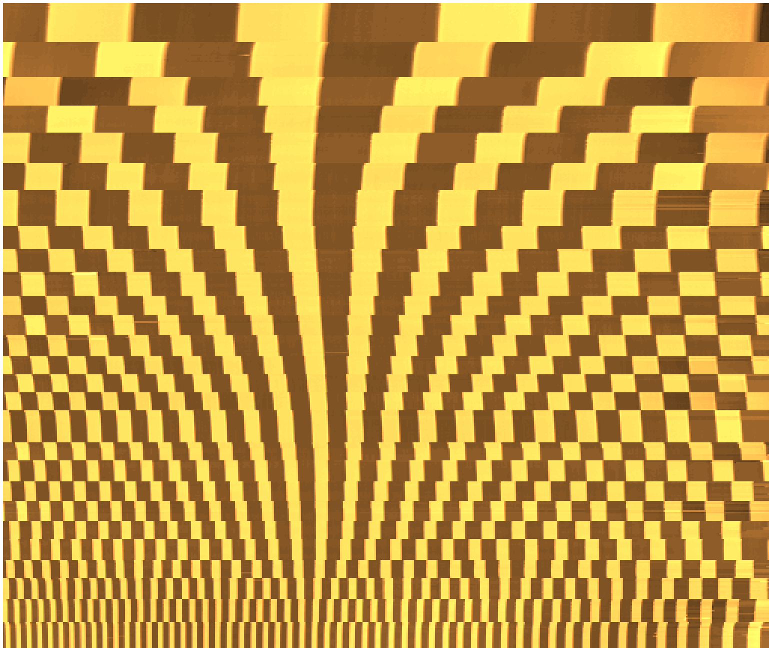

Figure A.2: Long tube scanner, tables 2.1 and 2.2. A sample of lines spaced by 3.0 μm is scanned in retrace direction. The height step between light and dark is 106 nm. The scan size is changed during the scan from top to bottom. The voltage ranges are between 50 V (top) to 440 V (bottom). Note that the patterns are stretched on the left while compressed on the right. This is due to the hysteresis of the piezo.

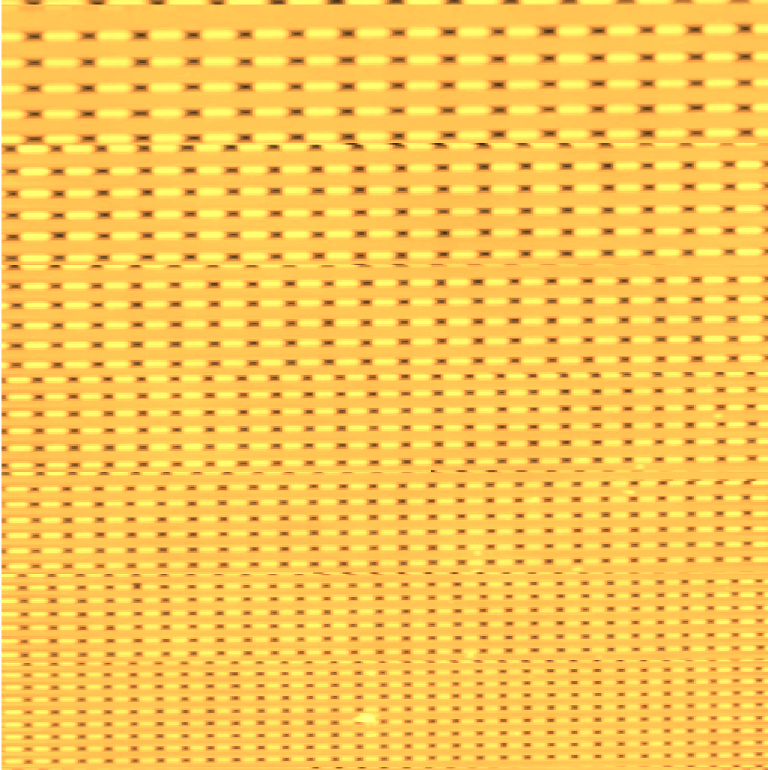

Figure A.3: Long tube scanner, tables 2.1 and 2.2. Trace image of a standard that consists of a 2-dimensional lattice of inverted square pyramids with 200 nm pitch. The height step between light and dark is 70 nm. The scan size is changed during the scan from top to bottom. The scan ranges are between 30 Volt (top) to 15 Volt (bottom).

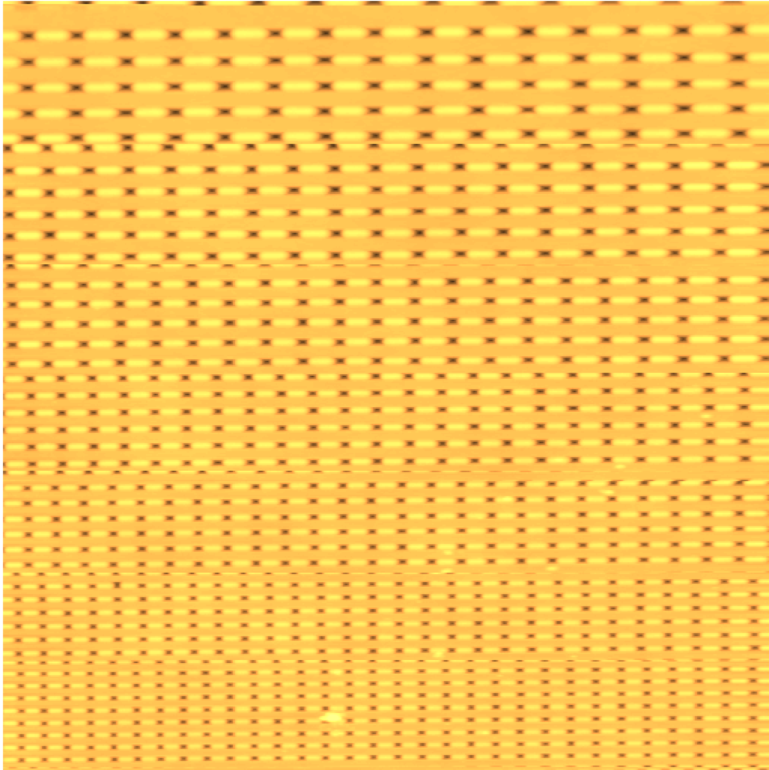

Figure A.4: Long tube scanner, tables 2.1 and 2.2. Retrace image of a standard that consists of a 2-dimensional lattice of inverted square pyramids with 200 nm pitch. The height step between light and dark is 70 nm. The scan size is changed during the scan from top to bottom. The scan ranges are between 30 Volt (top) to 15 Volt (bottom).

Appendix B

Offset analysis

Online corrected experiments have been performed where the scan range, the frequency and the scan offset has been varied. The online errors are plotted versus the scan range and offset for a constant frequency. Here are the figures for the experiments at 0.5 Hz and 2.0 Hz.

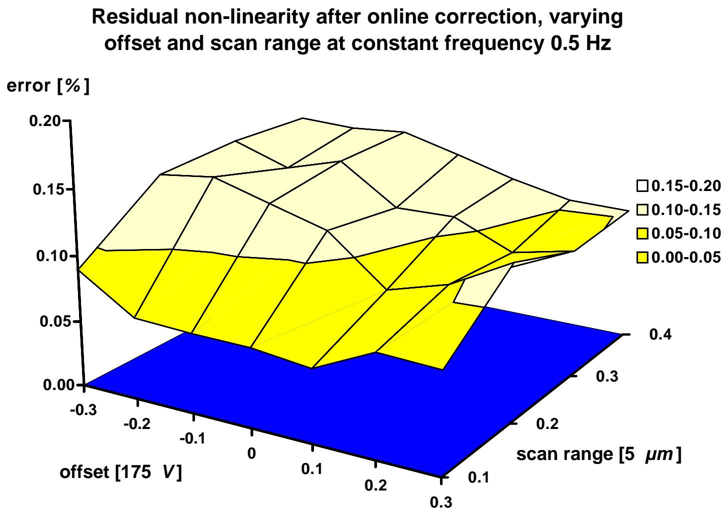

Figure B.1: Short stack scanner, table 4.2. The relative residual errors of non-linearity for different scan offsets and scan ranges at a constant frequency of 0.5 Hz. It is clearly seen that the non-linear error is independent of the offset and well below 0.2 %.

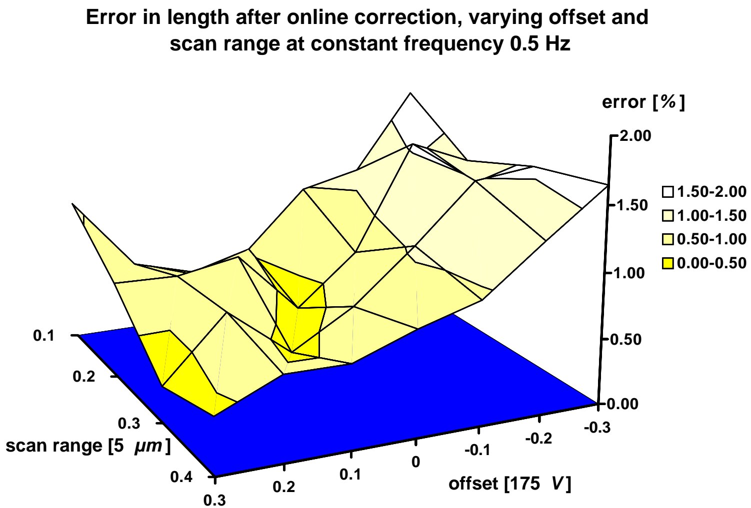

Figure B.2: Short stack scanner, table 4.2. The error in length plotted versus the scan range and offset for a constant frequency of 0.5 Hz. The linear decrease with increasing offset coincides with the growing counterforce applied by the spring. For the scan range of 0.1·5.0 μm, an increase of the error in length is noticable. This can be due to different piezo strains for electric field applied in direction of or opposite to direction of polarization.

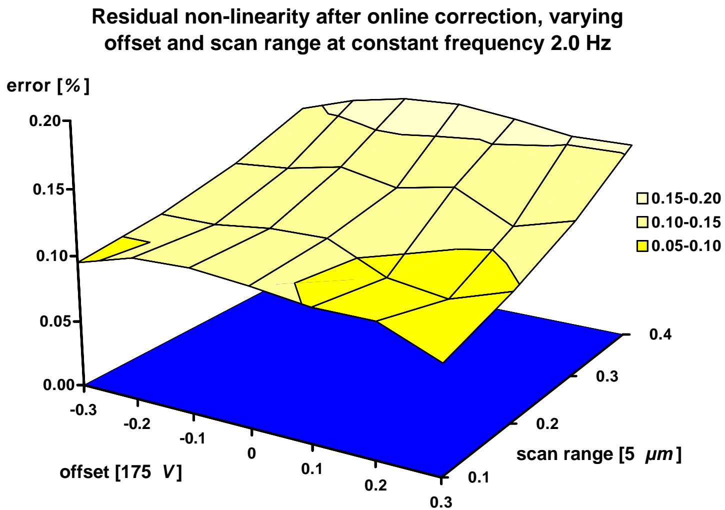

Figure B.3: Short stack scanner, table 4.2. The relative residual errors of non-linearity for different scan offsets and scan ranges at a constant frequency of 2.0 Hz. It is clearly seen that the non-linear error is independent of the offset and well below 0.2 %.

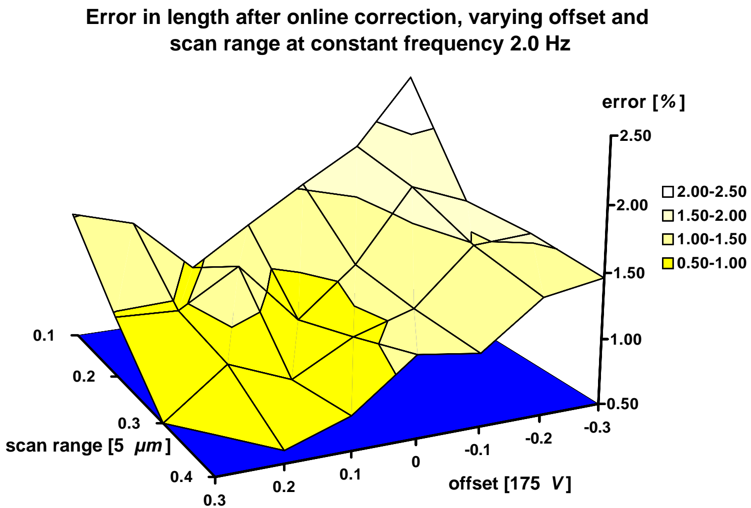

Figure B.4: Short stack scanner, table 4.2. The error in length plotted versus the scan range and offset for a constant frequency of 2.0 Hz. The linear decrease with increasing offset coincides with the growing counterforce applied by the spring. For the scan range of 0.1·5.0 μm, an increase of the error in length is noticable. This can be due to different piezo strains for electric field applied in direction of or opposite to direction of polarization.

Appendix C

Glossary

calibration frame : Set of all of voltage ranges and scan frequencies that have been considered for the calibration procedure.

creep : Time-dependent relaxation phenomenon of a piezo ceramic. A delay of the re-orientation of the Weiss domains that occurs when a ceramic is loaded mechanically or electrically. Overall, the ceramic continues to deform unless countered with an opposite force.

hysteresis : Greek "to arrive late". Closed loop of a rate-independent relaxation phenomenon. When plotting the delayed response versus exciting force, this almond shaped loop is formed.

online / offline : "Online" describes the time during the scan process, "offline" the time after the scanning has been completed.

relaxation : Continuously decaying response to an applied force.

scan offset : The centre point $\frac{V_M+V_m}{2}$ of V_R, typically 0 V for a symmetric scan.

scan range x_R **:** The length on the sample surface as observed in the scanned image from the left-most pixel to the right-most pixel in one line, typically noted in micrometer μm.

sensitivity of a piezo : Linear electro-mechanical coupling factor that determines the amount of extension per applied voltage interval. With the model described in this paper :

$$\hat{b}(\omega, V_M) = b + \frac{b-u}{\alpha V_M}\left(1 - A_1 e^{-\frac{1}{\omega\tau}}\right)\left(A_2 V_M + A_3\right)\left(1 - C_t e^{-\alpha V_M}\right)$$

is the sensitivity of the piezo depending on the scan frequency ω and the upper peak V_M of the oscillating control voltage for a symmetric scan in $[-V_M, V_M]$ around 0.V.

tilt of hysteresis loop : The slope of the line connecting the two turning points $(V_m, x(V_m))$, $(V_M, x(V_M))$ of the hysteresis loop:

$$s\left(V_M; b, u, \alpha\right) = \frac{x_t\left(V_M\right) - x_t\left(V_{-M}\right)}{2V_M} = b - \frac{b-u}{\alpha V_M}\tanh\left(\alpha V_M\right)$$

trace / retrace Commonly used expressions for the scan directions left-to-right "trace" and right-to-left "retrace". Typically "trace" occurs for an increasing flank of control voltage, $\dot{V} > 0$, "retrace" for a decreasing flank, $\dot{V} < 0$, respectively.

voltage range V_R : The peak-to-peak interval $V_R = [V_m, V_M]$ of the oscillating control voltage as sent to the piezo in order to create the scan movement. The maximum of V_R is noted as V_M, the minimum as V_m respectively. Typically a symmetric scan around 0 V is observed, then $V_m = -V_M$.

Weiss domains Clusters of equally oriented dipoles within the piezo ceramic.

Bibliography

[1] B.Ernst, ”The Eye Beguiled - Optical Illusions”, Benedikt Taschen Verlag (1992)

[2] G.Binnig, H.Rohrer,”Scanning tunneling microscopy”, Helvetica Physica Acta (1982) 55. pp. 726-735

[3] J.E.Griffith, D.A. Grigg, ”Dimensional metrology with scanning probe microscopes” J.Appl.Phys. (1993) 74, 9, pp. 83-107

[4] G.Binnig C.F.Quate, C.Gerber,”Atomic Force Microscope”, Physical Review Letters (1986) 56, pp. 930-933

[5] D.Sarid, ”Scanning Force Microscopy”, Oxford Universiy Press, 1994

[6] ”A Practical Guide to Scanning Probe Microscopy”, August 2000, http://www.thermomicro.com/spmguide/contents.htm

[7] L.L.Madsen, ”Scanning Tunneling Microscopy - An Implementation and some Applications”, Ph.D. Thesis June (1990), Danish Institute of Fundamental Metrology and Laboratory of Applied Physics, Technical University of Denmark

[8] DualScope, Danish Micro Engineering DME, Copenhagen, Denmark

[9] Nanoscope III, Digital Instruments Inc., Santa Barbara, CA, USA

[10] A.E.Holman, ”Using capacitive sensors for in situ calibration of displacementts in a piezo-driven stage of an STM”, Sensors and Actuators, A: Physical. (1993), 36 (1) , p. 37-42.

[11] ”Piezo University”, August 2000, http://www.physikinstrumente.com/tutorial/index.html

[12] J. Fu, ”In situ testing and calibration of z-piezo of an atomic force microscope”, Rev. Sci. Instrum. (1995) 66, 7, pp. 3785-3788

[13] J.F.Jørgensen et al., ”Hysteresis correction of scanning tunnelling microscope images”, J.Vac.Sci.Technol. B (1994), 12 (3), pp.1702-1704

[14] D.Croft, S.Devasia, ”Hysteresis and Vibration Compensation for Piezoactuators”, Journal of Guidance, Control and Dynamics (1998)

21, 5, pp. 710-717

[15] R.V.Lapshin, "Analytical model for the approximation of hysteresis loop and its application to the scanning tunneling microscope", Rev.Sci.Instrum. (1995) 66, 9, pp.4718-4730

[16] Dimension 3100 SPM with Metrology AFM Head, Digital Instruments Inc., Santa Barbara, CA, USA

[17] C.V. Newcomb, I. Flinn,"Improving the linearity of piezoelectric ceramic actuators", Electronic Letters (1982) 18, 11, pp. 442-444

[18] M.Goldfarb, N. Celanovic, "Modeling Piezoelectric Stack Actuators for Control of Micromanipulation", IEEE Control Systems Magazine (1997) 17,.3, pp. 69-79 ,ISSN 02721708

[19] K.R.Koops,"Observation of zero creep in piezoelectric actuators", Applied Physics A (1999), A68, 6, pp. 691-697.

[20] B.Jaffe et al., "Piezoelectric Ceramics", Academic Press (1971)

[21] T.Ikeda,"Fundamentals of Piezoelectricicty", Oxford University Press (1990)

[22] C.Z. Rosen et al., "Keypapers in Physics : Piezoelectricity", The American Institute of Physics (1993)

[23] TGZ03 line spacing, 3.0 μm period, NT-MDT, Russia

[24] A. Visintin, "Differential Models of Hysteresis",Springer-Verlag (1991)

[25] M.E. Taylor, "Dynamics of piezoelectric tube scanners for scanning probe microscopy", Rev. Sci. Instrum. 64 (1), January 1993, pp. 154-158

[26] x-y Calibration Standard, 2-dimensional lattice with 200.0 nm pitch, Nanosensors, Germany

[27] J.M.T.A. Adriaens et al.,"Design and Modelling of a Piezo-Actuated Positioning Mechnism", Proceedings of the 36th Conference on Design & Control (1997), pp. 1978-1983

[28] Tzou, H.S., "Piezoelectric Shells, Distributed sensing and control of continua", Kluwer 1993

[29] C.Chen,"Electromechanical deflections of piezoelectric tubes with quartered electrodes", Appl. Phys.Lett. (1992) 60, 1, pp. 132-134

[30] M.Locatelli et.al.,"Easy methods to characterize a piezoelectric ceramic tube as a displacer", Rev.Sci.Instrum. (1988) 59, 4, pp. 661-663

[31] R.G. Carr, "Finite element analysis of PZT tube scanner motion for scanning tunneling microscopy", Journal of Microscopy (1988) 152, 2, pp. 379-385

[32] M.Omura et al., "Simulations of Ferroelectric Characteristics Using a One-Dimensional Lattice Model", Japanese Journal of Applied

Physics, Part1 (1991) 30, 9b, pp. 2384-2387
[33] E. Klotins et al.,"Study and modelling of trapped charge effects in ferroelectrics: application to piezoactuators", Proceedings of the SPIE (1997) 2967, pp. 138-143
[34] B.D.Coleman, M.L.Hodgdon, "A constitutive relation for rate-independent hysteresis in ferromagnetically soft materials", Int. J. Engng. Sci. (1986) 24, 6 ,pp. 897-919
[35] B.D.Coleman, M.L.Hodgdon, "On a class of Constitutive Relations for ferromagnetic hysteresis", Archive for Rational Mechanics and Analysis (1987) 99, 4, pp. 375-396
[36] P.Ge, M. Jouaneh, "Modeling hysteresis in piezoceramic actuators", Precision Engineering (1995) 17, pp. 211-221
[37] Y.K.Wen, "Equivalent linearization for hysteretic systems under random excitation", Transactions of the ASME / Journal of Applied Mechanics (1980) 47, pp. 150-154
[38] M. Jouraneh, H. Tian, "Accuracy enhancement of a piezoelectric actuator with hysteresis", Symposium on Flexible Automation (1992) 1, pp. 631-637
[39] B.M.Chen et al. "An H_∞ almost disturbance decoupling robust controller design for a piezoelectric bimorph actuator with hysteresis", IEEE Transactions on Control Systems Technology (1999) 7, 2, pp.160-174
[40] A.E.Holman et al."Analysis of piezo actuators in translation constructions", Rev.Sci.Instrum. (1995) 66,5, pp. 3208-3215 Tilting, Hyst model
[41] Chen, P.J.; Montgomery, S.T., "A macroscopic theory for the existence of the hysteresis and butterfly loops in ferroelectricity", Ferroelectrics (1980) 23, pp. 199-208
[42] W.H.Press et al.,"Numerical Recipes in C", Cambridge University Press 1992
[43] K.Dirscherl et al."Modeling the hysteresis of a scanning probe microscope", J.Vac.Sci.Technol. B (2000) 18, 2, pp. 621-625
[44] R.W.Basedow, T.D.Cocks,"Piezoelectric ceramic displacment chracteristics at low frequencies and their consequences in Fabry-Perot interferometry", J. Phys. E: Sci. Intrum. (1980) 13, pp. 840-844
[45] R.M.Coreless et al., "On the Lambert W Function", Advances in Computational Mathematics (1996) 5, 4, pp 329-359
[46] K.Briggs, "W-ology or Some exactly solvable growth models", http://epidem13.plantsci.cam.ac.uk/~kbriggs/W-ology.html (August

2000)

[47] C.P.Jensen, "Calibrated Atomic Microscope, Measurements of Vickers Hardness Indentations and Tip Production and Characterisation for Scanning Tunneling Microscope", Ph.D. Thesis (1998), Danish Institute of Fundamental Metrology and Center for Geometrical Metrology, Department of Manufactoring Engineering, Technical University of Denmark

Ph.D. Theses

at the Department of Mathematical Modelling

IMM, DTU

1. **Larsen, Rasmus.** (1994). *Estimation of visual motion in image sequences.* *xiv* + 143 pp.
2. **Rygard, Jens Moberg.** (1994). *Design and optimization of flexible manufacturing systems.* *xiii* + 232 pp.
3. **Lassen, Niels Christian Krieger.** (1994). *Automated determination of crystal orientations from electron backscattering patterns.* *xv* + 136 pp.
4. **Melgaard, Henrik.** (1994). *Identification of physical models.* *xvii* + 246 pp.
5. **Wang, Chunyan.** (1994). *Stochastic differential equations and a biological system.* *xxii* + 153 pp.
6. **Nielsen, Allan Aasbjerg.** (1994). *Analysis of regularly and irregularly sampled spatial, multivariate, and multi-temporal data.* *xxiv* + 213 pp.
7. **Ersbøll, Annette Kjær.** (1994). *On the spatial and temporal correlations in experimentation with agricultural applications.* *xviii* + 345 pp.
8. **Møller, Dorte.** (1994). *Methods for analysis and design of heterogeneous telecommunication networks.* Volume 1-2, *xxxviii* + 282 pp., 283-569 pp.
9. **Jensen, Jens Christian.** (1995). *Teoretiske og eksperimentelle dynamiske undersøgelser af jernbanekøretøjer.* *viii* + 174 pp.
10. **Kuhlmann, Lionel.** (1995). *On automatic visual inspection of reflective surfaces.* Volume 1, *xviii* + 220 pp., (Volume 2, *vi* + 54 pp., fortrolig).
11. **Lazarides, Nikolaos.** (1995). *Nonlinearity in superconductivity and Josephson Junctions.* *iv* + 154 pp.
12. **Rostgaard, Morten.** (1995). *Modelling, estimation and control of fast sampled dynamical systems.* *xiv* + 348 pp.
13. **Schultz, Nette.** (1995). *Segmentation and classification of biological objects.* *xiv* + 194 pp.
14. **Jørgensen, Michael Finn.** (1995). *Nonlinear Hamiltonian systems.* *xiv* + 120 pp.

15. **Balle, Susanne M.** (1995). *Distributed-memory matrix computations.* *iii* + 101 pp.
16. **Kohl, Niklas.** (1995). *Exact methods for time constrained routing and related scheduling problems.* *xviii* + 234 pp.
17. **Rogon, Thomas.** (1995). *Porous media: Analysis, reconstruction and percolation.* *xiv* + 165 pp.
18. **Andersen, Allan Theodor.** (1995). *Modelling of packet traffic with matrix analytic methods.* *xvi* + 242 pp.
19. **Hesthaven, Jan.** (1995). *Numerical studies of unsteady coherent structures and transport in two-dimensional flows.* Risø-R-835(EN) 203 pp.
20. **Slivsgaard, Eva Charlotte.** (l995). *On the interaction between wheels and rails in railway dynamics.* *viii* + 196 pp.
21. **Hartelius, Karsten.** (1996). *Analysis of irregularly distributed points.* *xvi* + 260 pp.
22. **Hansen, Anca Daniela.** (1996). *Predictive control and identification - Applications to steering dynamics.* *xviii* + 307 pp.
23. **Sadegh, Payman.** (1996). *Experiment design and optimization in complex systems.* *xiv* + 162 pp.
24. **Skands, Ulrik.** (1996). *Quantitative methods for the analysis of electron microscope images.* *xvi* + 198 pp.
25. **Bro-Nielsen, Morten.** (1996). *Medical image registration and surgery simulation.* *xxvii* + 274 pp.
26. **Bendtsen, Claus.** (1996). *Parallel numerical algorithms for the solution of systems of ordinary differential equations.* *viii* + 79 pp.
27. **Lauritsen, Morten Bach.** (1997). *Delta-domain predictive control and identification for control.* *xxii* + 292 pp.
28. **Bischoff, Svend.** (1997). *Modelling colliding-pulse mode-locked semiconductor lasers.* *xxii* + 217 pp.
29. **Arnbjerg-Nielsen, Karsten.** (1997). *Statistical analysis of urban hydrology with special emphasis on rainfall modelling.* Institut for Miljøteknik, DTU. *xiv* + 161 pp.
30. **Jacobsen, Judith L.** (1997). *Dynamic modelling of processes in rivers affected by precipitation runoff.* *xix* + 213 pp.
31. **Sommer, Helle Mølgaard.** (1997). *Variability in microbiological degradation experiments - Analysis and case study.* *xiv* + 211 pp.
32. **Ma, Xin.** (1997). *Adaptive extremum control and wind turbine control.* *xix* + 293 pp.

33. **Rasmussen, Kim Ørskov.** (1997). *Nonlinear and stochastic dynamics of coherent structures.* *x* + 215 pp.
34. **Hansen, Lars Henrik.** (1997). *Stochastic modelling of central heating systems.* *xxii* + 301 pp.
35. **Jørgensen, Claus.** (1997). *Driftsoptimering på kraftvarmesystemer.* 290 pp.
36. **Stauning, Ole.** (1997). *Automatic validation of numerical solutions.* *viii* + 116 pp.
37. **Pedersen, Morten With.** (1997). *Optimization of recurrent neural networks for time series modeling.* *x* + 322 pp.
38. **Thorsen, Rune.** (1997). *Restoration of hand function in tetraplegics using myoelectrically controlled functional electrical stimulation of the controlling muscle.* *x* + 154 pp. + Appendix.
39. **Rosholm, Anders.** (1997). *Statistical methods for segmentation and classification of images.* *xvi* + 183 pp.
40. **Petersen, Kim Tilgaard.** (1997). *Estimation of speech quality in telecommunication systems.* *x* + 259 pp.
41. **Jensen, Carsten Nordstrøm.** (1997). *Nonlinear systems with discrete and continuous elements.* 195 pp.
42. **Hansen, Peter S.K.** (1997). *Signal subspace methods for speech enhancement.* *x* + 226 pp.
43. **Nielsen, Ole Møller.** (1998). *Wavelets in scientific computing.* *xiv* + 232 pp.
44. **Kjems, Ulrik.** (1998). *Bayesian signal processing and interpretation of brain scans.* *iv* + 129 pp.
45. **Hansen, Michael Pilegaard.** (1998). *Metaheuristics for multiple objective combinatorial optimization.* *x* + 163 pp.
46. **Riis, Søren Kamaric.** (1998). *Hidden markov models and neural networks for speech recognition.* *x* + 223 pp.
47. **Mørch, Niels Jacob Sand.** (1998). *A multivariate approach to functional neuro modeling.* *xvi* + 147 pp.
48. **Frydendal, Ib.** (1998.) *Quality inspection of sugar beets using vision.* *iv* + 97 pp. + app.
49. **Lundin, Lars Kristian.** (1998). *Parallel computation of rotating flows.* *viii* + 106 pp.
50. **Borges, Pedro.** (1998). *Multicriteria planning and optimization. - Heuristic approaches.* *xiv* + 219 pp.
51. **Nielsen, Jakob Birkedal.** (1998). *New developments in the theory of wheel/rail contact mechanics.* *xviii* + 223 pp.

52. **Fog, Torben.** (1998). *Condition monitoring and fault diagnosis in marine diesel engines. xii* + 178 pp.
53. **Knudsen, Ole.** (1998). *Industrial vision. xii* + 129 pp.
54. **Andersen, Jens Strodl.** (1998). *Statistical analysis of biotests. - Applied to complex polluted samples. xx* + 207 pp.
55. **Philipsen, Peter Alshede.** (1998). *Reconstruction and restoration of PET images. vi* + 132 pp.
56. **Thygesen, Uffe Høgsbro.** (1998). *Robust performance and dissipation of stochastic control systems.* 185 pp.
57. **Hintz-Madsen, Mads.** (1998). *A probabilistic framework for classification of dermatoscopic images. xi* + 153 pp.
58. **Schramm-Nielsen, Karina.** (1998). *Environmental reference materials methods and case studies. xxvi* + 261 pp.
59. **Skyggebjerg, Ole.** (1999). *Acquisition and analysis of complex dynamic intra- and intercellular signaling events.* 83 pp.
60. **Jensen, Kåre Jean.** (1999). *Signal processing for distribution network monitoring. xv* + 199 pp.
61. **Folm-Hansen, Jørgen.** (1999). *On chromatic and geometrical calibration. xiv* + 238 pp.
62. **Larsen, Jesper.** (1999). *Parallelization of the vehicle routing problem with time windows.xx* + 266 pp.
63. **Clausen, Carl Balslev.** (1999). *Spatial solitons in quasi-phase matched struktures. vi* + (flere pag.)
64. **Kvist, Trine.** (1999). *Statistical modelling of fish stocks. xiv* + 173 pp.
65. **Andresen, Per Rønsholt.** (1999). *Surface-bounded growth modeling applied to human mandibles. xxii* + 125 pp.
66. **Sørensen, Per Settergren.** (1999). *Spatial distribution maps for benthic communities.*
67. **Andersen, Helle.** (1999). *Statistical models for standardized toxicity studies. viii* + (flere pag.)
68. **Andersen, Lars Nonboe.** (1999). *Signal processing in the dolphin sonar system. xii* + 214 pp.
69. **Bechmann, Henrik.** (1999). *Modelling of wastewater systems. xviii* + 161 pp.
70. **Nielsen, Henrik Aalborg.** (1999). *Parametric and non-parametric system modelling. xviii* + 209 pp.
71. **Gramkow, Claus.** (1999). *2D and 3D object measurement for control and quality assurance in the industry. xxvi* + 236 pp.

72. **Nielsen, Jan Nygaard.** (1999). *Stochastic modelling of dynamic systems. xvi* + 225 pp.
73. **Larsen, Allan.** (2000). *The dynamic vehicle routing problem. xvi* + 183 pp.
74. **Halkjær, Søren.** (2000). *Elastic wave propagation in anisotropic inhomogeneous materials. xiv* + 133 pp.
75. **Larsen, Theis Leth.** (2000). *Phosphorus diffusion in float zone silicon crystal growth. viii* + 119 pp.
76. **Dirscherl, Kai.** (2000). *Online correction of scanning probe microscopes with pixel accuracy.* 151 pp.